UC Berkeley
UC Berkeley Electronic Theses and Dissertations

Title
Foundations of Strongly Lensed Supernova Cosmology

Permalink
https://escholarship.org/uc/item/0fz318n6

Author
Goldstein, Daniel Abraham

Publication Date
2018

Peer reviewed|Thesis/dissertation

eScholarship.org Powered by the California Digital Library
University of California

Foundations of Strongly Lensed Supernova Cosmology

By

Daniel Goldstein

A dissertation submitted in partial satisfaction of the

requirements for the degree of

Doctor of Philosophy

in

Astrophysics

in the

Graduate Division

of the

University of California, Berkeley

Committee in charge:
Professor Peter Nugent, Co-chair
Professor Daniel Kasen, Co-chair
Professor Joshua Bloom
Professor Saul Perlmutter

Spring 2018

Foundations of Strongly Lensed Supernova Cosmology

Copyright 2018
by
Daniel Goldstein

Abstract

Foundations of Strongly Lensed Supernova Cosmology

by

Daniel Goldstein

Doctor of Philosophy in Astrophysics

University of California, Berkeley

Professor Peter Nugent, Co-chair

Professor Daniel Kasen, Co-chair

This dissertation presents solutions to some problems associated with using strongly gravitationally lensed supernovae (gLSNe) to measure the cosmological parameters. Chief among these are new methods for finding gLSNe and extracting their time delays in the presence of microlensing. The first of these results increased the expected gLSN yields of the Zwicky Transient Facility and the Large Synoptic Survey Telescope, upcoming wide-field optical imaging surveys, by an order of magnitude. The latter of these results involved performing simulations of radiation transport in supernova atmospheres. These simulations provided evidence that some Type Ia supernovae come from sub-Chandrasekhar mass progenitors.

Contents

List of Figures iv

List of Tables vi

Acknowledgments vii

1 Introduction 1
- 1.1 Supernova Cosmology . . . 2
  - 1.1.1 Formalism . . . 2
  - 1.1.2 Supernova Cosmology in Practice . . . 3
- 1.2 Time Delay Cosmology . . . 6
  - 1.2.1 Formalism . . . 6
  - 1.2.2 Time Delay Cosmology in Practice . . . 7
- 1.3 Strongly Lensed Supernova Cosmology . . . 7
- 1.4 Thesis Outline . . . 13

2 A New Method for Automated Transient Identification and Results from its Application to the Dark Energy Survey Supernova Program 14
- 2.1 Introduction . . . 15
- 2.2 The Dark Energy Survey and Transient Detection Pipeline . . . 18
- 2.3 Classifier Development . . . 19
  - 2.3.1 Training Data . . . 19
  - 2.3.2 Features and Processing . . . 23
  - 2.3.3 Classification Algorithm Selection . . . 31
  - 2.3.4 Feature Importances . . . 35
  - 2.3.5 Optimization . . . 35
- 2.4 Performance . . . 36
  - 2.4.1 Performance Metrics . . . 37
  - 2.4.2 Classification Task . . . 37
  - 2.4.3 Results . . . 39
  - 2.4.4 Effect of `autoScan` on Transient Candidate Scanning Load . . . 39
- 2.5 Discussion . . . 42

2.5.1 Automating Artifact Rejection in Future Surveys . . . 42
2.5.2 Eliminating Spurious Candidates . . . 45

3 How to Find Gravitationally Lensed Type Ia Supernovae 47
3.1 Introduction . . . 48
3.2 The Method . . . 49
3.2.1 Sources of Contamination . . . 52
3.3 Yields for Planned Surveys . . . 54
3.3.1 Lens Modeling . . . 54
3.3.2 SN Ia Modeling . . . 55
3.3.3 Monte Carlo Simulation . . . 55
3.4 Discussion . . . 56
3.5 Conclusion . . . 59

4 Precise Time Delays from Strongly Gravitationally Lensed Type Ia Supernovae with Chromatically Microlensed Images 60
4.1 Introduction . . . 61
4.2 Population, Radiation Transport, and Microlensing Simulations . . . 65
4.2.1 The Strongly Lensed Type Ia Supernova Population . . . 65
4.2.2 Microlensing Magnification Patterns . . . 67
4.2.3 Supernova Modeling . . . 68
4.3 Two Phases of Type Ia Supernova Microlensing . . . 70
4.3.1 Physics of Achromatic and Chromatic SN Ia Microlensing . . . 71
4.4 The Effect of Microlensing on LSST Lensed Type Ia Supernova Yields . . . 71
4.4.1 Efficient Identification of Lensed Type Ia Supernovae with Spectral Template Fitting . . . 76
4.4.2 Monte Carlo Simulation . . . 76
4.4.3 Yields . . . 77
4.5 The Effect of Microlensing on Lensed Type Ia Supernova Time Delays . . . 81
4.5.1 Monte Carlo Simulations of Microlensing Time Delay Uncertainty . . . 81
4.5.2 iPTF16geu . . . 85
4.6 Conclusion . . . 85
4.A Radiation Transport Simulation . . . 87
4.B Derivation of Equation 9 . . . 88

5 Evidence for Sub-Chandrasekhar Mass Type Ia Supernovae from an Extensive Survey of Radiative Transfer Models 91
5.1 Introduction . . . 92
5.2 A Simple Model for The Ejecta . . . 93
5.3 Radiation Transport Simulations . . . 94
5.4 Results . . . 96
5.4.1 Light Curves and Empirical Fitting Functions . . . 99

5.5 Discussion 99
5.6 Conclusion 103
5.A Functions Relating Physical Parameters of SNe Ia to Observable Quantities . 104

6 Conclusion **106**

Bibliography **108**

List of Figures

1.1 Maximum-light spectra of different supernova types. . . . 4
1.2 The Phillips relationship. . . . 5
1.3 First-generation Type Ia supernova Hubble Diagram. . . . 8
1.4 Modern Type Ia supernova Hubble diagram. . . . 9
1.5 Tension in the Hubble constant. . . . 10
1.6 *HST* and Keck images of iPTF16geu. . . . 11
1.7 *HST* color-composite image of SN Refsdal. . . . 12

2.1 DES difference image objects classified by `autoScan`. . . . 16
2.2 Schematic of the DES-SN transient detection pipeline. . . . 20
2.3 Difference image cutouts showcasing `r_aper_psf`. . . . 30
2.4 Top three features of `autoScan`. . . . 32
2.5 Classification performance of different machine learning algorithms. . . . 33
2.6 Schematic confusion matrix. . . . 38
2.7 Performance of `autoScan`. . . . 40
2.8 Object-level fake efficiency and false positive rate as a function of S/N. . . . 41
2.9 Limitations of object-level classification for candidates with many detections. . . . 43

3.1 The luminosity function of SNe Ia in elliptical galaxies from SDSS. . . . 50
3.2 Magnification required for our technique to find strongly lensed SNe Ia. . . . 51
3.3 Spec-z v.phot-z for SLACS and BELLS galaxy-galaxy lenses. . . . 53
3.4 Redshift distribution of multiply imaged SNe Ia detectable by our method. . . . 57
3.5 Median time delays and median image separations for the LSST z-band sample. 58

4.1 Source-plane magnification patterns of nine lens galaxy star fields. . . . 62
4.2 Joint distributions of macrolensing and microlensing parameters. . . . 69
4.3 Spectra of a supernova model with and without microlensing. . . . 72
4.4 Difference light curves of model W7. . . . 73
4.5 Rest-frame microlensed color curves of model W7. . . . 74
4.6 Normalized projected specific intensity profiles of model W7. . . . 75
4.7 Detecting a $z_s = 1.91, z_l = 0.96$ LSST glSN Ia with SALT2. . . . 78
4.8 Phases of detected gLSN images when they are discovered. . . . 79
4.9 Source and lens redshift distributions of gLSNe Ia detected by LSST. . . . 80

4.10 Microlensing-induced time delay biased from light curve fitting. 82
4.11 Microlensing time delay error as a function of time delay. 83
4.12 Bias as a function of true time delay for all discovered microlensed image pairs. 84
4.B.1 Integration geometry for Appendix 4.B. 89

5.1 Correlation between M_B and $\Delta M_{15}(B)$ in the models. 97
5.2 Correlation between $M_{\rm Ej}$ and $\Delta M_{15}(B)$ in models. 98
5.3 SEDONA light curves for the models that lie along the WLR (red boxed region in Figure 5.1), color-coded by $M_{^{56}\rm Ni}$. There is a strong correlation between light curve shape and $M_{^{56}\rm Ni}$ in all bands. 100
5.4 Correlation between $M_{^{56}\rm Ni}$ and peak brightness in the models. 101

List of Tables

2.1 DES-SN object and candidate selection requirements. 21
2.2 `autoScan`'s feature library. 26
2.2 `autoScan`'s feature library. 27
2.2 `autoScan`'s feature library. 28
2.2 `autoScan`'s feature library. 29
2.3 Grid search results for `autoScan` hyperparameters. 36
2.4 Effect of `autoScan` on Reprocessed DES Y1 Transient Candidate Scanning Load. 42

4.1 Properties of the magnification patterns in Figure 4.1. 64

5.1 Model Parameters and Assumptions 95

Acknowledgments

Thanks are due to many people for making this thesis not just a reality but an experience that was fun and fulfilling to work on. First among these is my advisor Peter Nugent, who supported me for many years, even when it wasn't clear if there would be any return. Peter was the most important figure in my graduate research experience. He defined my direction, and gave me great ideas and the freedom to pursue them. He taught me how to think big, and how to have the optimism that everything would work out in the end. Peter: thank you.

I was also extremely lucky to benefit over the past 10 years from the advising of Dan Kasen and Masao Sako. Dan gave me a first-rate education in radiation transfer and supernova modeling, and he served as a scientific role model whose creativity, vision, and high standards of quality I aspire to. Masao, my undergraduate advisor, has supported me for almost a decade now, starting before I even arrived to college, and his sage advice and his decision to take me on early in research were essential in getting me where I am today.

In addition to great advising, I was lucky to benefit from exceptional mentorship while writing this thesis. My two most important mentors in graduate school were Eugene Chiang and Rollin Thomas. Eugene helped me figure out what kinds of problems were worth working on, how to find my scientific voice, and how to have fun doing science. By his example, he turned things around for me. From Rollin, I received an unparalleled education in algorithmic thinking, and, for many years, moral support to keep going in graduate school.

I surely would not have made it through graduate school without the support of my friends. First here is Drummond Fielding, who has been like a brother to me. I can't wait to see what life holds for him in New York and beyond, and I am confident he will go on to do great things. I was also lucky to have Alex Kim as a drinking partner, mentor, and collaborator. Alex expanded my palate and showed me the good life, and I will try hard to make it back to the Bay Area often so I don't miss too many of our usual Tuesday meetings.

Eric Linder, Rick Kessler, Josh Bloom, Saul Perlmutter, Phil Marshall, Shri Kulkarni, Mansi Kasliwal, and Greg Aldering all deserve thanks for significant scientific support, collaboration, and feedback. Last but not least, I cannot thank my parents enough for providing unconditional love and support during this journey.

Chapter 1

Introduction

In 1929, Edwin Hubble published observations showing that nearby galaxies are receding at velocities proportional to their distances from us (Hubble 1929). This landmark discovery provided the first evidence that the universe is expanding. Since a static universe was strongly favored at the time, the discovery fundamentally changed our scientific understanding of how the universe works. Precisely characterizing the nature of the expansion has been a flagship goal of astrophysics since.

An important step toward this goal was made more than a decade earlier in 1915, when Albert Einstein published a consolidated, generally covariant theory of relativity (GR), which provided a framework in which the dynamics of an expanding universe could be described mathematically (Einstein 1915). The most general spacetime metric of such a universe is due to Friedmann (1922), and is given by

$$ds^2 = -dt^2 + a^2(t)\left[\frac{dr^2}{1-\kappa r^2} + r^2 d\Omega^2\right], \tag{1.1}$$

where t is a time coordinate, $a(t)$ is a dimensionless scale factor, κ is a curvature parameter with dimensions of $(\text{length})^{-2}$, r is a "comoving" radial coordinate with dimensions of distance, and $d\Omega$ is the standard element of solid angle. Combining this metric with Einstein's field equations yields the famous "Friedmann equation,"

$$H^2 = \frac{8\pi G}{3}\rho - \frac{\kappa}{a^2}, \tag{1.2}$$

where the Hubble parameter $H \equiv \dot{a}/a$ describes the universe's expansion rate and ρ its total energy density.

Simply put, Equation 1.2 says that the "shape" and the density of "stuff" in the universe control how rapidly it expands. By charting the expansion of the universe (left side), we can draw fundamental inferences about its contents and geometry (right side). Two of the principal questions one can ask about the dynamics of an expanding universe are: "how much bigger is the universe today than it was in the past?" and, "how fast is the universe expanding today?" These questions can be posed equivalently as "how does $a(t)$ vary with

cosmic time?" and, "what is the value of the Hubble constant H_0?" where H_0 is defined as the value of H today. Nearly a century after Hubble's discovery, these questions remain open, but many clever techniques have been developed to answer them, and supernovae, the explosive deaths of stars, have played a leading role. In this thesis, I will lay the foundations of a new way to use supernovae to answer these questions.

1.1 Supernova Cosmology

Supernovae have a rich and interesting history of their own, starting with their discovery and observation by ancient civilizations and their subsequent classification by Baade & Zwicky in 1934. Today, we know that supernovae are produced in many different stellar death scenarios. Broadly speaking, all supernovae involve the explosion and disruption of a star. During the explosion, temperatures and densities become high enough for nuclear burning to rapidly fuse material from the star into heavier elements. The explosion ejects this material into the cosmos at a few percent of the speed of light, where it enters free expansion within minutes. Radiation from this ejected material is visible as a luminous transient for weeks to months. The radiation can be powered by any of several mechanisms, with radioactive decay and thermal energy being the most common. Many supernovae can be as bright as hundreds of billions of suns, making them visible across the better part of the observable universe.

1.1.1 Formalism

If the scatter in the peak absolute magnitude M of a class of supernovae is small, the events can be used to precisely constrain some of the parameters on the right-hand side of Equation 1.2, without knowing H_0. To show this, one can integrate Equation 1.2 to obtain the luminosity distance, which in the case of a flat universe dominated by matter and vacuum energy is given by:

$$d_L(z;\Omega_m,\Omega_\Lambda,H_0) = \frac{c(1+z)}{H_0}\int_0^z [(1+z')^2(1+\Omega_m z') - z'(2+z')\Omega_\Lambda]^{-1/2} dz'. \tag{1.3}$$

In Equation 1.3, $z = (a^{-1}-1)$ is the redshift of a photon emitted when the universe had scale factor a, $\rho_c = 3H_0^2/8\pi G$ is the "critical density" required to flatten the universe today (i.e., to set $\kappa = 0$), and the parameters Ω_m and Ω_Λ are defined as the energy density of matter and vacuum energy, respectively, today, divided by the critical density. Following Perlmutter et al. (1997b), from the definition of the distance modulus, we have

$$\begin{aligned} m(z) &= M + 5\log d_L(z;\Omega_m,\Omega_\Lambda,H_0) + 25 \\ &= M + 5\log \mathscr{D}_L(z;\Omega_m,\Omega_\Lambda) - 5\log H_0 + 25, \end{aligned} \tag{1.4}$$

where $m(z)$ is the apparent magnitude of a supernova of absolute magnitude M at redshift z, and $\mathscr{D}_L = H_0 d_L$ is the part of the luminosity distance expression that remains after

multiplying out the dependence on H_0. Using script letters to denote quantities that are independent of H_0, in the low-redshift (nearby) limit, Equation 1.4 reduces to

$$\begin{aligned} m(z) &\simeq M + 5\log cz - 5\log H_0 + 25 \\ &\simeq \mathscr{M} + 5\log cz, \end{aligned} \tag{1.5}$$

where $\mathscr{M} \equiv M - 5\log H_0 + 25$. This quantity can be measured from the apparent magnitudes and redshifts of low-redshift supernovae, without knowing H_0. The dispersions of $\mathscr{M}$ and M are the same, $\sigma_M = \sigma_{\mathscr{M}}$, since $5\log H_0$ is constant. Thus with a set of apparent magnitude and redshift measurements for high-redshift supernovae, and a similar set of low-redshift measurements to determine $\mathscr{M}$, one can find the values of Ω_m and Ω_Λ that best fit the equation

$$m(z) - \mathscr{M} = \mathscr{D}_L(z; \Omega_m, \Omega_\Lambda). \tag{1.6}$$

This analysis constrains the expansion history of the universe (see Equation 1.2), helping to answer the first question posed in this chapter.

1.1.2 Supernova Cosmology in Practice

For decades, it was known that Type Ia supernovae (SNe Ia), a subclass identified spectroscopically by strong Silicon features and a lack of Hydrogen (see Figure 1.1), had a very small dispersion in peak absolute B-band magnitude, $\sigma_{M_B} \approx 0.4$ mag. In 1993, Phillips reduced this dispersion to just 0.2 mag by showing that the B-band decline rate $\Delta M_{15}(B)$, defined as the number of magnitudes an SN Ia declines 15 days after maximum light in the B-band, is strongly correlated with M_B (Figure 1.2). This discovery enabled SNe Ia to be calibrated as precise cosmological distance indicators, capable of placing powerful constraints on Ω_m and Ω_Λ via Equation 1.6. Subsequent efforts, notably those of Tripp (1998) and Guy et al. (2007), have further reduced this dispersion.

Perlmutter et al. (1995, 1997b, 1998) and Garnavich et al. (1998) used samples of low- and high-redshift SNe Ia to carry out this analysis for the first time, laying the foundations for the seminal analyses of Riess et al. (1998) and Perlmutter et al. (1999). The distance-magnitude diagram known as the "Hubble diagram" of Perlmutter et al. (1999) and some of its cosmological implications are reproduced in Figure 1.3. The independent analyses showed that the energy density of the universe today is roughly 30% matter and 70% "dark energy," an unexpected component that was well described by a cosmological constant. In a shocking twist, the two analyses showed that the expansion of the universe was not slowing down due to gravity, but actually accelerating due to some form of dark energy. In the intervening years, this conclusion was confirmed at high levels of precision by more than a dozen independent research groups with successively larger samples of SNe Ia (Figure 1.4) and by other probes such as the cosmic microwave background (CMB; Komatsu et al. 2011; Planck Collaboration et al. 2016a).

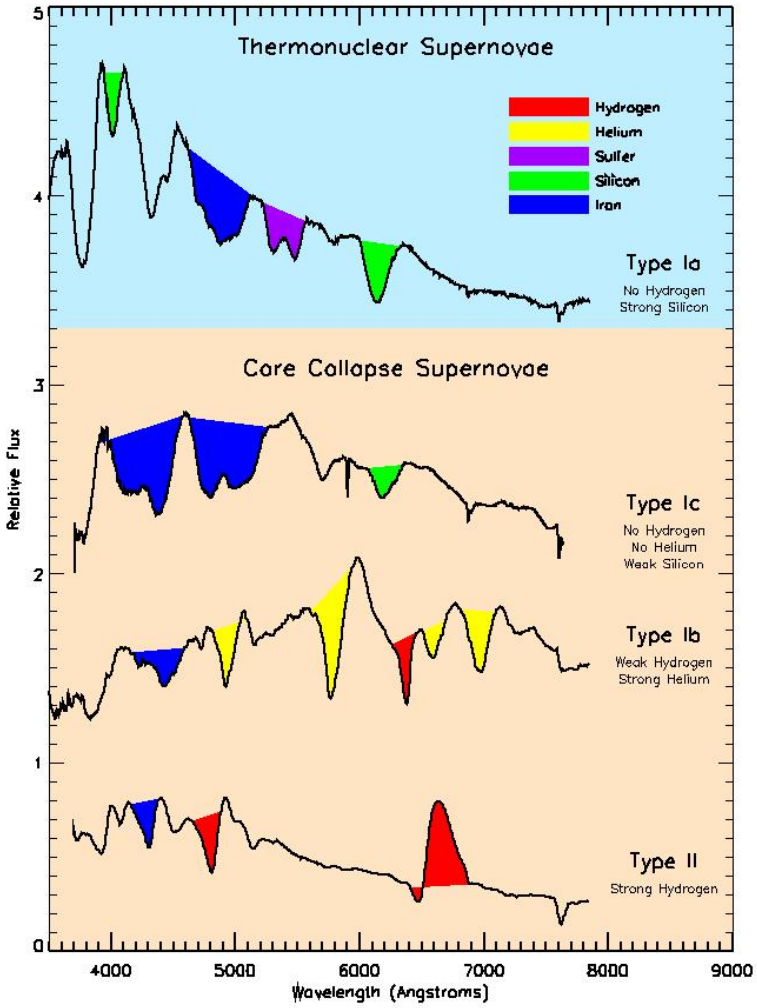

Figure 1.1: Maximum-light spectra of different supernova types (from D. Kasen). Type Ia supernovae are differentiated from other types of supernovae by their strong Silicon features and lack of Hydrogen.

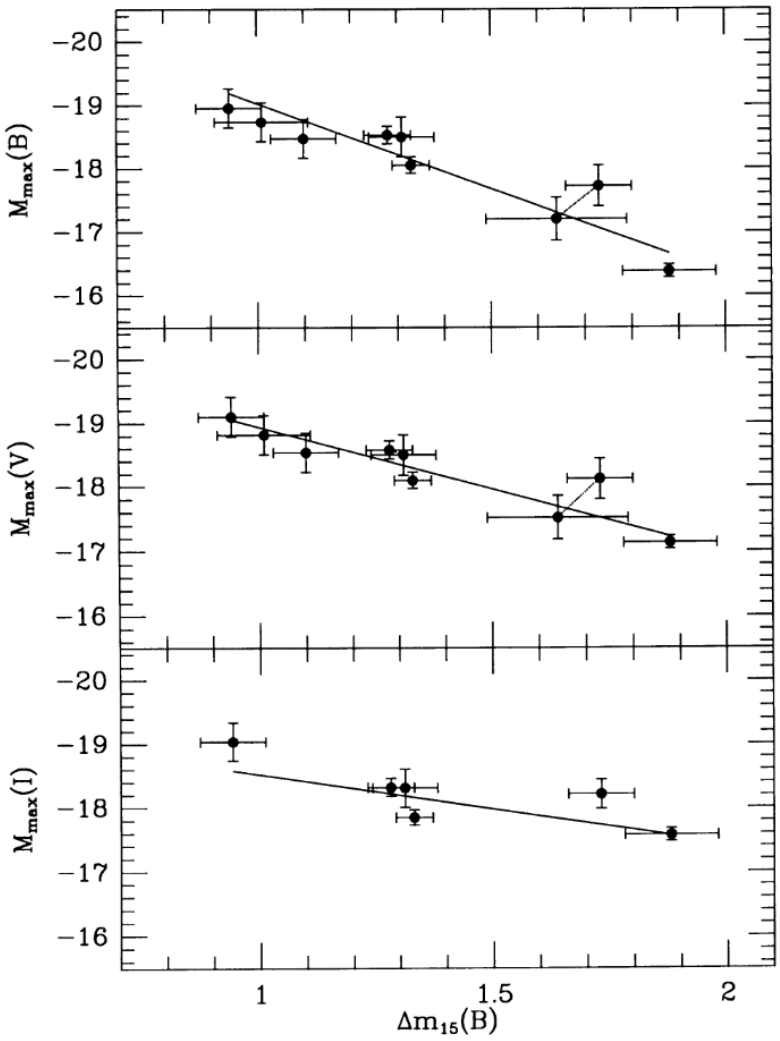

Figure 1.2: Correlation between $\Delta M_{15}(B)$ and M_B in SNe Ia, reproduced from Phillips (1993). This correlation enabled SNe Ia to be calibrated as distance markers for cosmology, and is known as the "Width-luminosity Relationship" or "Phillips relationship" in honor of its discoverer.

1.2 Time Delay Cosmology

Another striking consequence of GR is that light from distant sources is deflected by the gravitational field of massive objects near the line of sight. When the deflection produces multiple images of the same object, the phenomenon is known as "strong gravitational lensing." Multiple images of strongly lensed sources arrive at different times because they travel along different paths and through different gravitational potentials to reach us (Refsdal 1964; Blandford & Narayan 1992). When a strongly lensed source is time-variable, the arrival time delays can be measured and combined with a mass model to yield cosmological constraints. Whereas the supernova cosmology analysis described in Section 1.1 can constrain the time variation of $a(t)$, cosmology from strong lens time delays is most sensitive to H_0.

1.2.1 Formalism

Time delays from strong gravitational lensing are caused by two physical effects: a geometric delay due to the fact that the different images travel different paths to reach us and a gravitational time delay due to the fact that the images traverse different values of the gravitational potential of the lens. Specifically, the time delay of an image at position $\boldsymbol{\theta}$ on the sky relative to an unlensed source at position $\boldsymbol{\beta}$ is

$$\Delta t(\boldsymbol{\theta}, \boldsymbol{\beta}) = \frac{D_l D_s}{D_{ls}}(1 + z_l)\phi(\boldsymbol{\theta}, \boldsymbol{\beta}), \tag{1.7}$$

where D_l is the angular diameter distance to the lens, D_s is the angular diameter distance to the source, and D_{ls} is the angular diameter distance between the lens and the source. Only in flat space is $D_{ls} = D_s - D_l$. ϕ is the Fermat or time delay potential, given by

$$\phi(\boldsymbol{\theta}, \boldsymbol{\beta}) = \frac{(\boldsymbol{\theta} - \boldsymbol{\beta})^2}{2} - \psi(\boldsymbol{\theta}), \tag{1.8}$$

where the first term on the right hand side is the geometric delay and the second term is the lensing potential delay with $\nabla^2\psi = 2\kappa$ for κ the dimensionless lensing projected surface density. Equation 1.7 shows that the time delay Δt is proportional to a triple ratio of angular diameter distances

$$D_{\Delta t} = \frac{D_l D_s}{D_{ls}}, \tag{1.9}$$

known as the "time-delay distance." The time-delay distance contains all of the cosmological information in a strong lensing analysis. Since angular diameter distances are proportional to H_0^{-1}, Equation 1.9 shows that $D_{\Delta t} \propto H_0^{-1}$, making $D_{\Delta t}$ a sensitive probe of H_0.

As Equations 1.7 and 1.8 show, measuring cosmological parameters with strong lens time delays requires three main ingredients (Suyu et al. 2017). First, one must measure the time delays (e.g., Tewes et al. 2013; Bonvin et al. 2017). Second, the lensing potential must be inferred to convert the observed time delays into measurements of the time delay distance (e.g., Wong et al. 2017). This relies on reconstruction of the extended features of the

gravitationally lensed galaxies that host the time delay sources. Finally, the effect of weak lensing by mass close to the lens and along the line of sight must be included (e.g., Suyu et al. 2010; Collett et al. 2013; Rusu et al. 2017; McCully et al. 2017), since lenses are typically found in overdense regions of the universe (Fassnacht et al. 2011).

1.2.2 Time Delay Cosmology in Practice

To date, precision measurements of the cosmological parameters using strong lens time delays have only been obtained using strongly lensed active galactic nuclei (AGNs; e.g., Vuissoz et al. 2008; Suyu et al. 2013; Tewes et al. 2013; Bonvin et al. 2016). Lensed AGNs complicate these ingredients, making percent-level constraints on H_0 difficult. Because the light curves of AGNs are stochastic and heterogeneous, they typically require years of cadenced monitoring to yield precise time delays (Liao et al. 2015). Inferring the lensing potential by reconstructing the lensed host light is challenging since AGNs typically outshine their host galaxies by several magnitudes. Detecting lensed AGNs requires observations of multiple images introducing a selection function for larger Einstein radii and hence an overdense line of sight (Collett & Cunnington 2016), leading to systematic overestimates of H_0.

A time delay measurement of H_0 is needed now more than ever. Since the discovery of cosmic acceleration (Riess et al. 1998; Perlmutter et al. 1999), ΛCDM has become the observationally favored cosmology, implying that the universe is spatially flat, that it contains cold dark matter and baryons, and that its accelerated expansion is driven by a cosmological constant. Recently, a deviation from ΛCDM was reported by Riess et al. (2016), whose measurement of the Hubble constant H_0 using the cosmic distance ladder is in 3.4σ tension with the value inferred from the cosmic microwave background (CMB; Planck Collaboration et al. 2016a), assuming a ΛCDM cosmology and the standard model of particle physics (see Figure 1.5). Independent measurements of H_0 with percent-level accuracy are necessary to determine whether the discrepancy is due to new physics (e.g., a new neutrino species; Riess et al. 2016; Bonvin et al. 2017) or to unmodeled systematics. Time delays can provide these independent measurements.

1.3 Strongly Lensed Supernova Cosmology

In contrast to AGNs, the light curves of Type Ia supernovae (SNe Ia) are remarkably homogeneous, and strongly lensed SN Ia (hereafter, gLSN Ia) light curves evolve over weeks, not years, allowing their time delays to be measured with far less observational overhead than those of AGNs. In addition, gLSNe Ia fade away, allowing a simpler reconstruction of the lensed hosts. gLSNe Ia can be detected even when the separation between the multiple images is less than the seeing (Goobar et al. 2017), simplifying the selection function. Because gLSNe Ia are standardizable candles, they also have the potential to directly determine the lensing magnification factor μ, which can improve constraints on the lens model (Holz 2001; Oguri & Kawano 2003; Foxley-Marrable et al. 2018). The well known spectral energy

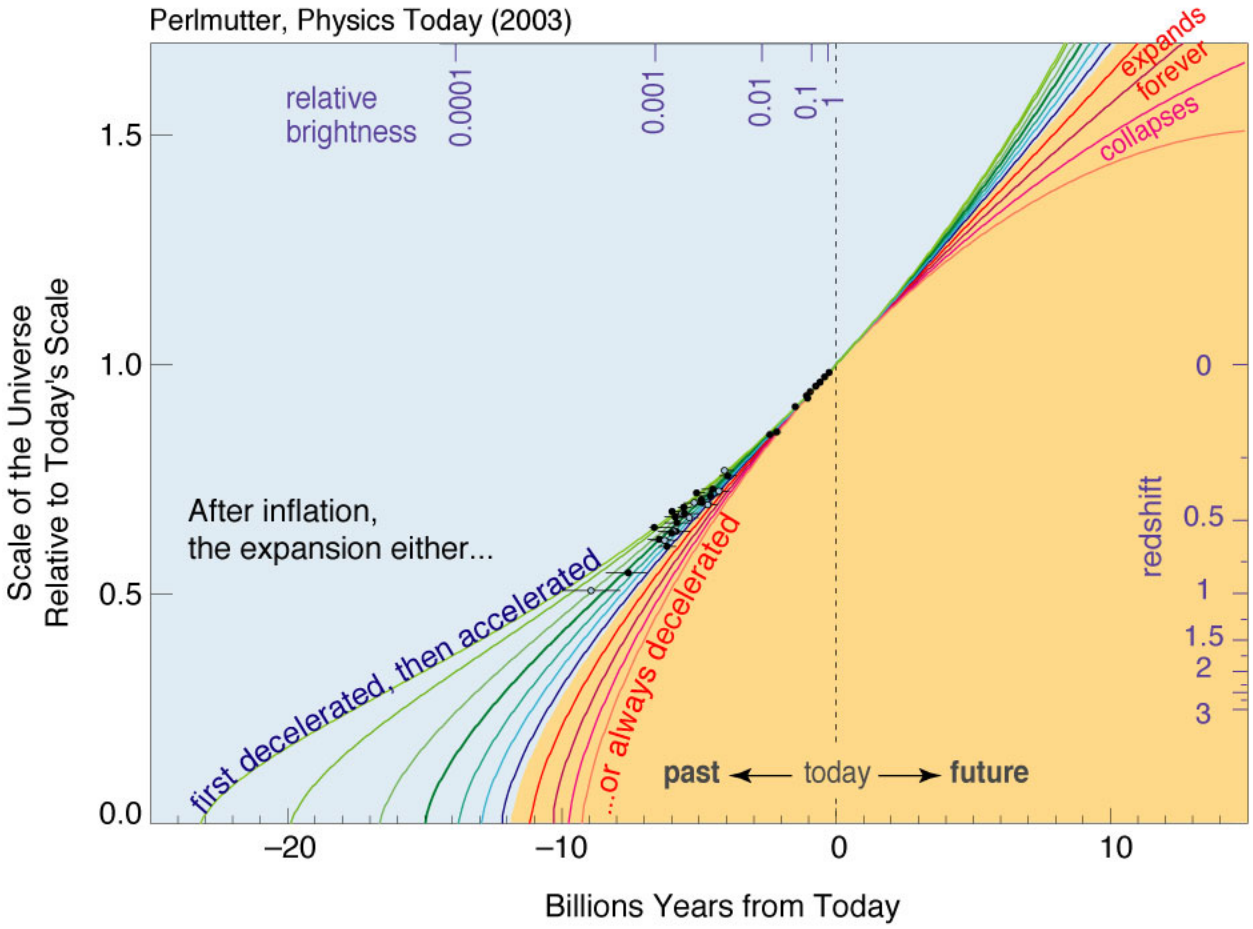

Figure 1.3: A first-generation Type Ia supernova Hubble diagram and some of its cosmological implications. The pioneering work of Riess et al. (1998) and Perlmutter et al. (1999) showed that the universe is currently undergoing a period of accelerated expansion, providing the first evidence for a mysterious property of space called "dark energy," which is now a cornerstone of the cosmological model. The nature of dark energy is one of the greatest open questions in science today.

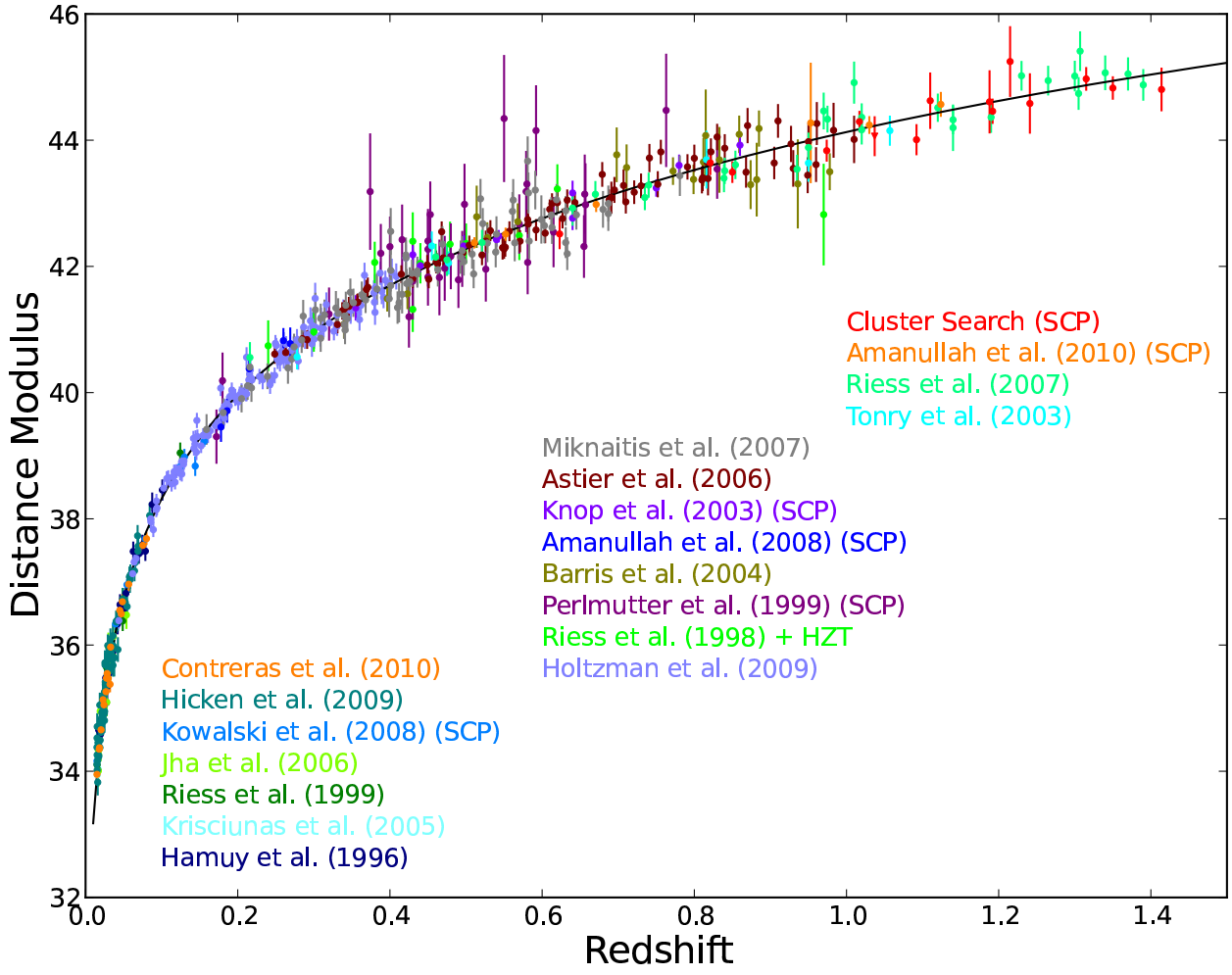

Figure 1.4: A modern Type Ia supernova Hubble diagram, reproduced from Suzuki et al. (2012). Since the late 1990s, dozens of independent research groups have used new samples of Type Ia supernovae to confirm the general findings in Figure 1.3.

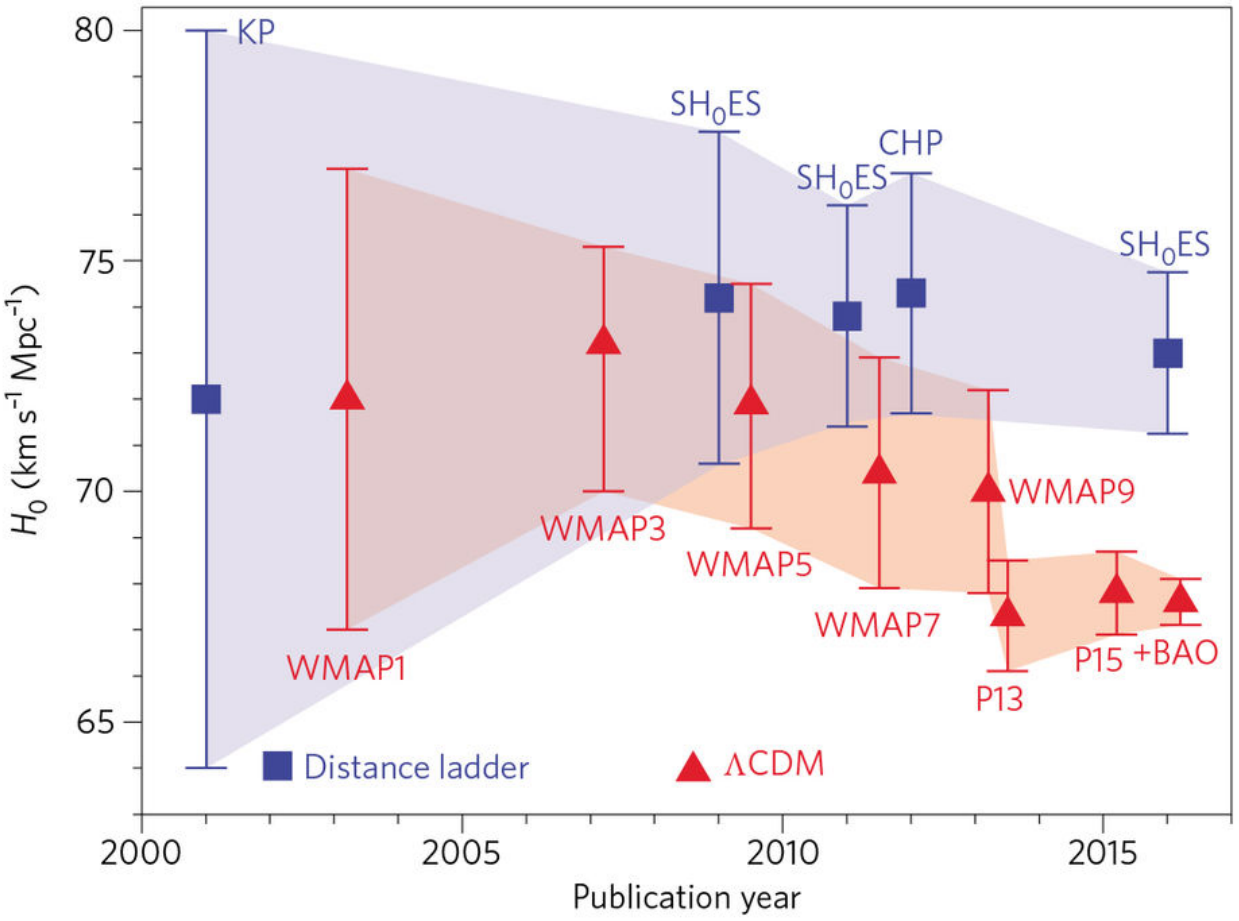

Figure 1.5: Tension in the local (red) and primordial (blue) measurements of the Hubble constant H_0 over time, reproduced from Freedman (2017). H_0 can be inferred to exquisite precision with measurements of the *nearby* universe using the distance ladder (Riess et al. 2016, $H_0 = 73.24 \pm 1.74\,\mathrm{km/s/Mpc}$). It can also be inferred with measurements of the *primordial* universe using the cosmic microwave background (CMB), assuming a ΛCDM cosmology (Planck Collaboration et al. 2016b, $H_0 = 66.93 \pm 0.62\,\mathrm{km/s/Mpc}$). The tension between these local and distant measurements is palpable: they currently disagree by 3.4σ (99.9% significance). Currently, this is the largest tension in cosmology. It is potentially a sign of new fundamental physics, such as sterile neutrinos or "phantom" dark energy (e.g., Di Valentino et al. 2016; Freedman 2017; Zhao et al. 2017). But it may also be a sign of something more mundane, such as systematics in the measurements (e.g., Efstathiou 2014; Bernal et al. 2016; Rigault et al. 2015).

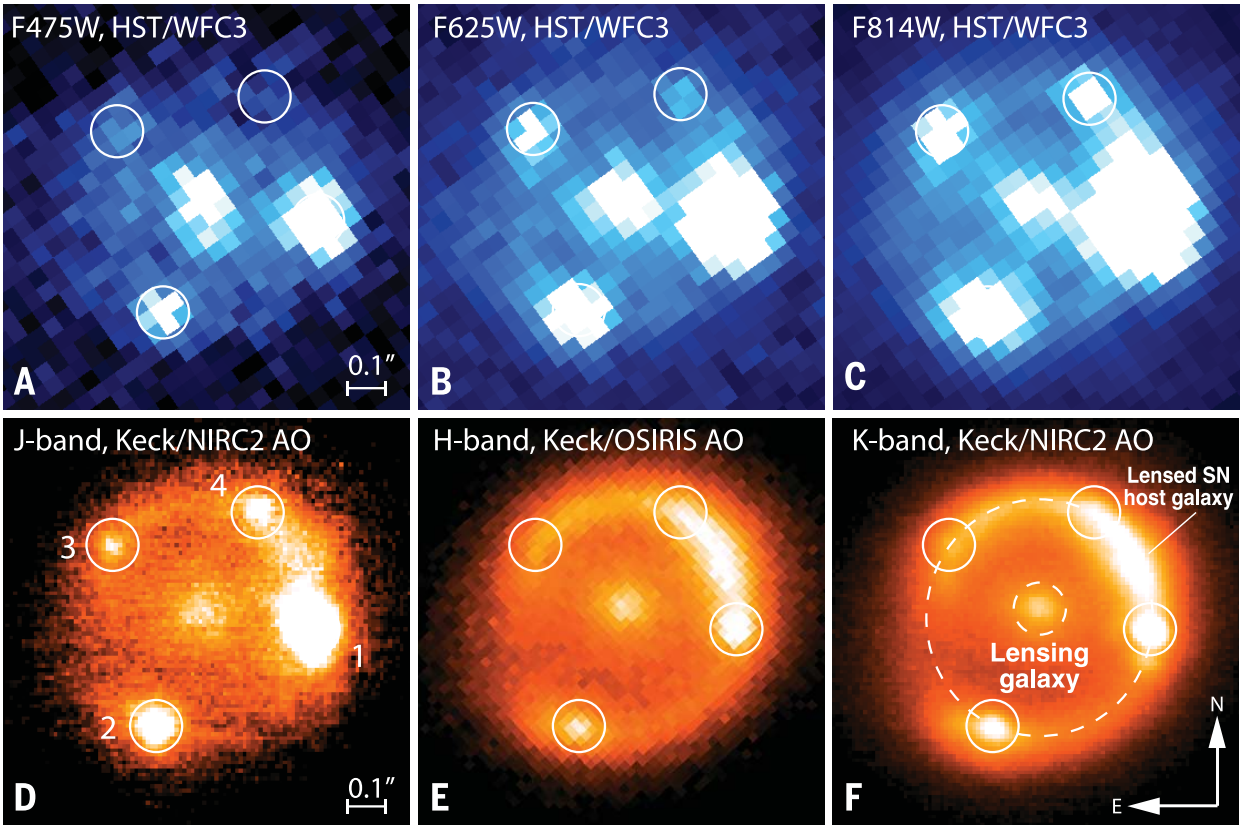

Figure 1.6: iPTF16geu, a Type Ia supernova at $z = 0.4$ strongly lensed by an elliptical galaxy at $z = 0.2$ (data from *HST* and Keck). This transient—the only known gLSN Ia—was discovered by the Zwicky Transient Facility's predecessor, iPTF. The multiple images of the supernova are indicated with circles. Figure reproduced from Goobar et al. (2017).

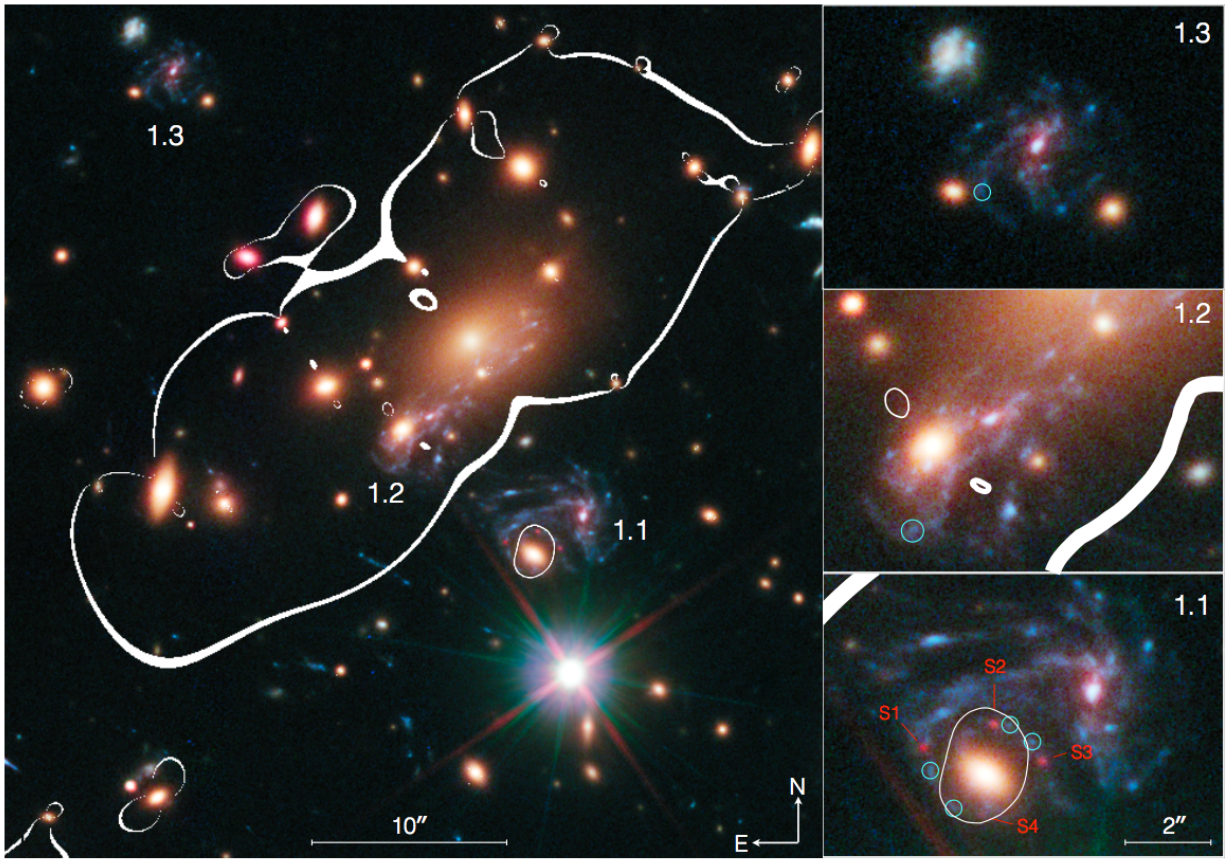

Figure 1.7: SN Refsdal (Kelly et al. 2015a), the first gLSN discovered with resolved multiple images. The supernova and its host galaxy were lensed by the galaxy cluster MACS J1149+2223. Due to the complicated mass distribution of the cluster six lensed images of the transient were produced. The locations of four of these images are designated with red labels.

distributions (SEDs) of SNe Ia also allow one to correct for extinction along the paths of each SN Ia image—another major advantage over AGNs.

Despite these advantages, several challenges face SNe Ia as tools for time delay measurements. First, multiply imaged SNe Ia are rarer than multiply imaged quasars and AGNs. Whereas the number of robust time delays from quasars is now in the double digits, only one multiply imaged SN Ia—iPTF16geu (Goobar et al. 2017, Figure 1.6)—has ever been found. Before this serendipitous event, only a multiply imaged core-collapse SN (Kelly et al. 2015a,b, Figure 1.7) and a few lensed, but not multiply imaged, SNe Ia had been discovered (Amanullah et al. 2011; Nordin et al. 2014; Patel et al. 2014; Rodney et al. 2015; Petrushevska et al. 2016). Another challenge is that most SNe Ia are visible for only ∼100 days after they explode, whereas AGNs and quasars can be monitored for variability over much longer time scales. Because high-resolution imaging or spectroscopy while an SN Ia is still active is necessary to measure a time delay, this creates pressure to identify strongly lensed SNe Ia as soon after explosion as possible. Quimby et al. (2014) classified an event as a lensed SN Ia that was previously thought to be a new type of superluminous supernova (Chornock et al. 2013). However, the classification was performed well after the event had faded and thus neither the properties of the lens system nor H_0 could be constrained. Finally, most strong gravitational lenses produce images that are separated by less than the resolution of ground-based optical surveys (Oguri 2006). Images of iPTF16geu were detected just $0.3''$ away from the center of a $z = 0.21$ quiescent galaxy, yet the initial discovery was performed on a telescope with typical seeing of $2.5''$.

1.4 Thesis Outline

In this thesis, I present solutions to some problems associated with using strongly gravitationally lensed supernovae (gLSNe) to measure the cosmological parameters. Chief among these are new methods for finding gLSNe and extracting their time delays in the presence of microlensing. The latter of these results involved performing simulations of radiation transport in supernova atmospheres. These simulations provided evidence that some Type Ia supernovae come from sub-Chandrasekhar mass progenitors.

In Chapter 2, I introduce a machine-learning based algorithm for identifying astrophysical sources of variability on difference images from large-scale supernova searches. This algorithm reduces the contamination by artifacts of processing and instrumentation in searches for gLSNe. In Chapter 3, I introduce a new technique for identifying gLSNe Ia in wide-area surveys in which they cannot be resolved. This technique improves the expected gLSN Ia yields of upcoming surveys like the Zwicky Transient Facility and the Large Synoptic Survey Telsecope by an order of magnitude. In Chapter 4, I present a new technique to accurately and precisely measure gLSN Ia time delays in microlensed images, retiring a major systematic facing the cosmology analysis. In Chapter 5, I use simulations similar to those in Chapter 4 along with the Phillips relationship to show that some SNe Ia must have sub-Chandrasekhar mass progenitors. I conclude in Chapter 6.

Chapter 2

A New Method for Automated Transient Identification and Results from its Application to the Dark Energy Survey Supernova Program

An earlier version of this article was previously published as Goldstein, D. A., D'Andrea, C. B., Fischer, J. A., et al. 2015, AJ, 150, 82.

Abstract

We describe an algorithm for identifying point-source transients and moving objects on reference-subtracted optical images containing artifacts of processing and instrumentation. The algorithm makes use of the supervised machine learning technique known as Random Forest. We present results from its use in the Dark Energy Survey Supernova program (DES-SN), where it was trained using a sample of 898,963 signal and background events generated by the transient detection pipeline. After reprocessing the data collected during the first DES-SN observing season (Sep. 2013 through Feb. 2014) using the algorithm, the number of transient candidates eligible for human scanning decreased by a factor of 13.4, while only 1.0 percent of the artificial Type Ia supernovae (SNe) injected into search images to monitor survey efficiency were lost, most of which were very faint events. Here we characterize the algorithm's performance in detail, and we discuss how it can inform pipeline design decisions for future time-domain imaging surveys, such as the Large Synoptic Survey Telescope and the Zwicky Transient Facility. An implementation of the algorithm and the training data used in this paper are available at http://portal.nersc.gov/project/dessn/autoscan.

2.1 Introduction

To identify scientifically valuable transients or moving objects on the sky, imaging surveys have historically adopted a manual approach, employing humans to visually inspect images for signatures of the events (e.g., Zwicky 1964; Hamuy et al. 1993; Perlmutter et al. 1997a; Schmidt et al. 1998; Filippenko et al. 2001; Strolger et al. 2004; Blanc et al. 2004; Astier et al. 2006; Sako et al. 2008; Mainzer et al. 2011; Waszczak et al. 2013; Rest et al. 2014). But recent advances in the capabilities of telescopes, detectors, and supercomputers have fueled a dramatic rise in the data production rates of such surveys, straining the ability of their teams to quickly and comprehensively look at images to perform discovery.

For surveys that search for objects on difference images—CCD images that reveal changes in the appearance of a region of the sky between two points in time—this problem of data volume is compounded by the problem of data purity. Difference images are produced by subtracting reference images from single-epoch images in a process that involves point-spread function (PSF) matching and image distortion (see, e.g., Alard & Lupton 1998). In addition to legitimate detections of astrophysical variability, they can contain artifacts of the differencing process, such as poorly subtracted galaxies, and artifacts of the single-epoch images, such as cosmic rays, optical ghosts, star halos, defective pixels, near-field objects, and CCD edge effects. Some examples are presented in Figure 2.1. These artifacts can vastly outnumber the signatures of scientifically valuable sources on the images, forcing object detection thresholds to be considerably higher than what is to be expected from Gaussian fluctuations.

For time-domain imaging surveys with a spectroscopic follow-up program, these issues of data volume and purity are compounded by time-pressure to produce lists of the most promising targets for follow-up observations before they become too faint to observe or fall outside a window of scientific utility. Ongoing searches for Type Ia supernovae (SNe Ia) out to $z \sim 1$, such as the Panoramic Survey Telescope and Rapid Response System Medium Deep Survey's (Rest et al. 2014) and the Dark Energy Survey's (DES; Flaugher 2005), face all three of these challenges. The DES supernova program (DES-SN; Bernstein et al. 2012), for example, produces up to 170 gigabytes of raw imaging data on a nightly basis. Visual examination of sources extracted from the resulting difference images using `SExtractor` (Bertin & Arnouts 1996) revealed that ~ 93 percent are artifacts, even after selection cuts (Kessler et al. 2015, in preparation). Additionally, the survey has a science-critical spectroscopic follow-up program for which it must routinely select the ~ 10 most promising transient candidates from hundreds of possibilities, most of which are artifacts. This program is crucial to survey science as it allows DES to confirm transient candidates as SNe, train and optimize its photometric SN typing algorithms (e.g., `PSNID`; Sako et al. 2011, `NNN`; Karpenka et al. 2013), and investigate interesting non-SN transients. To prepare a list of objects eligible for consideration for spectroscopic follow-up observations, members of DES-SN scanned nearly 1 million objects extracted from difference images during the survey's first observing season, the numerical equivalent of nearly a week of uninterrupted scanning time, assuming scanning one object takes half a second.

For DES to meet its discovery goals, more efficient techniques for artifact rejection

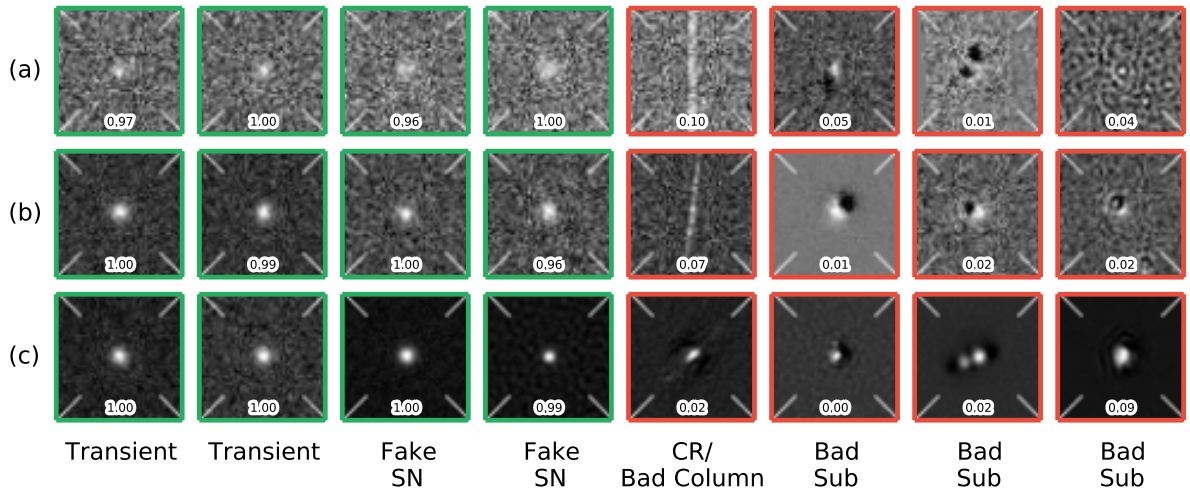

Figure 2.1: Cutouts of DES difference images, roughly 14 arcsec on a side, centered on legitimate (green boxes; left four columns of figure) and spurious (red boxes; right four columns of figure) objects, at a variety of signal-to-noise ratios: (a) S/N $\leq$ 10, (b) 10 $<$ S/N $\leq$ 30, (c) 30 $<$ S/N $\leq$ 100. The cutouts are subclassed to illustrate both the visual diversity of spurious objects and the homogeneity of authentic ones. Objects in the "Transient" columns are real astrophysical transients that subtracted cleanly. Objects in the "Fake SN" columns are fake SNe Ia injected into transient search images to monitor survey efficiency. The column labeled "CR/Bad Column" shows detections of cosmic rays (rows b and c) and a bad column on the CCD detector (row a). The columns labeled "Bad Sub" show non-varying astrophysical sources that did not subtract cleanly; this can result from poor astrometric solutions, shallow templates, or bad observing conditions. The numbers at the bottom of each cutout indicate the score that each detection received from the machine learning algorithm introduced in §2.3; a score of 1.0 indicates the algorithm is perfectly confident that the detection is not an artifact, while a score of 0.0 indicates the opposite.

on difference images are needed. Efforts to "crowd-source" similar large-scale classification problems have been successful at scaling with growing data rates; websites such as Zooniverse.org have accumulated over one million users to tackle a variety of astrophysical classification problems, including the classification of transient candidates from the Palomar Transient Factory (PTF; Smith et al. 2011). However, for DES to optimize classification accuracy and generate reproducible classification decisions, automated techniques are required.

To reduce the number of spurious candidates considered for spectroscopic follow-up, many surveys impose selection requirements on quantities that can be directly and automatically computed from the raw imaging data. Making hard selection cuts of this kind has been shown to be a suboptimal technique for artifact rejection in difference imaging. Although such cuts are automatic and easy to interpret, they do not naturally handle correlations between features, and they are an inefficient way to select a subset of the high-dimensional feature space as the number of dimensions grows large (Bailey et al. 2007).

In contrast to selection cuts, machine learning (ML) classification techniques provide a flexible solution to the problem of artifact rejection in difference imaging. In general, these techniques attempt to infer a precise mapping between numeric features that describe characteristics of observed data, and the classes or labels assigned to those data, using a training set of feature-class pairs. ML classification algorithms that generate decision rules using labeled data—data whose class membership has already been definitively established—are called "supervised" algorithms. After generating a decision rule, supervised ML classifiers can be used to predict the classes of unlabeled data instances. For a review of supervised ML classification in astronomy, see, e.g., Bloom & Richards (2012) or Ivezić et al. (2014). For an introduction to the statistical underpinnings of supervised ML classification techniques, see Willsky et al. (1995).

Such classifiers address many of the shortcomings of scanning and selection cuts. ML algorithms' decisions are automatic, reproducible, and fast enough to process streaming data in real-time. Their biases can be systematically and quantitatively studied, and, most importantly, given adequate computing resources, they remain fast and consistent in the face of increasing data production rates. As more data are collected, ML methods can continue to refine their knowledge about a data set (see §2.5.1), thereby improving their predictive performance on future data. Supervised ML classification techniques are currently used in a variety of astronomical contexts, including time-series analysis, such as the classification of variable stars (Richards et al. 2011) and SNe (Karpenka et al. 2013) from light curves, and image analysis, such as the typing of galaxies (Banerji et al. 2010), and discovery of trans-Neptunian objects (Gerdes et al. 2015, in preparation) on images. Although their input data types differ, light curve shape and image-based ML classification frameworks are quite similar: both operate on tabular numeric classification features computed from raw input data (see §2.3.2).

The use of supervised machine learning classification techniques for artifact rejection in difference imaging was pioneered by Bailey et al. (2007) for the Nearby Supernova Factory

(Aldering et al. 2002) using imaging data from the Near-Earth Asteroid Tracking program[1] and the Palomar-QUEST Consortium, using the 112-CCD QUEST-II camera (Baltay et al. 2007). They compared the performance of three supervised classification techniques—a Support Vector Machine, a Random Forest, and an ensemble of boosted decision trees—in separating a combination of real and fake detections of SNe from background events. They found that boosted decision trees constructed from a library of astrophysical domain features (magnitude, FWHM, distance to the nearest object in the reference co-add, measures of roundness, etc.) provided the best overall performance.

Bloom et al. (2012) built on the methodology of Bailey et al. (2007) by developing a highly accurate Random Forest framework for classifying detections of variability extracted from PTF difference images. Brink et al. (2013) made improvements to the classifier of Bloom et al. (2012), setting an unbroken benchmark for best overall performance on the PTF data set, using the technique of recursive feature elimination to optimize their classifier. Recently, du Buisson et al. (2015) published a systematic comparison of several classification algorithms using features based on Principal Component Analysis (PCA) extracted from Sloan Digital Sky Survey-II SN survey difference images. Finally, Wright et al. (2015) used a pixel-based approach to engineer a Random Forest classifier for the Pan-STARRS Medium Deep Survey.

In this article, we describe `autoScan`, a computer program developed for this purpose in DES-SN. Our main objective is to report the methodology that DES-SN adopted to construct an effective supervised classifier, with an eye toward informing the design of similar frameworks for future time domain surveys such as the Large Synoptic Survey Telescope (LSST; LSST Science Collaboration et al. 2009) and the Zwicky Transient Facility (ZTF; Smith et al. 2014). We extend the work of previous authors to a newer, larger data set, showing how greater selection efficiency can be achieved by increasing training set size, using generative models for training data, and implementing new classification features.

The structure of the paper is as follows. In §2.2, we provide an overview of DES and the DES-SN transient detection pipeline. In §2.3, we describe the development of `autoScan`. In §2.4, we present metrics for evaluating the code's performance and review its performance on a realistic classification task. In §2.5, we discuss lessons learned and areas of future development that can inform the design of similar frameworks for future surveys.

2.2 The Dark Energy Survey and Transient Detection Pipeline

In this section, we introduce DES and the DES-SN transient detection pipeline ("`DiffImg`"; Kessler et al. 2015, in preparation), which produced the data used to train and validate `autoScan`. DES is a Stage III ground-based dark energy experiment designed to provide the tightest constraints to date on the dark energy equation of state parameter using observations of the four most powerful probes of dark energy suggested by the Dark Energy Task Force

[1] `http://neat.jpl.nasa.gov`.

(DETF; Albrecht et al. 2006): SNe Ia, galaxy clusters, baryon acoustic oscillations, and weak gravitational lensing. DES consists of two interleaved imaging surveys: a wide-area survey that covers 5,000 deg^2 of the south Galactic cap in 5 filters ($grizY$), and DES-SN, a time-domain transient survey that covers 10 (8 "shallow" and 2 "deep") 3 deg^2 fields in the XMM-LSS, ELAIS-S, CDFS, and Stripe-82 regions of the sky, in four filters ($griz$). The survey's main instrument, the Dark Energy Camera (DECam; Diehl 2012; Flaugher et al. 2012; Flaugher et al. 2015, submitted), is a 570-megapixel 3 deg^2 imager with 62 fully depleted, red-sensitive CCDs. It is mounted at the prime focus of the Victor M. Blanco 4m telescope at the Cerro Tololo Inter-American Observatory (CTIO). DES conducted "science verification" (SV) commissioning observations from November 2012 until February 2013, and it began science operations in August 2013 that will continue until at least 2018 (Diehl et al. 2014). The data used in this article are from the first season of DES science operations ("Y1"; Aug. 2013—Feb. 2014).

A schematic of the pipeline that DES-SN employs to discover transients is presented in Figure 2.2. Transient survey "science images" are single-epoch CCD images from the DES-SN fields. After the image subtraction step, sources are extracted using `SExtractor`. Sources that pass the cuts described in the Object section of Table 2.1 are referred to as "detections." A "raw candidate" is defined when two or more detections match to within 1". A raw candidate is promoted to a "science candidate" when it passes the `NUMEPOCHS` requirement in Table 2.1. This selection requirement was imposed to reject Solar System objects, such as main belt asteroids and Kuiper belt objects, which move substantially on images from night to night. Science candidates are eligible for visual examination and spectroscopic follow-up observations. During the observing season, science candidates are routinely photometered, fit with multi-band SN light curve models, visually inspected, and slated for spectroscopic follow-up.

2.3 Classifier Development

In this section, we describe the development of `autoScan`. We present the classifier's training data set (§2.3.1), its classification feature set (§2.3.2), and the selection (§2.3.3), properties (§2.3.4), and optimization (§2.3.5) of its core classification algorithm.

2.3.1 Training Data

To make probabilistic statements about the class membership of new data, supervised ML classifiers must be trained or fit to existing data whose true class labels are already known. Each data instance is described by numeric classification "features" (see §2.3.2); an effective training data set must approximate the joint feature distributions of all classes considered. Objects extracted from difference images can belong to one of two classes: "Artifacts," or "Non-Artifacts." Examples of each class must be present in the training set. Failing to include data from certain regions of feature space can corrode the predictive performance of the

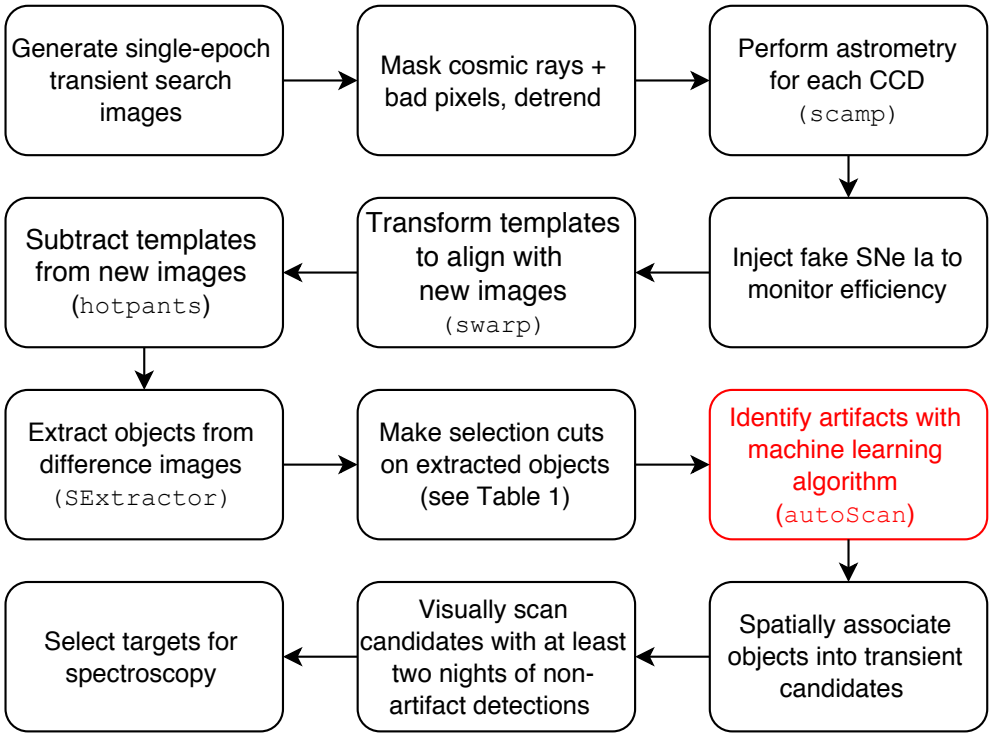

Figure 2.2: Schematic of the DES-SN transient detection pipeline. The magnitudes of fake SNe Ia used to monitor survey efficiency are calibrated using the zero point of the images into which they are injected and generated according to the procedure described in §2.3.1. The `autoScan` step (red box) occurs after selection cuts are applied to objects extracted from difference images and before objects are spatially associated into raw transient candidates. Codes used at specific steps are indicated in parenthesis.

Table 2.1: DES-SN object and candidate selection requirements.

Set	Feature	Lower Limit	Upper Limit	Description
Object	MAG	···	30.0	Magnitude from SExtractor.
	A_IMAGE	···	1.5 pix.	Length of semi-major axis from SExtractor.
	SPREAD_MODEL	···	$3\sigma_S + 1.0$	Star-galaxy separation output parameter from SExtractor. σ_S is the estimated SPREAD_MODEL uncertainty.
	CHISQ	···	10^4	χ^2 from PSF-fit to 35×35 pixel cutout around object in difference image.
	SNR	3.5	···	Flux from a PSF-model fit to a 35×35 pixel cutout around the object divided by the uncertainty from the fit.
	VETOMAG[a]	21.0	···	Magnitude from SExtractor for use in veto catalog check.
	VETOTOL[a]	Magnitude-dependent	···	Separation from nearest object in veto catalog of bright stars.
	DIPOLE6	···	2	N_{pix} in 35×35 pixel object-centered cutout at least 6σ below 0.
	DIPOLE4	···	20	N_{pix} in 35×35 pixel object-centered cutout at least 4σ below 0.
	DIPOLE2	···	200	N_{pix} in 35×35 pixel object-centered cutout at least 2σ below 0.
Candidate	NUMEPOCHS	2	···	Number of distinct nights that the candidate is detected.

[a]The difference imaging pipeline is expected to produce false positives near bright or variable stars, thus all difference image objects are checked against a "veto" catalog of known bright and variable stars and are rejected if they are brighter than 21st magnitude and within a magnitude-dependent radius of a veto catalog source. Thus only one of VETOMAG and VETOTOL must be satisfied for an object to be selected.

classifier in those regions, introducing bias into the search that can systematically degrade survey efficiency (Richards et al. 2012). Because the training set compilation described here took place during the beginning of Y1, it was complicated by a lack of available visually scanned "non-artifact" sources.

Fortunately, labeling data does not necessarily require humans to visually inspect images. Bloom et al. (2012) discuss a variety of methods for labeling detections of variability produced by difference imaging pipelines, including scanning alternatives such as artificial source construction and spectroscopic follow-up. Scanning, spectroscopy, and using fake data each have their respective merits and drawbacks. Scanning is laborious and potentially inaccurate, especially if each data instance is only examined by one scanner, or if scanners are not well trained. However, a large group of scanners can quickly label a number of detections sufficient to create a training set for a machine classifier, and Brink et al. (2013) have shown that the supervised classification algorithm Random Forest, which was ultimately selected for `autoScan`, is insensitive to mislabeled training data up to a contamination level of 10 percent.

Photometric typing (e.g., Sako et al. 2011) can also be useful for labeling detections of transients. However, robust photometric typing requires well-sampled light curves, which in turn require high-cadence photometry of difference image objects over timescales of weeks or months. This requirement is prohibitive for imaging surveys in their early stages. Further, because photometric typing is an integral part of the spectroscopic target selection process, by extension new imaging surveys also have too few detections of spectroscopically confirmed SNe, AGN, or variable stars. Native spectroscopic training samples are therefore impractical sources of training data for new surveys.

Artificial source construction is the fastest method for generating native detections of non-artifact sources in the early stages of a survey. Large numbers of artificial transients ("fakes") can be injected into survey science images, and by construction their associated detections are true positives. Difficulties can arise when the joint feature distributions of fakes selected for the training set do not approximate the joint feature distributions of observed transients in production. In DES-SN, SN Ia fluxes from fake SN Ia light curves are overlaid on images near real galaxies. The fake SN Ia light curves are generated by the `SNANA` simulation (Kessler et al. 2009), and they include true parent populations of stretch and color, a realistic model of intrinsic scatter, a redshift range from 0.1 to 1.4, and a galaxy location proportional to surface brightness. On difference images, detections of overlaid fakes are visually indistinguishable from real point-source transients and Solar System objects moving slowly enough not to streak. All fake SN Ia light curves are generated and stored prior to the start of the survey. The overlay procedure is part of the difference imaging pipeline, where the SN Ia flux added to the image is scaled by the zero point, spread over nearby pixels using a model of the PSF, and fluctuated by random Poisson noise. These fakes are used to monitor the single-epoch transient detection efficiency, as well as the candidate efficiency in which detections on two distinct nights are required. On average, six detections of fake SNe are overlaid on each single-epoch CCD-image.

The final `autoScan` training set contained detections of visually scanned artifacts and artificial sources only. We did not include detections of photometrically typed transients to

minimize the contamination of the "Non-Artifact" class with false positives. Bailey et al. (2007) also used a training set in which the "Non-Artifact" class consisted largely of artificial sources.

With 898,963 training instances in total, the `autoScan` training set is the largest used for difference image artifact rejection in production. It was split roughly evenly between "real" and "artifact" labeled instances—454,092 were simulated SNe Ia injected onto host galaxies, while the remaining 444,871 detections were human-scanned artifacts. Compiling a set of artifacts to train `autoScan` was accomplished by taking a random sample of the objects that had been scanned as artifacts by humans during an early processing of DES Y1 data with a pared-down version of the difference imaging pipeline presented in Figure 2.2.

2.3.2 Features and Processing

The supervised learning algorithms we consider in this analysis are nonlinear functions that map points representing individual detections in feature space to points in a space of object classes or class probabilities. The second design choice in developing `autoScan` is therefore to define a suitable feature space in which to represent the data instances we wish to use for training, validation, and prediction. In this section, we describe the classification features that we computed from the raw output of the difference imaging pipeline, as well as the steps used to pre- and post-process these features.

Data Preprocessing

The primary data sources for `autoScan` features are 51×51 pixel object-centered search, template, and difference image cutouts. The template and difference image cutouts are sky-subtracted. The search image cutout is sky-subtracted if and only if it does not originate from a coadded exposure, though this is irrelevant for what follows as no features are directly computed from search image pixel values. Photometric measurements, `SExtractor` output parameters, and other data sources are also used. Each cutout associated with a detection is compressed to 25×25 pixels. The seeing for each search image is usually no less than 1 arcsec, while the DECam pixel scale lies between 0.262 and 0.264 arcsec depending on the location on the focal plane, so little information is lost during compression. Although some artifacts are sharper than the seeing, we found that using compressed cutouts to compute some features resulted in better performance.

Consider a search, template, or difference image cutout associated with a single detection. Let the matrix element $\mathbf{I}_{x,y}$ of the 51×51 matrix $\mathbf{I}$ represent the flux-value of the pixel at location x, y on the cutout. We adopt the convention of zero-based indexing and the convention that element (0, 0) corresponds to the pixel at the top left-hand corner of the cutout. Let the matrix element $C_{x,y}$ of the 25×25 matrix C represent the flux-value of the pixel at location x, y on the compressed cutout. Then C is defined element-wise from $\mathbf{I}$ via

$$C_{x,y} = \frac{1}{N_u} \sum_{i=0}^{1} \sum_{j=0}^{1} \mathbf{I}_{2x+i,2y+j}, \tag{2.1}$$

where N_u is the number of unmasked pixels in the sum. Masked pixels are excluded from the sum. Only when all four terms in the sum represent masked pixels is the corresponding pixel masked in C. Note that matrix elements from the right-hand column and last row of $\mathbf{I}$ never appear in Equation 2.1.

To ensure that the pixel flux-values across cutouts are comparable, we rescale the pixel values of each compressed cutout via:

$$R_{x,y} = \frac{C_{x,y} - \text{med}(C)}{\hat{\sigma}}, \tag{2.2}$$

where the matrix element $R_{x,y}$ of the 25×25 matrix R represents the flux-value of the pixel at location x, y on the compressed, rescaled cutout, and $\hat{\sigma}$ is a consistent estimator of the standard deviation of C. We take the median absolute deviation as a consistent estimator of the standard deviation (Rousseeuw & Croux 1993), according to

$$\hat{\sigma} = \frac{\text{med}(|C - \text{med}(C)|)}{\Phi^{-1}\left(\frac{3}{4}\right)} \tag{2.3}$$

where $1/\Phi^{-1}(3/4) \approx 1.4826$ is the reciprocal of the inverse cumulative distribution for the standard normal distribution evaluated at $3/4$. This is done to ensure that the effects of defective pixels and cosmic rays nearly perpendicular to the focal plane are suppressed. We therefore have the following closed-form expression for the matrix element $R_{x,y}$,

$$R_{x,y} \approx \frac{1}{1.4826}\left[\frac{C_{x,y} - \text{med}(C)}{\text{med}(|C - \text{med}(C)|)}\right]. \tag{2.4}$$

The rescaling expresses the value of each pixel on the compressed cutout as the number of standard deviations above the median. Masked pixels are excluded from the computation of the median in Equation 2.4.

Finally, an additional rescaling from Brink et al. (2013) is defined according to

$$\mathbf{B}_{x,y} = \frac{\mathbf{I}_{x,y} - \text{med}(\mathbf{I})}{\max(|\mathbf{I}|)} \tag{2.5}$$

The size of $\mathbf{B}$ is 51×51. We found that using $\mathbf{B}$ instead of R or $\mathbf{I}$ to compute certain features resulted in better classifier performance. Masked pixels are excluded from the computation of the median in Equation 2.5.

Feature Library

Two feature libraries were investigated. The first was primarily "pixel-based." For a given object, each matrix element of the rescaled, compressed search, template, and difference cutouts was used as a feature. The CCD ID number of each detection was also used, as DECam has 62 CCDs with specific artifacts (such as bad columns and hot pixels) as well as

effects that are reproducible on the same CCD depending on which field is observed (such as bright stars). The signal-to-noise ratio of each detection was also used as a feature. The merits of this feature space include relatively straightforward implementation and computational efficiency. A production version of this pixel-based classifier was implemented in the DES-SN transient detection pipeline at the beginning of Y1. In production, it became apparent that the 1,877-dimensional[2] feature space was dominated by uninformative features, and that better false positive control could be achieved with a more compact feature set.

We pursued an alternative feature space going forward, instead using 38 high-level metrics to characterize detections of variability. A subset of the features are based on analogs from Bloom et al. (2012) and Brink et al. (2013). In this section, we describe the features that are new. We present an at-a-glance view of the entire `autoScan` feature library in Table 2.2. Histograms and contours for the three most important features in the final `autoScan` model (see §2.3.4) appear in Figure 2.4.

[2] 625 pixels on a 25×25 pixel cutout $\times$ 3 cutouts per detection + 2 non-pixel features (`snr`, `ccdid`) = 1,877.

Table 2.2: `autoScan`'s feature library.

Feature Name	Importance	Source	Description
`r_aper_psf`	0.148	New	The average flux in a 5-pixel circular aperture centered on the object on the $\mathbf{I}^t$ cutout plus the flux from a 35×35-pixel PSF model-fit to the object on the $\mathbf{I}^d$ cutout, all divided by the PSF model-fit flux.
`magdiff`	0.094	B12	If a source is found within 5" of the location of the object in the galaxy coadd catalog, the difference between `mag` and the magnitude of the nearby source. Else, the difference between `mag` and the limiting magnitude of the parent image from which the $\mathbf{I}^d$ cutout was generated.
`spread_model`	0.066	New	`SPREAD_MODEL` output parameter from `SExtractor` on $\mathbf{I}^d$.
`n2sig5`	0.055	B12	Number of matrix elements in a 7×7 element block centered on the detection on R^d with values less than -2.
`n3sig5`	0.053	B12	Number of matrix elements in a 7×7 element block centered on the detection on R^d with values less than -3.
`n2sig3`	0.047	B12	Number of matrix elements in a 5×5 element block centered on the detection on R^d with values less than -2.
`flux_ratio`	0.037	B12	Ratio of the flux in a 5-pixel circular aperture centered on the location of the detection on $\mathbf{I}^d$ to the absolute value of the flux in a 5-pixel circular at the same location on $\mathbf{I}^t$.
`n3sig3`	0.034	B12	Number of matrix elements in a 5×5 element block centered on the detection on R^d with values less than -3.
`mag_ref_err`	0.030	B12	Uncertainty on `mag_ref`, if it exists. Else imputed.
`snr`	0.029	B12	The flux from a 35×35-pixel PSF model-fit to the object on $\mathbf{I}^d$ divided by the uncertainty from the fit.
`colmeds`	0.028	New	The maximum of the median pixel values of each column on $\mathbf{B}^d$.

Table 2.2 (cont'd): `autoScan`'s feature library.

Feature Name	Importance	Source	Description
`nn_dist_renorm`	0.027	B12	The distance from the detection to the nearest source in the galaxy coadd catalog, if one exists within 5". Else imputed.
`ellipticity`	0.027	B12	The ellipticity of the detection on $\mathbf{I}^d$ using `a_image` and `b_image` from `SExtractor`.
`amp`	0.027	B13	Amplitude of fit that produced `gauss`.
`scale`	0.024	B13	Scale parameter of fit that produced `gauss`.
`b_image`	0.024	B12	Semi-minor axis of object from `SExtractor` on $\mathbf{I}^d$.
`mag_ref`	0.022	B12	The magnitude of the nearest source in the galaxy coadd catalog, if one exists within 5" of the detection on $\mathbf{I}^d$. Else imputed.
`diffsum`	0.021	New	The sum of the matrix elements in a 5×5 element box centered on the detection location on R^d.
`mag`	0.020	B12	The magnitude of the object from `SExtractor` on $\mathbf{I}^d$.
`a_ref`	0.019	B12	Semi-major axis of the nearest source in the galaxy coadd catalog, if one exists within 5". Else imputed.
`n3sig3shift`	0.019	New	The number of matrix elements with values greater than or equal to 3 in the central 5×5 element block of R^d minus the number of matrix elements with values greater than or equal to 3 in the central 5×5 element block of R^t.
`n3sig5shift`	0.018	New	The number of matrix elements with values greater than or equal to 3 in the central 7×7 element block of R^d minus the number of matrix elements with values greater than or equal to 3 in the central 7×7 element block of R^t
`n2sig3shift`	0.014	New	The number of matrix elements with values greater than or equal to 2 in the central 5×5 element block of R^d minus the number of matrix elements with values greater than or equal to 2 in the central 5×5 element block of R^t.

Table 2.2 (cont'd): `autoScan`'s feature library.

Feature Name	Importance	Source	Description
`b_ref`	0.012	B12	Semi-minor axis of the nearest source in the galaxy coadd catalog, if one exists within 5". Else imputed.
`gauss`	0.012	B13	χ^2 from fitting a spherical, 2D Gaussian to a 15×15 pixel cutout around the detection on $\mathbf{B}^d$.
`n2sig5shift`	0.012	New	The number of matrix elements with values greater than or equal to 2 in the central 7×7 element block of R^d minus the number of matrix elements with values greater than or equal to 2 in the central 7×7 element block of R^t.
`mag_from_limit`	0.010	B12	Limiting magnitude of the parent image from which the I^d cutout was generated minus `mag`.
`a_image`	0.009	B12	Semi-major axis of object on $\mathbf{I}^d$ from `SExtractor`.
`min_dist_to_edge`	0.009	B12	Distance in pixels to the nearest edge of the detector array on the parent image from which the I^d cutout was generated.
`ccdid`	0.008	B13	The numerical ID of the CCD on which the detection was registered.
`flags`	0.008	B12	Numerical representation of `SExtractor` extraction flags on $\mathbf{I}^d$.
`numneg`	0.007	New	The number of negative matrix elements in a 7×7 element box centered on the detection in R^d.
`l1`	0.006	B13	$\text{sign}(\sum \mathbf{B}^d) \times \sum \lvert\mathbf{B}^d\rvert / \lvert\sum \mathbf{B}^d\rvert$
`lacosmic`	0.006	New	$\max(\mathbf{B}^d)/\max(F)$, where F is the `LACosmic` (van Dokkum 2001) "fine structure" image computed on $\mathbf{B}^d$.

Table 2.2 (cont'd): `autoScan`'s feature library.

Feature Name	Importance	Source	Description
`spreaderr_model`	0.006	New	Uncertainty on `spread_model`.
`maglim`	0.005	B12	True if there is no nearby galaxy coadd source, false otherwise.
`bandnum`	0.004	New	Numerical representation of image filter.
`maskfrac`	0.003	New	The fraction of $\mathbf{I}^d$ that is masked.

Note. — Source column indicates the reference in which the feature was first published. B13 indicates the feature first appeared in Brink et al. (2013); B12 indicates the feature first appeared in Bloom et al. (2012), and New indicates the feature is new in this work. See §2.3.3 for an explanation of how feature importances are computed. Imputation refers to the procedure described in §2.3.2.

New Features

In this section we present new features developed for `autoScan`. Let the superscripts s, t, and d on matrices defined in the previous section denote search, template, and difference images, respectively. The feature `r_aper_psf` is designed to identify badly subtracted stars and galaxies on difference images caused by poor astrometric alignment between search and template images. These objects typically appear as overlapping circular regions of positive and negative flux colloquially known as "dipoles." Examples are presented in Figure 2.3. In these cases the typical search-template astrometric misalignment scale is comparable to the FWHM of the PSF, causing the contributions of the negative and positive regions to the total object-flux from a PSF-model fit to be approximately equal in magnitude but opposite in sign, usually with a slight positive excess as the PSF-fit is centered on the detection location, where the flux is always positive. The total flux from a PSF-model fit to a dipole is usually greater than but comparable to the average flux per pixel in a five-pixel circular aperture centered on the detection location on the template image. To this end, let $F_{aper,I}$ be the flux from a five-pixel circular aperture centered on the location of a detection on the uncompressed template image. Let $F_{PSF,I}$ be the flux computed by fitting a PSF-model to a 35×35 pixel cutout centered on the location of the detection on the uncompressed difference image. Then `r_aper_psf` is given by

$$\texttt{r_aper_psf} = \frac{F_{aper,I} + F_{PSF,I}}{F_{PSF,I}}. \tag{2.6}$$

We find that objects with `r_aper_psf` > 1.25 are almost entirely "dipoles."

Let $a \in \{2, 3\}$, $b \in \{3, 5\}$. The four features `n`a`sig`b`shift` represent the difference between the number of pixels with flux values greater than or equal to a in $(b+2) \times (b+2)$ element blocks centered on the detection position in R^d and R^t. These features coarsely describe

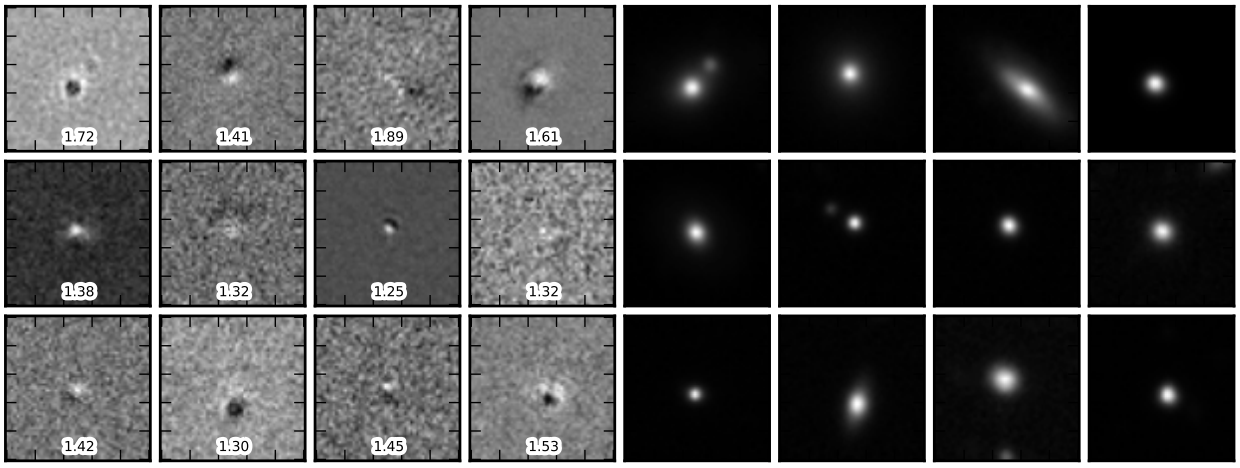

Figure 2.3: Difference image cutouts (left four columns; `r_aper_psf` values indicated) and corresponding template image cutouts (right four columns) for objects with `r_aper_psf` > 1.25.

changes in the morphology of the source between the template and search images.

The feature `diffsum` is the sum of the matrix elements in a 5×5 element ($2.8 \times 2.8\,\mathrm{arcsec}^2$) box centered on the detection location in R^d. It is given by

$$\texttt{diffsum} = \sum_{i=-2}^{2} \sum_{j=-2}^{2} R^d_{x_c+i, y_c+j}, \tag{2.7}$$

where x_c, y_c is the location of the central element on R^d. It gives a coarse measurement of the significance of the detection.

`bandnum` is a numeric representation of the filter in which the object was detected on the search image. This feature enables `autoScan` to identify band-specific patterns.

`numneg` is intended to assess object-smoothness by returning the number of negative elements in a 7×7 pixel box centered on the object in R^d, exposing objects riddled with negative pixels or objects that have a significant number of pixels below $\mathrm{med}(R^d)$. Used in concert with the S/N, `numneg` can help identify high-S/N objects with spatial pixel intensity distributions that do not vary smoothly, useful in rejecting hot pixels and cosmic rays.

`lacosmic` was designed to identify cosmic rays and other objects with spatial pixel intensity distributions that do not vary smoothly, and is based loosely on the methodology that van Dokkum (2001) uses to identify cosmic rays on arbitrary sky survey images. Derive the "fine structure" image $\mathbf{F}$ from $\mathbf{B}^d$ according to

$$\mathbf{F} = (M_3 * \mathbf{B}^d) - ([M_3 * \mathbf{B}^d] * M_7), \tag{2.8}$$

where M_n is an $n \times n$ median filter. Then

$$\texttt{lacosmic} = \max(\mathbf{B}^d) / \max(\mathbf{F}). \tag{2.9}$$

Relatively speaking, this statistic should be large for objects that do not vary smoothly, and small for objects that approximate a PSF. The reader is referred to Figure 3 of van Dokkum (2001) for visual examples.

Bad columns and CCD edge effects that appear as fuzzy vertical streaks near highly masked regions of difference images are common types of artifacts. Because they share a number of visual similarities, we designed a single feature, `colmeds`, to identify them:

$$\texttt{colmeds} = \max(\{\text{med}(\text{transpose}(\mathbf{B}^d)_i); \\ i \in \{0 \ldots N_{col} - 1\}\}), \tag{2.10}$$

where N_{col} is the number of columns in $\mathbf{B}^d$. This feature operates on the principle that the median of a column in $\mathbf{B}^d$ should be comparable to the background if the cutout is centered on a PSF, because, in general, even the column in which the PSF is at its greatest spatial extent in $\mathbf{B}^d$ should still contain more background pixels than source pixels. However, for vertically oriented artifacts that occupy entire columns on $\mathbf{B}^d$, this does not necessarily hold. Since these artifacts frequently appear near masked regions of images, we define `maskfrac` as the percentage of $\mathbf{I}^d$ that is masked.

The feature `spread_model` (Desai et al. 2012; Bouy et al. 2013) is a `SExtractor` star/galaxy separation output parameter computed on the $\mathbf{I}^d$ cutout. It is a normalized simplified linear discriminant between the best fitting local PSF model and a slightly more extended model made from the same PSF convolved with a circular exponential disk model.

Data Postprocessing

When there is not a source in the galaxy coadd catalog within 5 arcsec of an object detected on a difference image, certain classification features cannot be computed for the object (see Table 2.2). If the feature of an object cannot be computed, it is assigned the mean value of that feature from the training set.

2.3.3 Classification Algorithm Selection

After we settled on an initial library of classification features, we compared three well-known ML classification algorithms: a Random Forest (Breiman 2001), a Support Vector Machine (SVM; Vapnik 2013), and an AdaBoost decision tree classifier (Hastie et al. 2009). We used `scikit-learn` (Pedregosa et al. 2012), an open source Python package for machine learning, to instantiate examples of each model with standard settings. We performed a three-fold cross-validated comparison using a randomly selected 100,000-detection subset of the training set described in §2.3.1. The subset was used to avoid long training times for the SVM. For a description of cross validation and the metrics used to evaluate each model, see §2.4 and §2.4.2. The results appear in Figure 2.5. We found that the performance of all three models was comparable, but that the Random Forest outperformed the other models by a small margin. We incorporated the Random Forest model into `autoScan`.

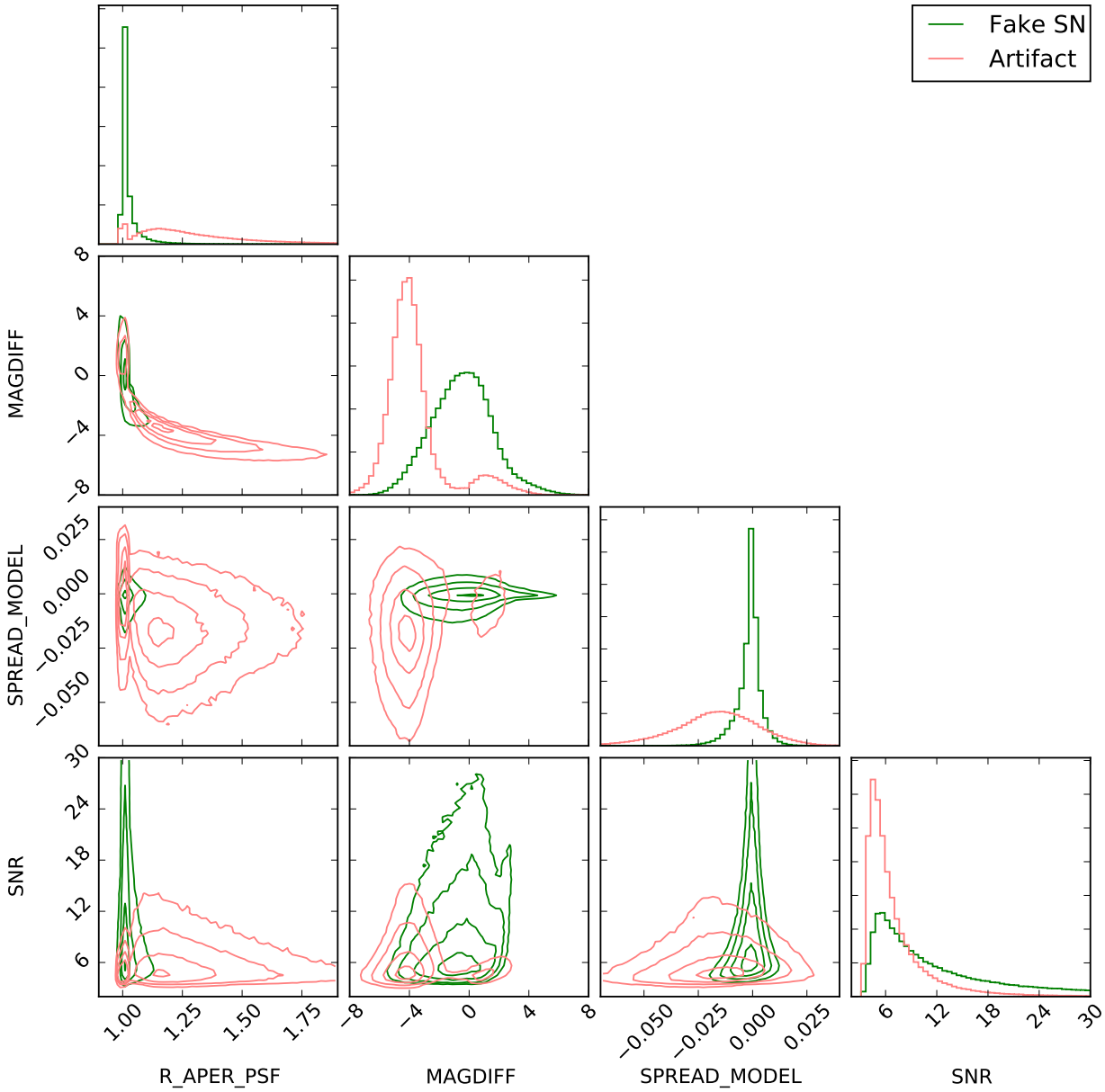

Figure 2.4: Contours of `r_aper_psf`, `magdiff`, and `spread_model`—the three most important features in the `autoScan` Random Forest model, computed using the feature importance evaluation scheme described in §2.3.4—and the signal-to-noise ratio, `snr`. The importances of `r_aper_psf`, `magdiff`, and `spread_model` were 0.148, 0.094, and 0.066, respectively. The contours show that the relationships between the features are highly nonlinear and better suited to machine learning techniques than hard selection cuts.

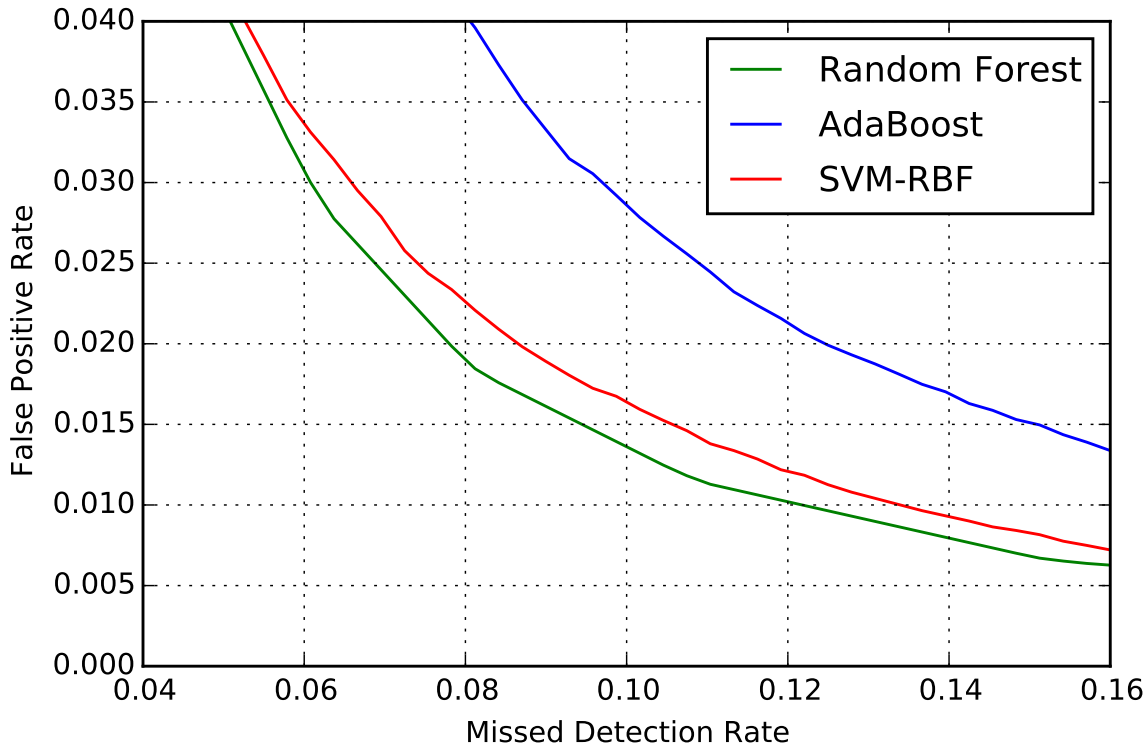

Figure 2.5: Initial comparison of the performance of a Random Forest, a Support Vector Machine with a radial basis function kernel, and an AdaBoost Decision Tree classifier on the DES-SN artifact/non-artifact classification task. Each classifier was trained on a randomly selected 67% of the detections from a 100,000-detection subset of the training set, then tested on the remaining 33%. This process was repeated three times until every detection in the subset was used in the testing set once. The curves above represent the mean of each iteration. The closer a curve is to the origin, the better the classifier. The unoptimized Random Forest outperformed the other two methods, and was selected.

Random Forests are collections of decision trees, or cascading sequences of feature-space unit tests, that are constructed from labeled training data. For an introduction to decision trees, see Breiman et al. (1984). Random Forests can be used for predictive classification or regression. During the construction of a supervised Random Forest classifier, trees in the forest are trained individually. To construct a single tree, the training algorithm first chooses a bootstrapped sample of the training data. The algorithm then attempts to recursively define a series of binary splits on the features of the training data that optimally separate the training data into their constituent classes. During the construction of each node, a random subsample of features with a user-specified size is selected with replacement. A fine grid of splits on each feature is then defined, and the split that maximizes the increase in the purity of the incident training data is chosen for the node.

Two popular metrics for sample-purity are the Gini coefficient (Gini 1921) and the Shannon entropy (Shannon 1948). Define the purity of a sample of difference image objects to be[3]

$$P = \frac{N_{NA}}{N_A + N_{NA}}, \tag{2.11}$$

where N_{NA} is the number of non-artifact objects in the sample, and N_A is the number of artifacts in the sample. Note that $P = 1$ for a sample composed entirely of artifacts, $P = 0$ for a sample composed entirely of non-artifacts, and $P(1 - P) = 0$ for a sample composed entirely of either artifacts or non-artifacts. Then the Gini coefficient is

$$\text{Gini} = P(1 - P)(N_A + N_{NA}). \tag{2.12}$$

A tree with a Gini objective function seeks at each node to minimize the quantity

$$\text{Gini}_{\text{lc}} + \text{Gini}_{\text{rc}}, \tag{2.13}$$

where Gini_{lc} is the Gini coefficient of the data incident on the node's left child, and Gini_{rc} is the Gini coefficient of the data incident on the node's right child. If $\text{Gini}_{\text{lc}} + \text{Gini}_{\text{rc}} > \text{Gini}$, then no split is performed and the node is declared a terminal node. The process proceeds identically if another metric is used, such as the Shannon entropy, the most common alternative. The Shannon entropy S of a sample of difference image objects is given by

$$S = -p_{NA}\log_2(p_{NA}) - p_A\log_2(p_A), \tag{2.14}$$

where p_{NA} is the proportion of non-artifact objects in the sample, and p_A is the proportion of artifacts in the sample.

Nodes are generated in this fashion until a maximum depth or a user-specified measure of node purity is achieved. The number of trees to grow in the forest is left as a free parameter

[3]Some authors define $P = \frac{\sum_{NA} w_i}{\sum_{NA} w_i + \sum_{A} w_i}$, where w_i is the weight of instance i, $\sum_A$ is a sum over artifact events, and $\sum_{NA}$ is a sum over non-artifact events. This renders the definition of the Gini coefficient in Equation 2.12 as $\text{Gini} = P(1 - P)\sum_i w_i$.

to be set by the user. Training a single Random Forest using the entire $\sim 900,000$ object training sample with the hyperparameters selected from the grid search described in Table 2.3 took ~ 4.5 minutes when the construction of the trees was distributed across 60 1.6GHz AMD Opteron 6262 HE processors.

Random Forests treat the classes of unseen objects as unknown parameters that are described probabilistically. An object to be classified descends each tree in the forest, beginning at the root nodes. Once a data point arrives at a terminal node, the tree returns the fraction of the training instances that reached that node that were labeled "non-artifact." The output of the trained `autoScan` Random Forest model on a single input data instance is the average of the outputs of each tree, representing the probability that the object is not an artifact, henceforth the "`autoScan` score" or "ML score." Ultimately, a score of 0.5 was adopted as the cut τ to separate real detections of astrophysical variability from artifacts in the DES-SN data; see §2.4.4 for details. Class prediction for 200,000 unseen data instances took 9.5s on a single 1.6GHz AMD Opteron 6262 HE processor.

2.3.4 Feature Importances

Numeric importances can be assigned to the features in a trained forest based on the amount of information they provided during training (Breiman et al. 1984). For each tree T in the forest, a tree-specific importance for feature i is computed according to

$$\zeta_{i,T} = \sum_{n \in T} N(n) B_i(n) \left[m(n) - m_{ch}(n) \right], \tag{2.15}$$

where n is an index over nodes in T, $N(n)$ is the number of training data points incident on node n, $B_i(n)$ is 1 if node n splits on feature i and 0 otherwise, $m(n)$ is the value of the objective function (usually the Gini coefficient or the Shannon entropy, see §2.3.3) applied to the the training data incident on node n, and $m_{ch}(n)$ is the sum of the values of the objective function applied to the node's left and right children. The global importance of feature i is the average of the tree-specific importances:

$$I_i = \frac{1}{N_T} \sum_T \zeta_{i,T}, \tag{2.16}$$

where N_T is the number of trees in the forest. In this article, importances are normalized to sum to unity.

2.3.5 Optimization

The construction of a Random Forest is governed by a number of free parameters called hyperparameters. The hyperparameters of the Random Forest implementation used in this work are `n_estimators`, the number of decision trees in the forest, `criterion`, the function that measures the quality of a proposed split at a given tree node, `max_features`, the number of features to randomly select when looking for the best split at a given tree node, `max_depth`,

Table 2.3: Grid search results for `autoScan` hyperparameters.

Hyperparameter	Values
`n_estimators`	10, 50, **100**, 300
`criterion`	`gini`, **entropy**
`max_features`	5, **6**
`min_samples_split`	2, **3**, 4, 10, 20, 50
`max_depth`	**Unlimited**, 100, 30, 15, 5

Note. — A 3-fold cross-validated search over the grid of Random Forest hyperparameters tabulated above was performed to characterize the the performance of the machine classifier. The hyperparameters of the best-performing classifier appear in bold.

the maximum depth of a tree, and `min_samples_split`, the minimum number of samples required to split an internal node.

We performed a 3-fold cross-validated (see §2.4.2) grid search over the space of Random Forest hyperparameters described in Table 2.3. A total of 1,884 trainings were performed. The best classifier had 100 trees, used the Shannon entropy objective function, chose 6 features for each split, required at least 3 samples to split a node, and had unlimited depth, and it was incorporated into the code. Recursive feature elimination (Brink et al. 2013) was explored to improve the performance of the classifier, but we found that it provided no statistically significant performance improvement.

2.4 Performance

In this section, we describe performance of `autoScan` on a realistic classification task and the effect of the code on the DES-SN transient candidate scanning load. Performance statistics for the classification task were measured using production Y1 data, whereas candidate-level effects were measured using a complete reprocessing of Y1 data using an updated difference imaging pipeline. The reprocessed detection pool differed significantly from its production counterpart, providing a out-of-sample data set for benchmarking the effects of the code on the scanning load.[4]

[4] Although the re-processing of data through the difference imaging pipeline from the raw images is not useful for getting spectra of live transients, it is quite useful for acquiring host-galaxy targets for previously missed transients and is therefore performed regularly as pipeline improvements are made.

2.4.1 Performance Metrics

The performance of a classifier on an n-class task is completely summarized by the corresponding $n \times n$ confusion matrix $\mathbb{E}$, also known as a contingency table or error matrix. The matrix element $\mathbb{E}_{ij}$ represents the number of instances from the task's validation set with ground truth class label j that were predicted to be members of class i. A schematic 2×2 confusion matrix for the `autoScan` classification task is shown in Figure 2.6.

From the confusion matrix, several classifier performance metrics can be computed. Two that frequently appear in the literature are the False Positive Rate (FPR) and the Missed Detection Rate (MDR; also known as the False Negative Rate or False Omission Rate). Using the notation from Figure 2.6, the FPR is defined by:

$$FPR = \frac{F_p}{F_p + T_n}, \tag{2.17}$$

and the missed detection rate by

$$MDR = \frac{F_n}{T_p + F_n}. \tag{2.18}$$

For `autoScan`, the FPR represents the fraction of artifacts in the validation set that are predicted to be legitimate detections of astrophysical variability. The MDR represents the fraction of non-artifacts in the task's validation set that are predicted to be artifacts. Another useful metric is the efficiency or True Positive Rate (TPR),

$$\epsilon = \frac{T_p}{T_p + F_n}, \tag{2.19}$$

which represents the fraction of non-artifacts in the sample that are classified correctly. For the remainder of this study, we often refer to the candidate-level efficiency measured on fake SNe Ia, ϵ_F (see §2.4.4).

Finally, the receiver operating characteristic (ROC) is a graphical tool for visualizing the performance of a classifier. It displays FPR as a function of MDR, both of which are parametric functions of τ, the `autoScan` score that one chooses to delineate the boundary between "non-artifacts" and "artifacts." One can use the ROC to determine the location at which the trade-off between the FPR and MDR is optimal for the survey at hand, a function of both the scanning load and the potential bias introduced by the classifier, then solve for the corresponding τ. By benchmarking the performance of the classifier using the the ROC, one can paint a complete picture of its performance that can also serve as a statistical guarantee on performance in production, assuming a validation set and a production data set that are identically distributed in feature space, and that detections are scanned individually in production (see §2.4.4).

2.4.2 Classification Task

We used stratified 5-fold cross-validation to test the performance of `autoScan`. Cross validation is a technique for assessing how the results of a statistical analysis will generalize to

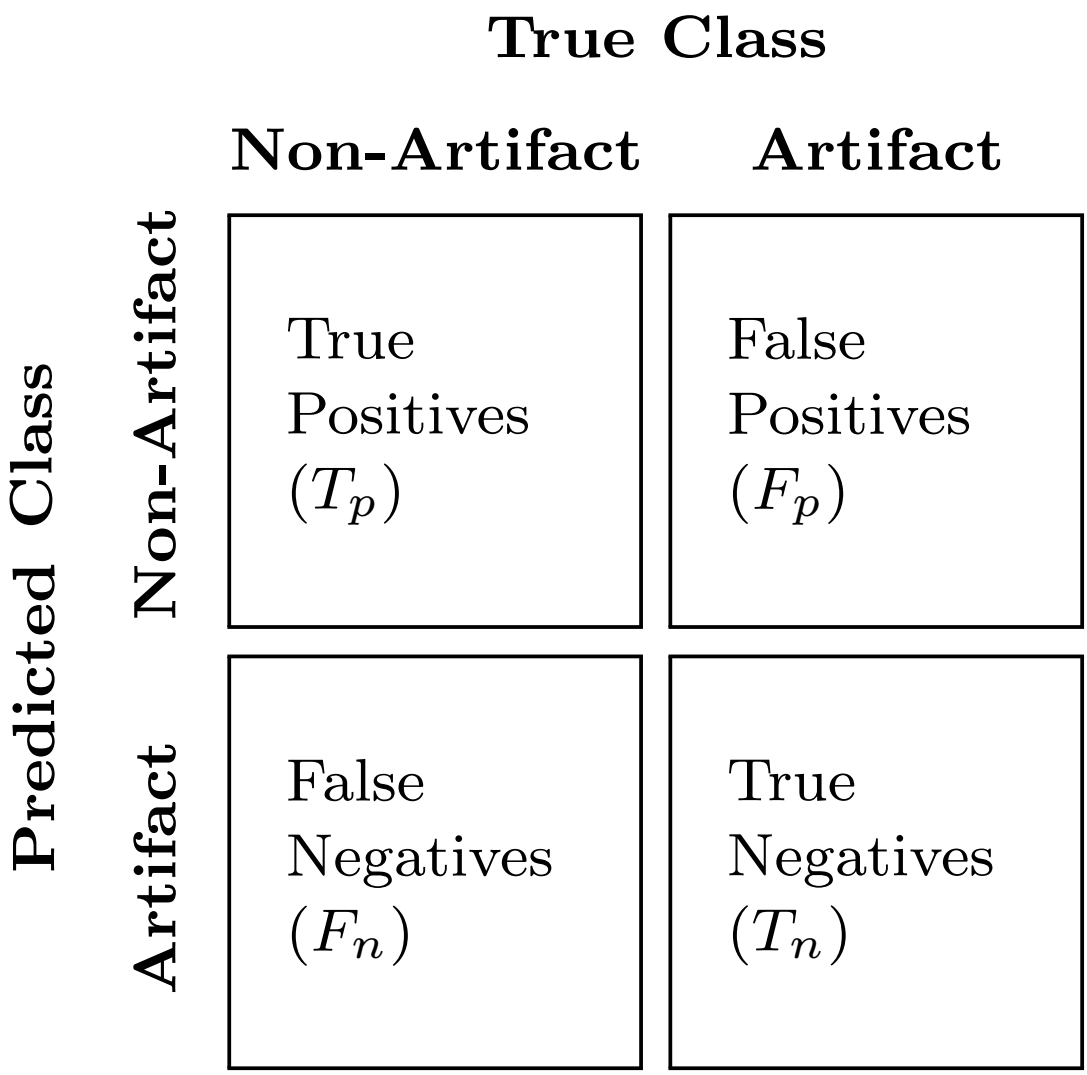

Figure 2.6: Schematic confusion matrix for the `autoScan` classification task. Each matrix element $\mathbb{E}_{ij}$ represents the number of instances from the task's validation set with ground truth class label j that were predicted to be members of class i.

an independent data set. In a k-fold cross-validated analysis, a data set is partitioned into k disjoint subsets. k iterations of training and testing are performed. During the ith iteration, subset i is held out as a "validation" set of labeled data instances that are not included in the training sample, and the union of the remaining $k-1$ subsets is passed to the classifier as a training set. The classifier is trained and its predictive performance on the validation set is recorded. In standard k-fold cross-validation, the partitioning of the original data set into disjoint subsets is done by drawing samples at random without replacement from the original data set. But in a stratified analysis, the drawing is performed subject to the constraint that the distribution of classes in each subset be the same as the distribution of classes in the original data set. Cross-validation is useful because it enables one to characterize how a classifier's performance varies with respect to changes in the composition of training and testing data sets, helping quantify and control "generalization error."

2.4.3 Results

Figure 2.7 shows the ROCs that resulted from each round of cross-validation. We report that `autoScan` achieved an average detection-level MDR of 4.0 ± 0.1 percent at a fixed FPR of 2.5 percent with $\tau = 0.5$, which was ultimately adopted in the survey; see §2.4.4. We found that `autoScan` scores were correlated with detection signal-to-noise ratio (S/N). Figure 4.12 displays the fake efficiency and false positive of `autoScan` using all out-of-sample detections of fake SNe from each round of cross-validation. At S/N $\lesssim 10$, the out-of-sample fake efficiency is markedly lower than it is at higher S/N. The efficiency asymptotically approaches unity for S/N $\gtrsim 100$. The effect becomes more pronounced when the class discrimination boundary is raised. This occurs because legitimate detections of astrophysical variability at low S/N are similar to artifacts. The false positive rate remains relatively constant in the S/N $\lesssim 10$ regime, where the vast majority of artifacts reside.

2.4.4 Effect of `autoScan` on Transient Candidate Scanning Load

As discussed in §2.2, DES-SN performs target selection and scanning using aggregates of spatially coincident detections from multiple nights and filters ("candidates"). After the implementation of `autoScan`, the `NUMEPOCHS` requirement described in Table 2.1 was revised to require that a candidate be detected on at least two distinct nights having at least one detection with an ML score greater than τ to become eligible for visual scanning. In this section we describe the effect of this revision on the scanning load for an entire observing season using a full reprocessing of the Y1 data.

We sought to minimize the size of our transient candidate scanning load with no more than a 1 percent loss in ϵ_F. By performing a grid search on τ, we found that we were able to reduce the number of candidates during the first observing season of DES-SN by a factor of 13.4, while maintaining $\epsilon_F > 99.0$ per cent by adopting $\tau = 0.5$. After implementing `autoScan` using this τ, we measured the quantity $\langle N_A/N_{NA} \rangle$, the average ratio of artifact objects to non-artifact detections that a human scanner encountered during a scanning session,

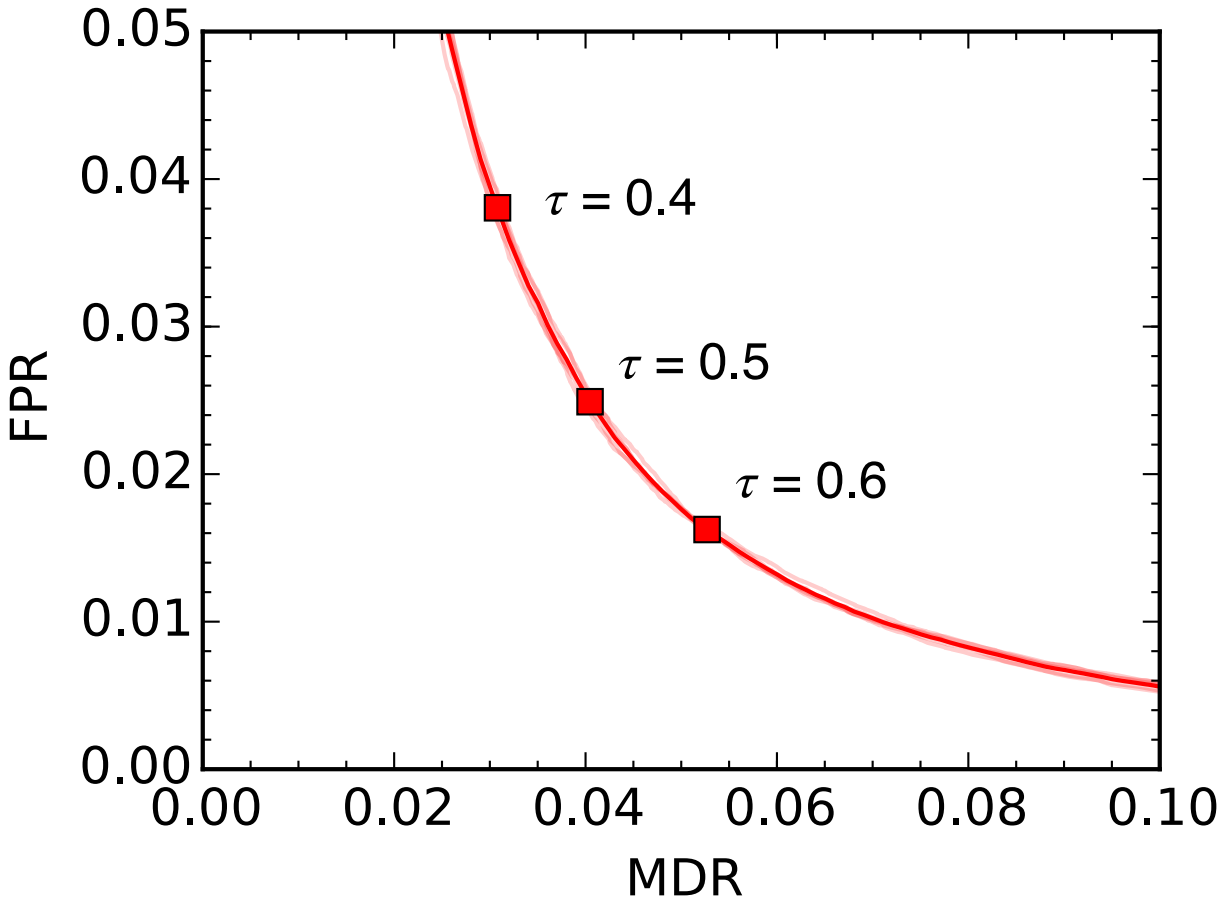

Figure 2.7: 5-fold cross-validated receiver operating characteristics of the best-performing classifier from §2.3.5. Six visually indistinguishable curves are plotted: one translucent curve for each round of cross-validation, and one opaque curve representing the mean. Points on the mean ROC corresponding to different class discrimination boundaries τ are labeled. $\tau = 0.5$ was adopted in DES-SN.

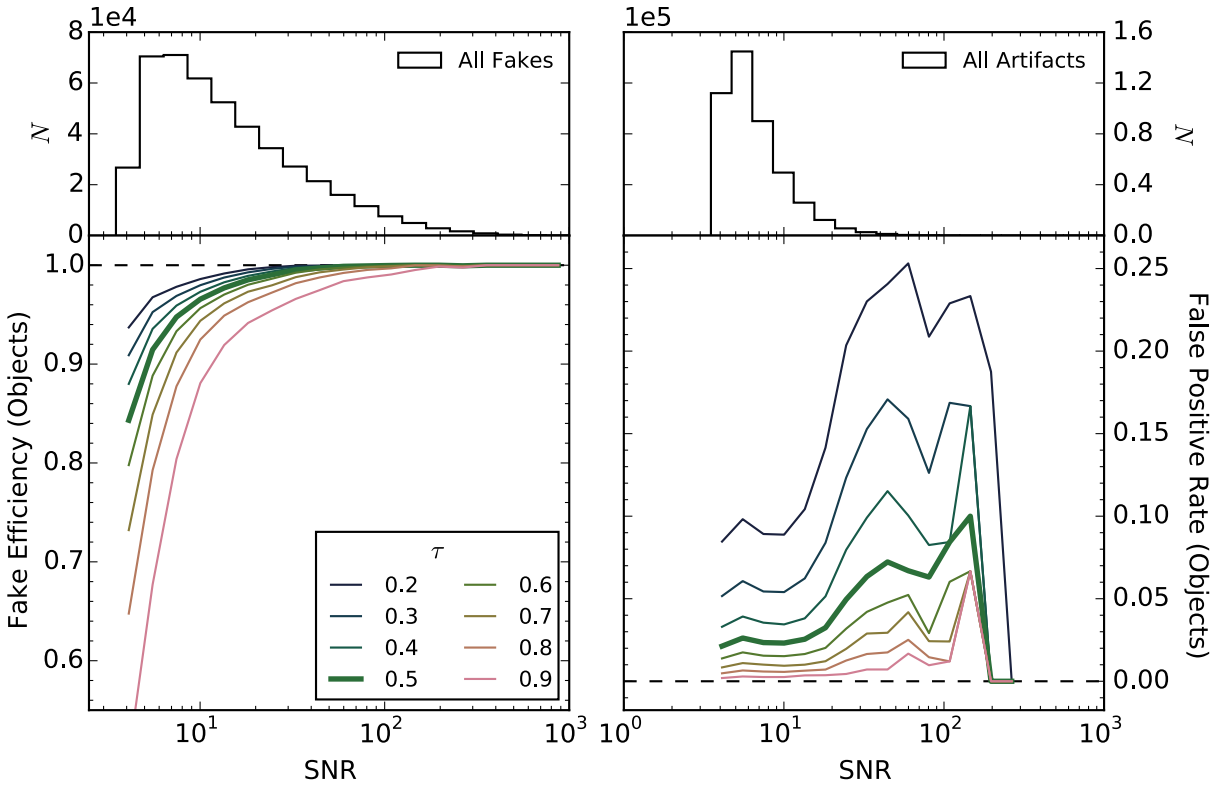

Figure 2.8: Object-level fake efficiency and false positive rate as a function of S/N, at several `autoScan` score cuts. The S/N is computed by dividing the flux from a PSF-model fit to a 35×35 pixel cutout around the object in the difference image by the uncertainty from the fit. The artifact rejection efficiency and missed detection rate are 1 minus the false positive rate and fake efficiency, respectively. The fake efficiency of `autoScan` degrades at low S/N, whereas the false positive rate is relatively constant in the S/N regime not dominated by small number statistics. $\tau = 0.5$ (bold) was adopted in DES-SN.

Table 2.4: Effect of `autoScan` on Reprocessed DES Y1 Transient Candidate Scanning Load.

	No ML	ML ($\tau = 0.5$)	ML / No ML
N_c[a]	100,450	7,489	0.075
$\langle N_A/N_{NA}\rangle$[b]	13	0.34	0.027
ϵ_F[c]	1.0	0.990	0.990

[a]Total number of science candidates discovered.
[b]Average ratio of artifact to non-artifact detections in human scanning pool determined from scanning 3,000 randomly selected detections from all science candidate detections.
[c]`autoScan` candidate-level efficiency for fake SNe Ia.

using random samples of 3,000 objects drawn from the pool of objects passing the modified and unmodified cuts in Table 2.1. We found that the ratio decreased by a factor of roughly 40 after the production implementation of `autoScan`. Table 2.4 summarizes these results.

2.5 Discussion

With the development of `autoScan` and the use of fake overlays to robustly measure efficiencies, the goal of automating artifact rejection on difference images using supervised ML classification has reached a certain level of maturity. With several historical and ongoing time-domain surveys using ML techniques for candidate selection, it is clear that the approach has been successful in improving astrophysical source selection efficiency on images. However, there are still several ways the process could be improved for large-scale transient searches of the future, especially for ZTF and LSST, whose demands for reliability, consistency, and transparency will eclipse those of contemporary surveys.

2.5.1 Automating Artifact Rejection in Future Surveys

For surveys like LSST and ZTF, small decreases in MDR are equivalent to the recovery of vast numbers of new and interesting transients. Decreasing the size of the feature set and increasing the importance of each feature is one of the most direct routes to decreasing MDR. However, designing and engineering effective classification features is among the most time-consuming and least intuitive aspects of framework design. Improving MDR by revising feature sets is a matter of trial and error—occasionally, performance improvements can result, but sometimes adding features can degrade the performance of a classifier. Ideally, surveys that will retrain their classifiers periodically will have a rigorous, deterministic procedure to extract the optimal feature set from a given training data set. This is possible with the use of convolutional neural networks (CNNs), a subclass of Artificial Neural Networks, that can take images as input and infer an optimal set of features for a given set of training

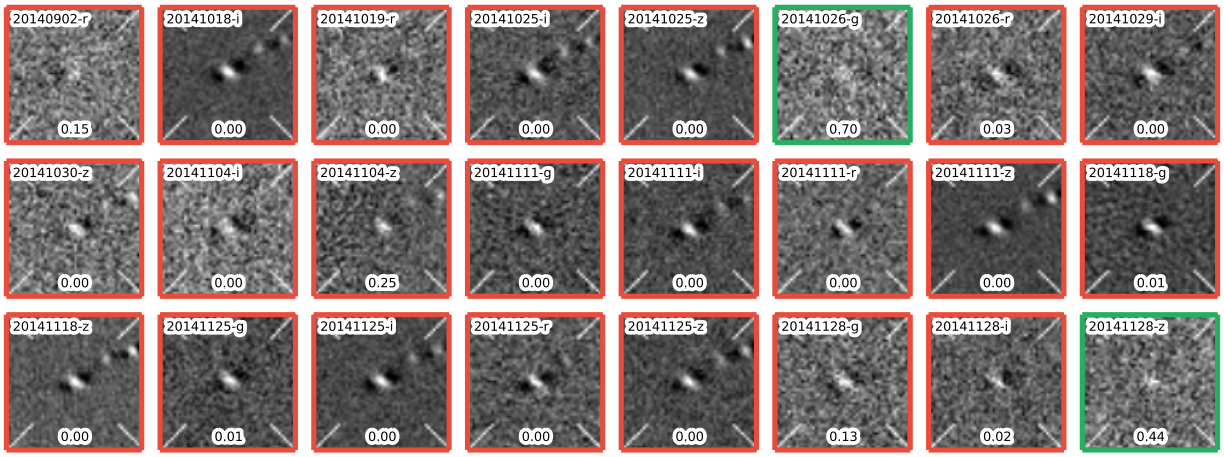

Figure 2.9: 24 consecutively observed difference image cutouts of a poorly subtracted galaxy that was wrongly identified as a transient. The `autoScan` score of each detection appears at the bottom of each cutout. The mis-identification occurred because on two nights the candidate had a detection that received a score above an `autoScan` class discrimination boundary $\tau = 0.4$ used during early code tests (green boxes). Night-to-night variations in observing conditions, data reduction, and image subtraction can cause detections of artifacts to appear real. If a two-night trigger is used, spurious "transients" like this one can can easily accumulate as a season goes on. Consequently, care must be taken when using an artifact rejection framework that scores individual detections to make statements about aggregates of detections. Each image is labeled with the observation date and filter for the image, in the format YYYYMMDD-filter.

data. The downside to CNNs is that the resulting features are significantly more abstract than astrophysically motivated features and consequently can be more difficult to interpret, especially in comparison with Random Forests, which assign each feature a relative importance. However, CNNs have achieved high levels of performance for a diverse array of problems. They remain relatively unexplored in the context of astrophysical data processing, and bear examination for use in future surveys.

Next, unless great care is taken to produce a training data set that is drawn from the same multidimensional feature distribution as the testing data, dense regions of testing space might be completely devoid of training data, leading to an unacceptable degradation of classification accuracy in production. Developing a rigorous method for avoiding such sample selection bias is crucial for future surveys, for which small biases in the training set can result in meaningful losses in efficiency. The idea of incorporating active learning techniques into astronomical ML classification frameworks has been advanced as a technique for reducing sample selection bias (Richards et al. 2012).

Given a testing set and a training set which are free to be drawn from different distributions in feature space, in the pool-based active learning for classification framework, an algorithm iteratively selects, out of the entire set of unlabeled data, the object (or set of objects) that would give the maximum performance gains for the classification model, if its true label were known. The algorithm then solicits a user to manually input the class of the object under consideration, and then the object is automatically incorporated into future training sets to improve upon the original classifier. Under this paradigm, human scanners would play the valuable role of helping the classifier learn from its mistakes, and each human hour spent vetting data would immediately carry scientific return. Active learning could produce extremely powerful classifiers over short timescales when used in concert with generative models for training data. Instead of relying on historical data to train artifact rejection algorithms during commissioning phases, experiments like LSST could use generative models for survey observations to simulate new data sets. After training a classifier using simulated data, in production active learning could be used to automatically fill in gaps in classifier knowledge and augment predictive accuracy.

In this work, we used a generative model of SN Ia observations—overlaying fake SNe Ia onto real host galaxies—to produce the "Non-Artifact" component of our training data set. However, the nearly 500,000 artifacts in our training set were human-scanned, implying that future surveys will still need to do a great deal of scanning before being able to get an ML classifier off the ground. A new survey should not intentionally alter the pipeline to produce artifacts during commissioning, as it is crucial that the unseen data be drawn from the same feature distributions as the training data. For surveys with $\langle N_A/N_{NA}\rangle \gtrsim 100$, Brink et al. (2013) showed that a robust artifact library can be prepared by randomly sampling from all detections of variability produced by the difference imaging pipeline. For surveys or pipelines that do not produce as many artifacts, some initial scanning to produce a few 10^4-artifact library from commissioning data should be sufficient to produce an initial training set (Brink et al. 2013; du Buisson et al. 2015).

2.5.2 Eliminating Spurious Candidates

Using a two-night trigger, some spurious science candidates can be created due to nightly variations in astrometry, observing conditions, and repeatedly imaged source brightnesses that cause night-to-night fluctuations in the appearance of candidates on difference images. These variations lead to a spread of ML scores for a given candidate. As an observing season progress, artifacts can accumulate large numbers of detections via repeated visits. Although for a typical artifact the vast majority of detections fail the ML requirement, the fluctuations in ML scores can cause a small fraction of the detections to satisfy the `autoScan` requirement. Figure 2.9 shows an example of this effect.

Mitigating the buildup of spurious multi-night candidates could be achieved by implementing a second ML classification framework that takes as input multi-night information, including the detection-level output of `autoScan`, to predict whether a given science candidate represents a bona-fide astrophysical source. Training data compilation could be performed by randomly selecting time-contiguous strings of detections from known candidates. The lengths of the strings could be drawn from a distribution specified during framework development. Candidate-level features could characterize the temporal variation of detection level features, such as the highest and lowest night-to-night shifts in `autoScan` score, magnitude, and astrometric uncertainty.

Acknowledgments

DAG thanks an anonymous referee for comments that improved the paper. We are grateful for the extraordinary contributions of our CTIO colleagues and the DES Camera, Commissioning and Science Verification teams for achieving excellent instrument and telescope conditions that have made this work possible. The success of this project also relies critically on the expertise and dedication of the DES Data Management organization. Funding for DES projects has been provided by the U.S. Department of Energy, the U.S. National Science Foundation, the Ministry of Science and Education of Spain, the Science and Technology Facilities Council of the United Kingdom, the Higher Education Funding Council for England, the National Center for Supercomputing Applications at the University of Illinois at Urbana-Champaign, the Kavli Institute of Cosmological Physics at the University of Chicago, Financiadora de Estudos e Projetos, Fundação Carlos Chagas Filho de Amparo á Pesquisa do Estado do Rio de Janeiro, Conselho Nacional de Desenvolvimento Científico e Tecnológico and the Ministério da Ciência e Tecnologia, the Deutsche Forschungsgemeinschaft and the collaborating institutions in the Dark Energy Survey.

The collaborating institutions are Argonne National Laboratory, the University of California, Santa Cruz, the University of Cambridge, Centro de Investigaciones Energeticas, Medioambientales y Tecnologicas-Madrid, the University of Chicago, University College London, the DES-Brazil Consortium, the Eidgenössische Tecnische Hochschule (ETH) Zürich, Fermi National Accelerator Laboratory, the University of Edinburgh, the University of Illinois at Urbana-Champaign, the Institut de Ciencies de l'Espai (IEEC/CSIC), the Intitut de Fisica

d'Altes Energies, Lawrence Berkeley National Laboratory, the Ludwig-Maximilians Universität and the associated Excellence Cluster Universe, the University of Michigan, the National Optical Astronomy Observatory, the University of Nottingham, the Ohio State University, the University of Pennsylvania, the University of Portsmouth, SLAC National Acclerator Laboratory, Stanford University, the University of Sussex, and Texas A&M University.

This research used resources of the National Energy Research Scientific Computing Center, a DOE Office of Science User Facility supported by the Office of Science of the U.S. Department of Energy under Contract No. DE-AC02-05CH11231. Figure 2.4 was generated with a modified version of `triangle.py` (Foreman-Mackey et al. 2014). ACR acknowledges financial support provided by the PAPDRJ CAPES/FAPERJ Fellowship. FS acknowledges financial support provided by CAPES under contract No. 3171-13-2. The DES participants from Spanish institutions are partially supported by MINECO under grants AYA2012-39559, ESP2013-48274, FPA2013-47986, and Centro de Excelencia Severo Ochoa SEV-2012-0234, some of which include ERDF funds from the European Union.

Chapter 3

How to Find Gravitationally Lensed Type Ia Supernovae

An earlier version of this chapter was previously published as Goldstein, D. A., & Nugent, P. E. 2017, ApJ, 834, L5.

Abstract

Type Ia supernovae (SNe Ia) that are multiply imaged by gravitational lensing can extend the SN Ia Hubble diagram to very high redshifts ($z \gtrsim 2$), probe potential SN Ia evolution, and deliver high-precision constraints on H_0, w, and Ω_m via time delays. However, only one, iPTF16geu, has been found to date, and many more are needed to achieve these goals. To increase the multiply imaged SN Ia discovery rate, we present a simple algorithm for identifying gravitationally lensed SN Ia candidates in cadenced, wide-field optical imaging surveys. The technique is to look for supernovae that appear to be hosted by elliptical galaxies, but that have absolute magnitudes implied by the apparent hosts' photometric redshifts that are far brighter than the absolute magnitudes of normal SNe Ia (the brightest type of supernovae found in elliptical galaxies). Importantly, this purely photometric method does not require the ability to resolve the lensed images for discovery. AGN, the primary sources of contamination that affect the method, can be controlled using catalog cross-matches and color cuts. Highly magnified core-collapse SNe will also be discovered as a byproduct of the method. Using a Monte Carlo simulation, we forecast that LSST can discover up to 500 multiply imaged SNe Ia using this technique in a 10-year z-band search, more than an order of magnitude improvement over previous estimates (Oguri & Marshall 2010). We also predict that ZTF should find up to 10 multiply imaged SNe Ia using this technique in a 3-year R-band search—despite the fact that this survey will not resolve a single system.

3.1 Introduction

Constraining H_0, w, and Ω_m with lensing time delays is a key goal of modern precision cosmology (Treu 2010). Currently, high-quality time delay measurements have only been obtained for quasars and active galactic nucleii (AGN, e.g., Vuissoz et al. 2008; Suyu et al. 2013; Tewes et al. 2013; Bonvin et al. 2016). However, other kinds of variable sources are better suited for the job. Using time delays from lensed supernovae to measure H_0 was first proposed by Refsdal (1964), and it has since been realized that Type Ia supernovae (SNe Ia) have many advantages over AGN and quasars as time delay indicators. Because they are standardizable candles, strongly lensed SNe Ia can be used to directly determine the lensing magnification factor μ, which breaks the degeneracy between the lens potential and the Hubble constant (Oguri & Kawano 2003). Because they possess exceptionally well-characterized spectral sequences (e.g., Nugent et al. 2002; Pereira et al. 2013a), time delays are less onerous to extract from SNe Ia than from AGN and quasars, which show considerable variation in light curve morphology across events. Also, the well known spectral energy distributions (SED) of SNe Ia allow one to correct for extinction along the paths of each SN Ia image—a huge advantage over AGN and quasars.

Despite these advantages, several challenges face SNe Ia as tools for time delay measurements. First, multiply imaged SNe Ia are rarer than multiply imaged quasars and AGN. Whereas the number of robust time delays from quasars is now in the double digits, only one multiply imaged SN Ia—iPTF16geu (Goobar et al. 2017)—has ever been found. Before this serendipitous event, only a multiply imaged core-collapse SN (Kelly et al. 2015a,b) and a few lensed, but not multiply imaged, SNe Ia had been discovered (Amanullah et al. 2011; Patel et al. 2014; Rodney et al. 2015; Petrushevska et al. 2016). Another challenge is that most SNe Ia are visible for only ∼100 days after they explode, whereas AGN and quasars can be monitored for variability over much longer time scales. Because high-resolution imaging or spectroscopy while an SN Ia is still active is necessary to measure a time delay, this creates pressure to identify strongly lensed SNe Ia as soon after explosion as possible. Quimby et al. (2014) classified an event as a lensed SN Ia that was previously thought to be a new type of superluminous supernova (Chornock et al. 2013). However, the classification was performed well after the event had faded and thus neither the properties of the lens system nor H_0 could be constrained. Finally, most strong gravitational lenses produce images that are separated by less than the resolution of ground-based optical surveys (Oguri 2006). Images of iPTF16geu were detected just $0.3''$ away from the center of a $z = 0.21$ quiescent galaxy, yet the initial discovery was performed on an telescope with typical seeing of $2.5''$.

In this paper, we address these challenges by presenting a new technique for identifying gravitationally lensed SN Ia candidates. Our goal is to enable transient surveys to systematically search for multiply imaged SNe Ia in their data, and to make strongly lensed SNe Ia viable tools for precision cosmology. In Section 3.2, we present the technique and discuss its sources of contamination. In Section 3.3, we apply it to a Monte Carlo simulation of the source and lens populations to estimate the multiply imaged SN Ia yields of the Large Synoptic Survey Telescope (LSST; LSST Science Collaboration et al. 2009) and the Zwicky

Transient Facility (ZTF; Bellm 2014). We discuss the implications of our method in Section 5.5 and conclude in Section 5.6. Throughout this paper we assume a Planck Collaboration et al. (2016a) cosmology with $\Omega_\Lambda = 0.6925$, $\Omega_m = 0.3075$, and $h = 0.6774$.

3.2 The Method

We consider the strong gravitational lensing of SNe Ia by quiescent (E/S0) galaxies, which have three properties that are useful to identify strongly lensed SNe Ia. First, normal SNe Ia are the brightest type of supernovae that have ever been observed to occur in quiescent galaxies (Maoz et al. 2014). Second, the absolute magnitudes of normal SNe Ia in quiescent galaxies are remarkably homogenous, even without correcting for their colors or lightcurve shapes ($\sigma_M \sim 0.4$ mag), with a component of the population being underluminous (Li et al. 2011). Finally, due to the sharp 4000Å break in their spectra, quiescent galaxies tend to provide accurate photometric redshifts from large-scale multi-color galaxy surveys such as the Sloan Digital Sky Survey (SDSS; York et al. 2000).

A high-cadence, wide-field imaging survey can leverage these facts to systematically search for strongly lensed SNe Ia in the following way. First, by spatially cross-matching its list of supernova candidates with a catalog of quiescent galaxies for which secure photometric redshifts have been obtained, supernovae that appear to be hosted by quiescent galaxies can be identified. Empirically, it is likely that these supernovae are Type Ia. Not all galaxies with secure photometric redshifts are quiescent; some can show signs of ongoing star formation, in which case they may host core-collapse supernovae that can contaminate the sample. For this reason we follow Tojeiro et al. (2013) and select quiescent galaxies by requiring that in addition to secure photometric redshifts (i.e., $\sigma_z/(1+z) \lesssim 0.05$), they have a rest-frame $g-r$ color > 0.65, to ensure that they are "red and dead."

Assuming a standard ΛCDM cosmology, distance moduli to the supernovae can be computed using the photometric redshifts, giving the absolute magnitudes. Because SNe Ia hosted in quiescent galaxies are expected to be normal to underluminous, their absolute magnitudes should be no brighter than -19.5 in B (see Figure 3.1). If a supernova candidate hosted in an elliptical galaxy has an absolute magnitude that is brighter than this, there is a strong chance that it is not actually in that galaxy, but is instead a background supernova lensed by the apparent host. Therefore, conservatively requiring:

$$M_B = m_X - \mu_D(z_{ph}) - K_{BX}(z_{ph}) < -20, \tag{3.1}$$

will produce a catalog of lensed SN Ia candidates, where m_X is the peak apparent magnitude of the supernova in filter X, $\mu_D(z_{ph})$ is the ΛCDM distance modulus evaluated at the photometric redshift of the apparent host galaxy, K_{BX} is the cross-filter K-correction from the rest-frame B-band to the observer frame X-band (Kim et al. 1996), and M_B is the inferred rest-frame B-band absolute magnitude of the supernova. This is simply a statement that any supernova found to be brighter than an SN Ia at the photometrically determined distance to

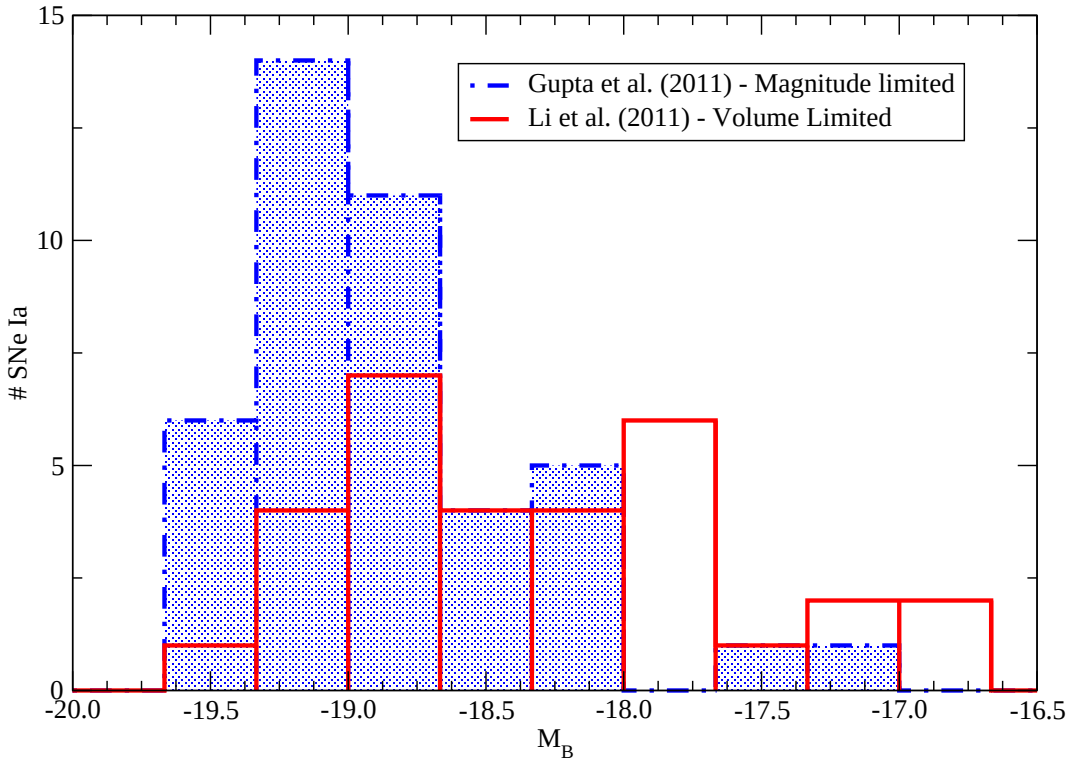

Figure 3.1: The luminosity function of SNe Ia in elliptical galaxies from the SDSS (Gupta et al. 2011) and LOSS (Li et al. 2011) supernova surveys. The former is magnitude-limited while the latter is volume-limited and thus more relevant to a survey of known host galaxies such as the one we propose here. As SNe Ia are the brightest supernovae hosted by ellipticals, a conservative cut at $M_B < -20$ will eliminate any contamination by supernovae located in a candidate lens galaxy.

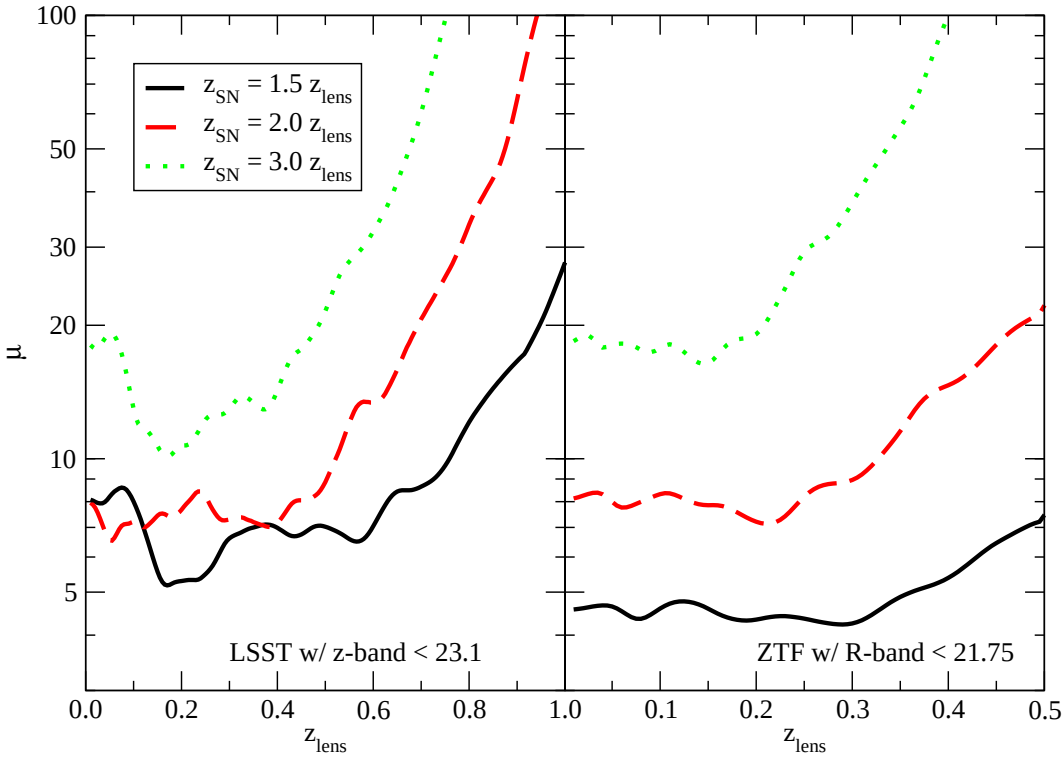

Figure 3.2: The magnification required for our search technique to be sensitive to strongly lensed SNe Ia in a z-band LSST search and an R-band ZTF search. Magnification is required at low redshifts to ensure $M_B < -20$ (Equation 3.1), and at higher redshifts to ensure at least 5-σ detections. The non-monotonicity of the curves is due to the cross-filter K-corrections, as is the slightly higher magnification required in the z-band search at low-redshift compared to R-band.

its potential quiescent host could be a lensed SN Ia. The magnification μ necessary for this method to be sensitive to various lensing systems is shown in Figure 3.2.

Applying this technique to a cross-match of Palomar Transient Factory (PTF) transients and SDSS galaxies satisfying the above criteria would have led to the discovery of iPTF16geu, as it appeared several magnitudes too bright to be associated with its apparent host, a $z_{ph} = 0.23$ lens galaxy. Although PTF has over a billion detections of variability in its transient database, performing the above cuts led to a catalog of only a few hundred transients. These are easy to vet by eye and will be the subject of a future paper.

An important property of this search technique is that it does not require the ability to resolve the lensed images to perform discovery. Once lensed SN Ia candidates are identified, they can be confirmed using high-resolution imaging, e.g., Laser Guide Star Adaptive Optics (LGSAO) or space-based imaging such as HST or, in the future, by the James Webb Space Telescope (JWST) and the Wide Field Infrared Space Telescope (WFIRST). If a retroactive search is being performed, then high-resolution imaging will yield lensed images of the supernova host galaxy, which provides strong indirect evidence for the lensed transient. Finally, if the supernova is still active, then a spectrum can confirm its redshift, and reveal features of the host and lens galaxies.

3.2.1 Sources of Contamination

AGN are the greatest source of contamination for this technique. AGN lightcurves can occasionally resemble those of supernovae, and they can have $M_B < -20$, so spectroscopic followup may be necessary to distinguish between the two. To reduce AGN contamination, one can cross-match lens candidates against e.g., the Brescia et al. (2015) SDSS AGN catalog. Additionally, the photometric redshifts of the lens galaxies may be polluted by emission from the source galaxies. To understand this potential bias, we examined the difference between the photometrically and spectroscopically determined redshifts of the galaxy-galaxy lens systems in the Master Lens Database[1] (Moustakas et al. in preparation) for which the restframe photometrically determined $g - r < 0.65$. The majority of these systems are from the SLACS (Bolton et al. 2008) and BELLS (Brownstein et al. 2012) surveys found via the method presented in Bolton et al. (2004), in which background emission lines at higher redshift are seen on lower redshift lensing galaxies. The results are presented in Figure 3.3. The overall bias is just 0.5-σ towards lower redshift, which is not surprising as bluer light from high-redshift emission line galaxies contaminates the rest-frame UV of the lower-redshift quiescent lens galaxies. This small bias effectively increases the magnification requirement by 20%, as we have underestimated the distance to the putative lensing galaxy. This is a conservative overestimate of the bias, as these systems required the presence of strong emission lines in order to be found.

Finally, highly magnified core-collapse supernovae may also contaminate the sources found by this method. Given that they have $M_B \sim -17$, the rates of these events are expected to

[1] http://slacs.astro.utah.edu

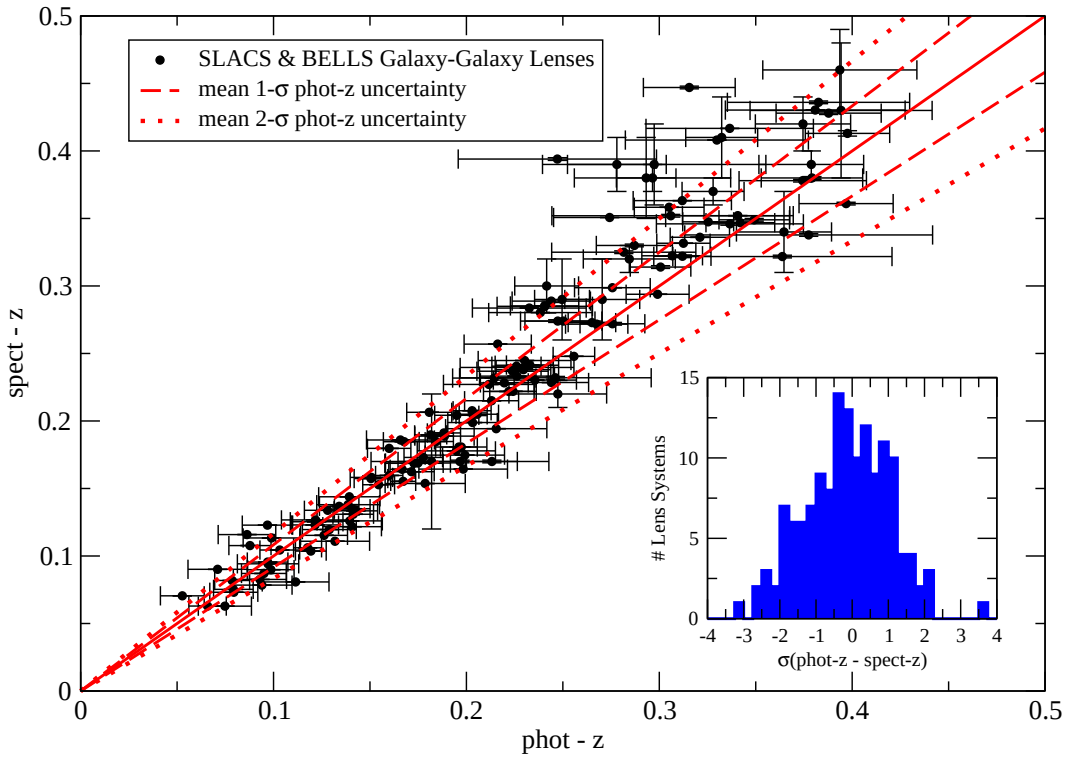

Figure 3.3: Spectroscopic redshift versus photometric redshift for SLACS and BELLS galaxy-galaxy lenses with $g - r > 0.65$ (Bolton et al. 2008; Brownstein et al. 2012). Strong source emission introduces negligible bias into the photometric redshifts of lens galaxies.

be much lower than lensed SNe Ia, as their discovery requires roughly an order of magnitude more magnification than SNe Ia.

3.3 Yields for Planned Surveys

Oguri & Marshall (2010) carried out detailed Monte Carlo simulations of the gravitationally lensed supernova and quasar yields of several cadenced optical imaging surveys, including LSST. They predicted that LSST should find roughly 45 multiply imaged SNe Ia over 10 years, but they assumed that only resolved systems (image separation $> 0.5''$ for LSST) with a flux ratio > 0.1 could be discovered. In this section, we carry out analogous rate forecasts using the candidate identification technique presented in Section 3.2, which does not possess these constraints. We develop a statistical model of the source and lens populations and then perform a Monte Carlo simulation to calculate the yields for LSST and ZTF.

3.3.1 Lens Modeling

We model the mass distribution of the lens galaxies as a Singular Isothermal Ellipsoid (SIE; Kormann et al. 1994), which has shown excellent agreement with observations (e.g., Koopmans et al. 2009; More et al. 2017). The SIE convergence κ is given by:

$$\kappa(x, y) = \frac{\theta_E}{2} \frac{\lambda(e)}{\sqrt{(1-e)^{-1}x^2 + (1-e)y^2}}, \tag{3.2}$$

where

$$\theta_E = 4\pi \left(\frac{\sigma}{c}\right)^2 \frac{D_{ls}}{D_s}. \tag{3.3}$$

In the above equations, σ is the velocity dispersion of the lens galaxy, e is its ellipticity, and $\lambda(e)$ is its so-called "dynamical normalization," a parameter related to three-dimensional shape. Here we make the simplifying assumption that there are an equal number of oblate and prolate galaxies, which Chae (2003) showed implies $\lambda(e) \simeq 1$. As in Oguri et al. (2008), we assume e follows a truncated normal distribution on the interval $[0.0, 0.9]$, with $\mu_e = 0.3$, $\sigma_e = 0.16$. Finally, the orientation θ_e of the lens galaxy is assumed to be random.

We also include external shear to account for the effect of the lens environment (e.g., Kochanek 1991; Keeton et al. 1997; Witt & Mao 1997) The potential V of the external shear is given by

$$V(x, y) = \frac{\gamma}{2}(x^2 - y^2)\cos 2\theta_\gamma + \gamma xy \sin 2\theta_\gamma, \tag{3.4}$$

where γ is the magnitude of the shear, and θ_γ describes its orientation in the image plane. We assume $\log_{10}\gamma$ follows a normal distribution with mean -1.30 and scale 0.2, consistent with the level of external shear expected from ray tracing in N-body simulations (Holder & Schechter 2003). The orientation of the external shear is assumed to be random.

We model the velocity distribution of elliptical galaxies as a modified Schechter function (Sheth et al. 2003):

$$dn = \phi(\sigma)d\sigma = \phi_* \left(\frac{\sigma}{\sigma_*}\right)^\alpha \exp\left[-\left(\frac{\sigma}{\sigma_*}\right)^\beta\right] \frac{\beta}{\Gamma(\alpha/\beta)}\frac{d\sigma}{\sigma}, \tag{3.5}$$

where Γ is the gamma function, and dn is the differential number of galaxies per unit velocity dispersion per unit comoving volume. We use the parameter values from SDSS (Choi et al. 2007): $(\phi_*, \sigma_*, \alpha, \beta) = (8 \times 10^{-3}\ h^3\ \mathrm{Mpc}, 161\ \mathrm{km\ s^{-1}}, 2.32, 2.67)$. We assume the mass distribution and velocity function do not evolve with redshift.

To convert Equation 4.3 into a redshift distribution, we use the definition of the comoving volume element:

$$dV_C = D_H \frac{(1+z)^2 D_A^2}{E(z)}\, dz\, d\Omega, \tag{3.6}$$

where $D_H = c/H_0$ is the Hubble distance, $E(z) = \sqrt{\Omega_M(1+z)^3 + \Omega_\Lambda}$ in our assumed cosmology, and D_A is the angular diameter distance. Since $dn = dN/dV_C$, for the all-sky ($d\Omega = 4\pi$) galaxy distribution we have

$$\frac{dN}{d\sigma dz} = 4\pi D_H \frac{(1+z)^2 D_A^2}{E(z)}\phi(\sigma). \tag{3.7}$$

Integrating Equation 4.5 over $0 \leq z \leq 1$ and $10^{1.7} \leq \sigma \leq 10^{2.6}$, the parameter ranges that we consider in this analysis, we find that there are $N_{\mathrm{gal}} \simeq 3.8 \times 10^8$ quiescent galaxies, all sky, that can act as strong lenses. Normalizing Equation 4.5 by this factor, we obtain the joint probability density function for σ and z:

$$p(\sigma, z) = \frac{4\pi D_H}{N_{\mathrm{gal}}} \frac{(1+z)^2 D_A^2}{E(z)}\phi(\sigma). \tag{3.8}$$

3.3.2 SN Ia Modeling

SNe Ia exhibit a redshift-dependent volumetric rate and an intrinsic dispersion in rest-frame M_B. In our model of the SN Ia population, we take the redshift-dependent SN Ia rate from Sullivan et al. (2000). We assume that the peak rest-frame M_B is normally distributed with $\mu_M = -19.3$ and $\sigma_M = 0.2$. To realize SN Ia lightcurves, we employ the implementation of the one-component SN Ia spectral template of Nugent et al. (2002) provided by Barbary et al. (2016), which automatically allows one to compute the cross-filter K-corrections in Equation 3.1. For simplicity, we assume that the SNe Ia suffer no extinction.

3.3.3 Monte Carlo Simulation

We carried out a Monte Carlo simulation of the lens and source populations to forecast the yields of multiply imaged SNe Ia for LSST and ZTF. To perform the simulation, we

generated 10^5 galaxies with parameters realized at random from their underlying distributions. Assuming the galaxies were uniformly distributed on the sky, the average area on the sky "occupied" by a single galaxy was $A_{\rm gal} = 4\pi/N_{\rm gal} \simeq 1.4 \times 10^3$ arcsec^2.

For each lens galaxy, an effective lensing area of influence was estimated as a $[8\theta_{E,max}]^2$ box centered on the galaxy, where $\theta_{E,max}$ is given by Equation 4.2 with $D_{ls}/D_s = 1$. This box size was chosen to be large enough to accommodate the effects of ellipticity and external shear. One year's worth of SNe Ia was realized at random locations in this box for each galaxy, at a rate amplified at all redshifts by a factor of 5×10^4 to reduce shot noise. SNe Ia with $z_{SN} < z_l$ were rejected. For each remaining source, we solved the lens equation using `glafic` (Oguri 2010) to determine the magnification and image multiplicity.

Given the redshift of each lens galaxy, the peak M_B implied by the redshift of the lens ("apparent host") was calculated for each multiply imaged system according to Equation 3.1, taking μ to be the total magnification of the images. Multiply imaged SNe Ia satisfying $M_B < -20$ and $m_X < m_{lim,X}$, where $m_{lim,X}$ is the 5σ limiting magnitude of the survey in filter X, were counted as "detections."

Given a nominal 20,000 $\square^\circ$ search in LSST to $z = 23.1$ ($i = 24.0$) we would find 500 (281) multiply lensed SNe Ia via this method over a 10 year period (the drop in rest-frame SN Ia flux below 4000Å makes z-band more efficient than i-band at high-redshift). A 3 year, 10,000 deg^2 ZTF survey to $R = 21.7$ (obtained through weekly image co-addition) would yield 10 such SNe Ia. Assuming the magnification is due solely to the brightest image gives a conservative lower limit on yields: 220 SNe Ia for LSST-z and 3 for ZTF-R. Figure 4.9 shows the redshift distribution of multiply imaged SNe Ia that can be discovered in the total magnification case and Figure 3.5 shows the joint time delay-image separation distribution.

3.4 Discussion

As this technique will increase the detection of lensed SNe Ia in LSST by an order of magnitude and yield a few discoveries per year in ZTF, we now discuss potential improvements to this method as well as follow-up plans for these future discoveries. The most immediate improvement to this method is that one can not only use the incongruous brightness of a supernova to identify it as a potential lens candidate, but also its photometric evolution. Notwithstanding that a multiply imaged supernova will appear photometrically as the superposition of a few time-shifted lightcurves, both the shape of lensed SN Ia lightcurves and their colors will reflect their origin in a supernova that is both incompatible with its apparent host galaxy and is at higher redshift. Thus one should be able to relax the constraint in Equation 3.1 and use all the information in the transient's lightcurve to identify a lensed supernova candidate. Furthermore, one could relax the requirement that one examine only quiescent galaxies and take a statistical approach involving the probability of the candidate being a superluminous supernova at the redshift of the host or a lensed supernova behind it. Given the rarity of such events, the contamination will likely be small and could easily be screened via rapid follow-up spectroscopy on 8-m class telescopes. Lensed core-collapse

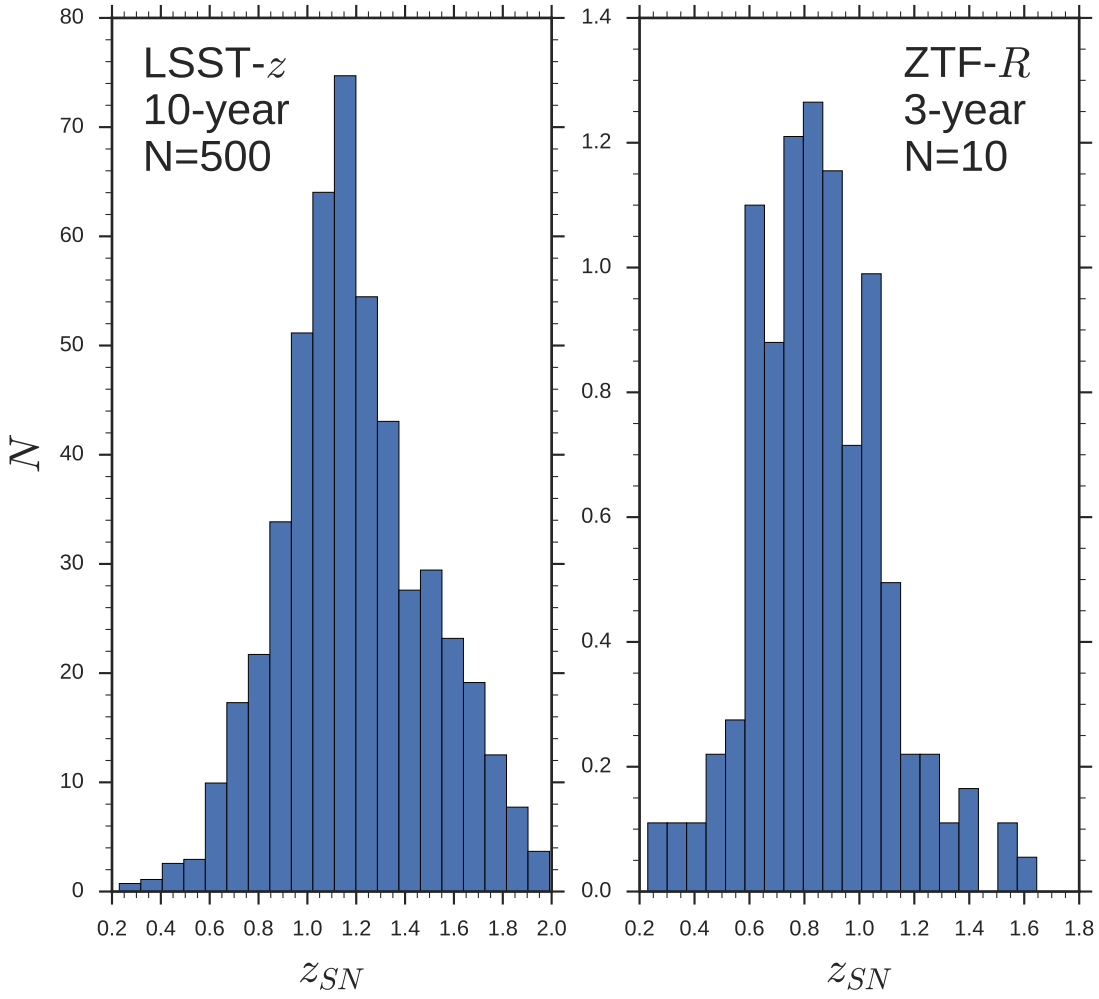

Figure 3.4: Redshift distribution of multiply imaged SNe Ia detectable by our method in a 10-year LSST z-band search (left) and a 3-year ZTF R-band search (right).

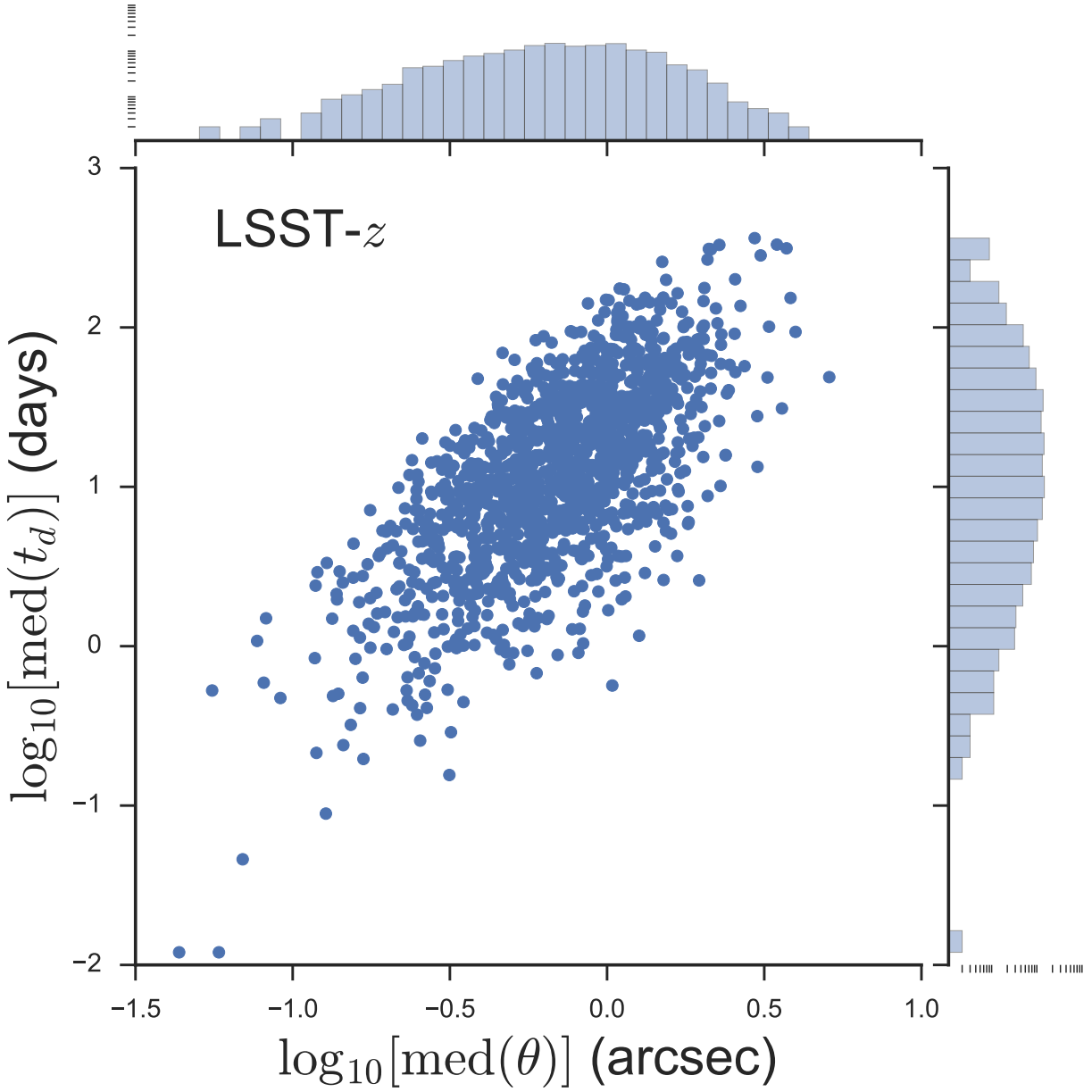

Figure 3.5: Distribution of median time delays and median image separations for the LSST z-band sample.

supernovae could be discovered via similar techniques.

Turning our attention to follow-up, a major difference between the work presented here and that of Oguri & Marshall (2010) is that the vast majority of the SNe Ia discovered via this method will have unresolved supernova images or low flux ratios. While the survey itself will provide an absolute measurement of the total magnification, follow-up resources with higher resolution and/or depth will be required to measure the relative magnification of each of the lensed supernova images. Space based facilities such as HST, JWST and WFIRST (Gehrels et al. 2015), given its proposed low-resolution IFU spectrograph (Perlmutter 2014), are ideally set up to make these measurements from the optical through near-IR. However, even ground-based LGSAO would be well suited for these measurements in the near-IR.

Finally, Dobler & Keeton (2006a) showed that microlensing may affect many of these systems. The SN Ia yields should remain invariant under microlensing, as the microlensing magnification distributions are roughly symmetric and centered around zero. Since microlensing is achromatic, the color curves of SNe Ia will be unaffected and one can use the multiple inflections in these curves to carry out time delay measurements.

3.5 Conclusion

In this paper, we have presented a simple, new method for discovering strongly gravitationally lensed SNe Ia in high-cadence, wide-field imaging surveys. We have calculated the nominal multiply-imaged SN Ia discovery rates for LSST and ZTF, and found them to be roughly an order of magnitude higher than previous estimates. Due to its effectiveness and ease of implementation, this technique will greatly increase the utility of gravitationally lensed SNe Ia as cosmological probes. As such, a renewed focus should be placed on their role in cosmological studies and how to maximize their scientific return.

Acknowledgements

PEN thanks the Berkeley Astronomy Department for asking him to give a last-minute Departmental Lunch Talk on iPTF16geu, where he first proposed the main idea behind this paper. The authors thank Ariel Goobar, Joshua Bloom, Jessica Lu, and Peter Behroozi for useful discussions, and they acknowledge support from the DOE under grant DE-AC02-05CH11231, Analytical Modeling for Extreme-Scale Computing Environments. This research used resources of the National Energy Research Scientific Computing Center, a DOE Office of Science User Facility supported by the Office of Science of the U.S. Department of Energy under Contract No. DE-AC02-05CH11231.

Chapter 4

Precise Time Delays from Strongly Gravitationally Lensed Type Ia Supernovae with Chromatically Microlensed Images

An earlier version of this chapter was previously published as Goldstein, D. A., Nugent, P. E., Kasen, D. N., & Collett, T. E. 2018, ApJ, 855, 22.

Abstract

Time delays between the multiple images of strongly lensed Type Ia supernovae (glSNe Ia) have the potential to deliver precise cosmological constraints, but the effects of microlensing on the measurement have not been studied in detail. Here we quantify the effect of microlensing on the glSN Ia yield of the Large Synoptic Survey Telescope (LSST) and the effect of microlensing on the precision and accuracy of time delays that can be extracted from LSST glSNe Ia. Microlensing has a negligible effect on the LSST glSN Ia yield, but it can be increased by a factor of $\sim$2 to 930 systems using a novel photometric identification technique based on spectral template fitting. Crucially, the microlensing of glSNe Ia is achromatic until 3 rest-frame weeks after the explosion, making the early-time color curves microlensing-insensitive time delay indicators. By fitting simulated flux and color observations of microlensed glSNe Ia with their underlying, unlensed spectral templates, we forecast the distribution of absolute time delay error due to microlensing for LSST, which is unbiased at the sub-percent level and peaked at 1% for color curve observations in the achromatic phase, while for light curve observations it is comparable to state-of-the-art mass modeling uncertainties (4%). About 70% of LSST glSN Ia images should be discovered during the achromatic phase, indicating that microlensing time delay uncertainties can be minimized if prompt multicolor follow-up observations are obtained. Accounting for microlensing, the 1–2 day time delay on the recently

discovered glSN Ia iPTF16geu can be measured to 40% precision, limiting its cosmological utility.

4.1 Introduction

Since the discovery of cosmic acceleration (Riess et al. 1998; Perlmutter et al. 1999), ΛCDM has become the observationally favored cosmology, implying that the universe is spatially flat, that it contains cold dark matter and baryons, and that its accelerated expansion is driven by a cosmological constant. Recently, a deviation from ΛCDM was reported by Riess et al. (2016), whose measurement of the Hubble constant H_0 using the cosmic distance ladder is in 3.4σ tension with the value inferred from the cosmic microwave background (CMB; Planck Collaboration et al. 2016a), assuming a ΛCDM cosmology and the standard model of particle physics. Independent measurements of H_0 with percent-level accuracy are necessary to determine whether the discrepancy is due to new physics (e.g., a new neutrino species; Riess et al. 2016; Bonvin et al. 2017) or to systematics.

Strong gravitational lensing is an independent probe of the cosmological parameters (Oguri et al. 2012; Suyu et al. 2013; Collett & Auger 2014). Time delays between multiple images of strongly gravitationally lensed variable sources are particularly sensitive to H_0, making them ideal tools to test this discrepancy. They also are sensitive to other parameters of the cosmological model, such as the dark energy equation of state and its evolution with redshift (Linder 2004, 2011; Treu & Marshall 2016).

Measuring cosmological parameters to percent level accuracy with strong lens time delays requires three main ingredients (Suyu et al. 2017). First, one must measure the time delays (e.g. Tewes et al. 2013; Bonvin et al. 2017). Second, the lensing potential must be inferred to convert the observed time delays into measurements of the time delay distance (e.g., Wong et al. 2017). This relies on reconstruction of the extended features of a lensed host. Finally, the effect of weak lensing by mass close to the lens and along the line of sight must be included (e.g., Suyu et al. 2010; Collett et al. 2013; Rusu et al. 2017; McCully et al. 2017), since lenses are typically found in overdense regions of the universe (Fassnacht et al. 2011).

To date, time delay cosmography has only been attempted with strongly lensed active galactic nuclei (AGNs; e.g., Vuissoz et al. 2008; Suyu et al. 2013; Tewes et al. 2013; Bonvin et al. 2016). Lensed AGNs complicate these ingredients, making percent-level constraints on H_0 difficult. Because the light curves of AGNs are stochastic and heterogeneous, they typically require years of cadenced monitoring to yield precise time delays (Liao et al. 2015). Inferring the lensing potential by reconstructing the lensed host light is challenging since AGNs typically outshine their host galaxies by several magnitudes. Detecting lensed AGNs requires observations of multiple images introducing a selection function for larger Einstein radii and hence an overdense line of sight (Collett & Cunnington 2016), leading to systematic overestimates of H_0.

In contrast, the light curves of Type Ia supernovae (SNe Ia) are remarkably homogeneous, and strongly lensed SN Ia (glSN Ia) light curves evolve over weeks, not years, allowing their

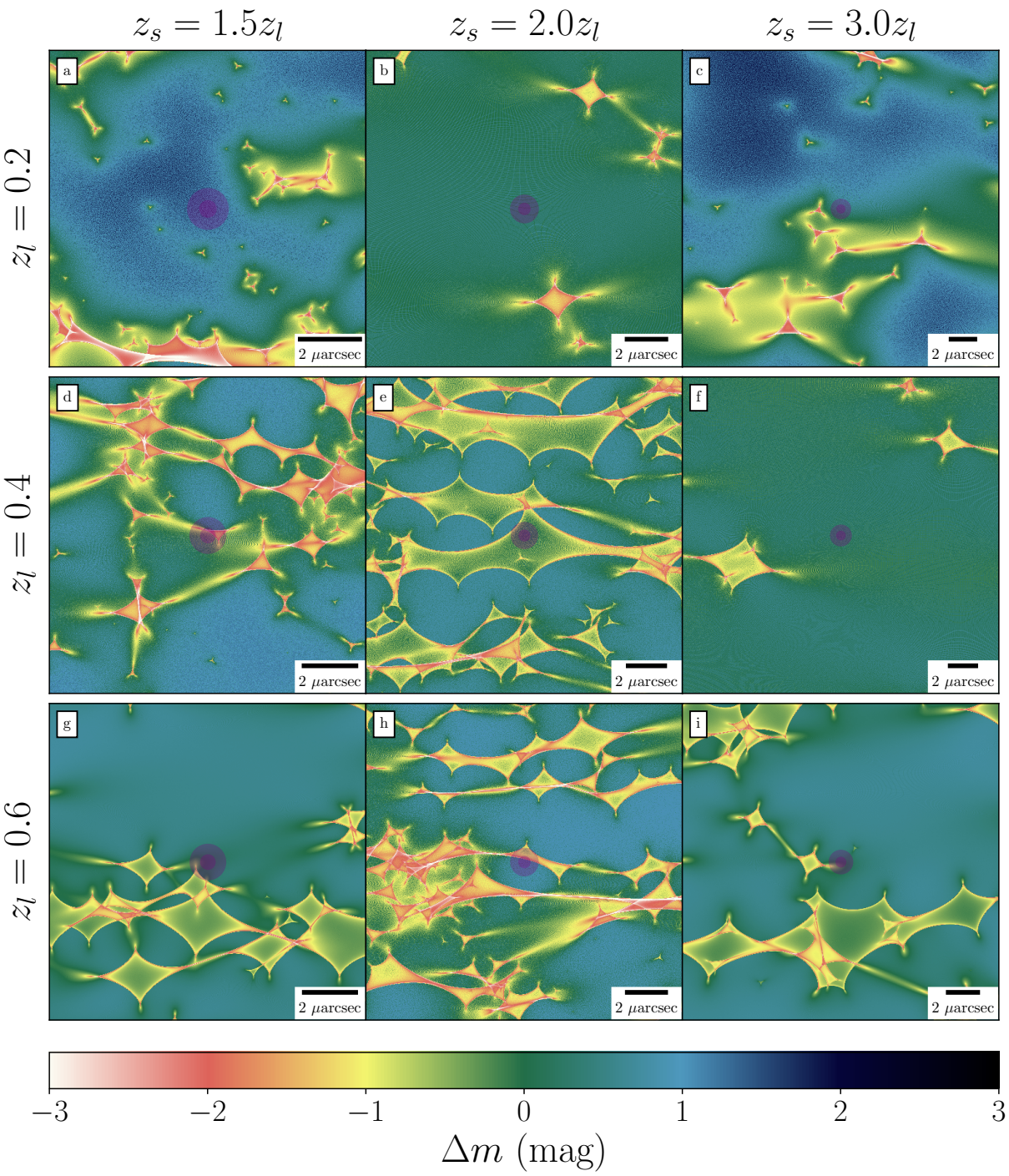

Figure 4.1: Source-plane magnification patterns of nine of 78,184 the lens galaxy star fields considered in this analysis. Each panel consists of $1{,}000^2$ pixels and has a side length of 10 times the Einstein radius of a $1M_\odot$ deflector projected onto the source plane. The detailed parameters of each map are given in Table 4.1. The size of the exterior shell (4×10^4 km s^{-1}) of the SN Ia model W7 at 20 (50) days after explosion is plotted as the interior (exterior) purple circle at the center of each map. Negative (positive) Δm indicates magnification (demagnification) over the value from a smooth mass model without microlensing.

time delays to be measured with far less observational overhead than those of AGNs. In addition, glSNe Ia fade away, allowing a simpler reconstruction of the lensed hosts. glSNe Ia can be detected without resolving multiple images (Goobar et al. 2017), simplifying the selection function. Because glSNe Ia are standardizable candles, they also have the potential to directly determine the lensing magnification factor μ, which breaks the degeneracy between the lens potential and the Hubble constant (Oguri & Kawano 2003), if the microlensing and macrolensing magnifications can be separated. The well known spectral energy distributions (SEDs) of SNe Ia also allow one to correct for extinction along the paths of each SN Ia image—another major advantage over AGNs.

So far, only one glSN Ia, iPTF16geu, has been discovered with resolved images (Goobar et al. 2017). However, future surveys, especially the Large Synoptic Survey Telescope (LSST; LSST Science Collaboration et al. 2009), are expected to discover hundreds (Goldstein & Nugent 2017). Thus the prospects for discovering a sufficient number of glSNe Ia to perform time-delay cosmography in the near future are good.

However, there is a foreground that threatens this outlook: microlensing. It has long been known that lens galaxy field stars can significantly magnify and demagnify cosmologically distant background AGNs (Chang & Refsdal 1979) and supernovae (Dobler & Keeton 2006b; Bagherpour et al. 2006). In the microlensing scenario, different macroimages of the same source propagate through different regions of the lens galaxy, passing through distinct lens galaxy star fields. The star fields possess rich networks of caustics that introduce magnification patterns into the source plane. These patterns vary over characteristic angular scales of microarcseconds (hence "microlensing," see Figure 4.1), which are typically comparable to the physical sizes of supernovae and AGNs. Thus, as a strongly lensed supernova expands over the source plane, it can experience time- and wavelength-dependent magnifications unique to each lensed image, distorting their light curves and spectra in different ways. These distortions can make it harder to "match up" the light curves of multiple images and extract an accurate time delay.[1]

Microlensing of lensed variable sources is more than a theoretical exercise: it has been reported in many strongly lensed quasars (e.g., Kayser et al. 1986), and there is also evidence that it affects the images of iPTF16geu (More et al. 2017). Dobler & Keeton (2006b) estimated that microlensing can introduce uncertainties of several days into the features of supernova light curves that can yield time delays. Typical time delays for glSNe Ia are a couple of weeks (Goldstein & Nugent 2017), translating to a typical fractional time delay uncertainty of (a few days) / (two weeks) $\sim 20\%$. At this precision, $\sim$400 glSN Ia time delays would be required to reach a 1% uncertainty on H_0, assuming no other sources of error, whereas a single glSN Ia time delay with 1% precision could accomplish the same goal. Thus, controlling microlensing is of critical importance to the success of time delay cosmography with glSNe Ia.

If, as proposed by Goldstein & Nugent (2017), the microlensing magnification affects all wavelengths equally (i.e., if it is "achromatic")—then one could use the color curves of glSNe Ia

[1]N.B. The general relativistic time delays introduced by microlensing into macroimages are of order microseconds (Moore & Hewitt 1996)—too small to detect. The uncertainty microlensing introduces into time delays is solely due to time- and wavelength-dependent distortions of macroimage light curves and spectra.

Table 4.1: Properties of the magnification patterns in Figure 4.1.

	κ	f_*	γ	q	$\langle\mu\rangle$
a	1.30	0.84	1.30	0.20	0.63
b	0.24	0.35	0.25	0.10	1.93
c	1.25	0.83	1.26	0.20	0.65
d	0.87	0.72	0.93	1.00	1.19
e	0.75	0.80	0.76	1.00	1.96
f	0.30	0.38	0.27	1.00	2.39
g	0.36	0.49	0.33	1.00	3.30
h	0.84	0.72	0.79	0.10	1.66
i	0.37	0.50	0.31	1.00	3.29

Note. — κ: local convergence. f_*: fraction of surface density in stars. γ: local shear. q: mass ratio m_{min}/m_{max} of the stellar mass function. $\langle\mu\rangle$: magnification of the field from a smooth mass model without microlensing.

instead of the broadband light curves to extract time delays even if the images are affected by microlensing. For example, for a given image, if the B-band is macro- and microlensed as much as the U-band, then in the $U - B$ color curve, the micro- and macrolensing magnifications will both cancel out, leaving features common to the color curves of all images that can pin down the time delays to high precision. This would enable color curves of different images to be compared meaningfully, yielding time delays with less uncertainty.

In this article, we use detailed radiation transport simulations of a well-understood SN Ia model to assess the viability of extracting time delays from the color curves of glSNe Ia to circumvent the effects of microlensing. We also perform the first glSN Ia yield calculation that takes microlensing into account. The structure of the paper is as follows. In Section 4.2, we describe the radiation transport, glSN Ia population, and microlensing models used to synthesize representative microlensed glSN Ia SEDs. In Section 4.3, we present the results of our simulations and use them to show that the microlensing of glSNe Ia exhibits an achromatic phase at early times. In Section 4.4, we present a novel spectral template-based glSN Ia photometric detection technique and use it to forecast the glSN Ia yield of LSST. In Section 4.5, we forecast the time delay uncertainty due to microlensing and show that it can be controlled to 1% for typical LSST systems. We conclude in Section 5.6. Throughout this paper we assume a Planck Collaboration et al. (2016a) cosmology with $\Omega_\Lambda = 0.6925$, $\Omega_m = 0.3075$, and $h = 0.6774$.

4.2 Population, Radiation Transport, and Microlensing Simulations

In this section, we describe the simulation framework we use to generate a realistic population of glSNe Ia. First, the framework realizes a population of unlensed SNe Ia and elliptical galaxy lenses using measured redshift distributions. It solves the lens equation for supernovae and lenses close together on the sky, and when a multiply imaged system is produced, it yields image multiplicities, time delays, magnifications, and image positions. For each lensed supernova image, the framework generates a microlensing magnification pattern based on the image properties. A theoretical SN Ia spectral time series is convolved with the magnification pattern, giving the lensing amplification of the supernova SED as a function of time and wavelength. This in turn is applied to an empirical SN Ia SED template. Realistic LSST light curves are generated from these microlensed spectral templates and fed to a novel detection algorithm.

4.2.1 The Strongly Lensed Type Ia Supernova Population

In the present analysis we use the same glSN Ia population model as Goldstein & Nugent (2017). We consider only elliptical galaxy lenses and model their mass distribution as a Singular Isothermal Ellipsoid (SIE; Kormann et al. 1994), which has shown excellent agreement

with observations (e.g., Koopmans et al. 2009). The SIE convergence κ is given by:

$$\kappa(x,y) = \frac{\theta_E}{2}\frac{\lambda(e)}{\sqrt{(1-e)^{-1}x^2 + (1-e)y^2}}, \tag{4.1}$$

where

$$\theta_E = 4\pi\left(\frac{\sigma}{c}\right)^2 \frac{D_{ls}}{D_s}. \tag{4.2}$$

In the above equations, σ is the velocity dispersion of the lens galaxy, e is its ellipticity, and $\lambda(e)$ is its so-called "dynamical normalization," a parameter related to three-dimensional shape. Here we make the simplifying assumption that there are an equal number of oblate and prolate galaxies, which Chae (2003) showed implies $\lambda(e) \simeq 1$. As in Oguri et al. (2008), we assume e follows a truncated normal distribution on the interval $[0.0, 0.9]$, with $\mu_e = 0.3$, $\sigma_e = 0.16$.

We also include external shear to account for the effect of the lens environment (e.g., Kochanek 1991; Keeton et al. 1997; Witt & Mao 1997) We assume $\log_{10}\gamma_{\rm ext}$ follows a normal distribution with mean -1.30 and scale 0.2, consistent with the level of external shear expected from ray tracing in N-body simulations (Holder & Schechter 2003). The orientation of the external shear is assumed to be random.

We model the velocity distribution of elliptical galaxies as a modified Schechter function (Sheth et al. 2003):

$$dn = \phi(\sigma)d\sigma = \phi_*\left(\frac{\sigma}{\sigma_*}\right)^\alpha \exp\left[-\left(\frac{\sigma}{\sigma_*}\right)^\beta\right]\frac{\beta}{\Gamma(\alpha/\beta)}\frac{d\sigma}{\sigma}, \tag{4.3}$$

where Γ is the gamma function, and dn is the differential number of galaxies per unit velocity dispersion per unit comoving volume. We use the parameter values of Choi et al. (2007) from the Sloan Digital Sky Survey (SDSS; Frieman et al. 2008): $(\phi_*, \sigma_*, \alpha, \beta) = (8\times10^{-3}\ h^3\ \mathrm{Mpc}, 161\ \mathrm{km\ s^{-1}}, 2.32, 2.67)$. We assume the mass distribution and velocity function do not evolve with redshift, consistent with the results of Chae (2007), Oguri et al. (2008), and Bezanson et al. (2011).

To convert Equation 4.3 into a redshift distribution, we use the definition of the comoving volume element:

$$dV_C = D_H\frac{(1+z)^2 D_A^2}{E(z)}\,dz d\Omega, \tag{4.4}$$

where $D_H = c/H_0$ is the Hubble distance, $E(z) = \sqrt{\Omega_M(1+z)^3 + \Omega_\Lambda}$ in our assumed cosmology, and D_A is the angular diameter distance. Since $dn = dN/dV_C$, for the unnormalized all-sky ($d\Omega = 4\pi$) galaxy distribution we have

$$\frac{dN}{d\sigma dz} = 4\pi D_H\frac{(1+z)^2 D_A^2}{E(z)}\phi(\sigma). \tag{4.5}$$

Integrating Equation 4.3 over $0 \leq z \leq 1$ and $10^{1.7}$ km s$^{-1} \leq \sigma \leq 10^{2.6}$ km s^{-1}, we find that there are $N_{\rm gal} \simeq 3.8 \times 10^8$ elliptical galaxies, all sky, that can act as strong lenses. This gives the joint probability density function for σ and z:

$$p(\sigma, z) = \frac{1}{N_{\rm gal}} \frac{dN}{d\sigma dz}. \tag{4.6}$$

SNe Ia exhibit a redshift-dependent volumetric rate and an intrinsic dispersion in rest-frame M_B. In our model of the SN Ia population, we take the redshift-dependent SN Ia rate from Sullivan et al. (2000). We assume that the peak rest-frame M_B is normally distributed with $\mu_M = -19.3$ and $\sigma_M = 0.2$. For simplicity, we neglect extinction.

The lens and source populations are realized in a Monte Carlo simulation. We generate 10^5 lens galaxies with parameters drawn at random from their underlying distributions. For each lens galaxy, an effective lensing area of influence is estimated as a $[8\theta_{E,z_s=\infty}]^2$ box centered on the galaxy.[2] We simulate 5×10^4 years of SNe Ia, randomly distributed across the box, rejecting systems where $z_s < z_l$. For each remaining source, we solve the lens equation using `glafic` (Oguri 2010) to determine the macrolensing magnification, image multiplicity, and time delays. In total we generated 37,100 multiply imaged systems containing a total of 78,184 images. Since our simulation only covers $10^5/N_{\rm gal} \approx 0.026\%$ of the sky, this corresponds to a rate of 2,675 systems, all sky, per year to $z_s = 2$.

4.2.2 Microlensing Magnification Patterns

For each image we calculate a source-plane magnification pattern with `microlens` (Wambsganss 1990, 1999), an inverse ray-tracing code. In this scheme, stars modeled as point-mass deflectors are realized from a mass function at random locations in a two-dimensional field of the lens galaxy. The size of the pattern is characterized by the Einstein radius $\bar{R}_E$ of a deflector of mass $\bar{m}$ projected onto the source plane,

$$\bar{R}_E = \sqrt{\frac{4G\bar{m}}{c^2} \frac{D_{ls} D_s}{D_l}}, \tag{4.7}$$

where D_l is the angular diameter distance to the lens, D_s is the angular diameter distance to the source, and D_{ls} is the angular diameter distance between the lens and the source. Our magnification patterns are $10\bar{R}_E$ on a side, which for typical source and lens redshifts ($z_s = 1.2, z_l = 0.6$) corresponds to an angular scale of $10\bar{R}_E/D_s \approx 1.5 \times 10^{-5}$ arcsec. At the same redshifts, $\bar{R}_E \approx 2.7 \times 10^3$ AU, which is roughly 5 times larger than the extent of the supernova model near peak brightness.

The magnification patterns are specified by four parameters: (1) the local convergence, κ, (2) the local shear, γ, including the contributions of both the SIE and external potentials, (3) the fraction of the local convergence in stars, f_*,[3] and (4) the dynamic range of the stellar

[2] This box size was chosen to be large enough to accommodate the effects of ellipticity and external shear.

[3] The remainder of the convergence is assumed to take the form of continuously distributed matter (i.e., dark matter).

mass function, $q = m_{min}/m_{max}$. Supplying these parameters allows `microlens` to solve the general microlensing equation, $\boldsymbol{\beta} = \boldsymbol{\theta} - \boldsymbol{\alpha}$, which resolves to

$$\boldsymbol{\beta} = \begin{pmatrix} 1-\gamma-\kappa_c & 0 \\ 0 & 1+\gamma-\kappa_c \end{pmatrix} \boldsymbol{\theta} - \sum_{i=1}^{N_*} \frac{M_i(\boldsymbol{\theta}-\boldsymbol{\theta}_i)}{(\boldsymbol{\theta}-\boldsymbol{\theta}_i)^2}, \tag{4.8}$$

where $\kappa_c = (1-f_*)\kappa$ is the local convergence in continuously distributed matter, the two-dimensional vector $\boldsymbol{\beta}$ is the angular position of the source in the absence of lensing, $\boldsymbol{\theta}$ is the angular position of the observed macroimage, $\boldsymbol{\theta}_i$ is the angular position of the i'th star, and N_* is the number of stars in the field, determined from the local convergence in stars $\kappa_* = f_*\kappa$ using the procedure of Schneider & Weiss (1987).

We use a Salpeter (1955) mass function, $dn/dm \propto m^{-2.35}$, to model the population of stars in our microlensing calculations. As we will show in Section 4.3, this choice has no effect on our results as the achromaticity of glSN Ia microlensing is driven entirely by the color evolution of SNe Ia and not by the properties of the microlensing magnification patterns. Following Dobler & Keeton (2006b), we take the mean mass $\bar{m} = 1M_\odot$. The microlensing parameters κ and γ are determined by evaluating the SIE and external shear lensing potentials at the location of each image. f_* is estimated following the method of Dobler & Keeton (2006b), assuming a de Vaucouleurs stellar profile normalized so that the maximum $f_* = 1$. For each image, the dynamic range parameter q is sampled uniformly at random from $(0.1, 0.2, 0.5, 1.0)$, appropriate for the old stellar populations in elliptical galaxies. Figure 4.1 shows a random selection of nine of the maps, highlighting their morphological diversity. Figure 4.2 shows two dimensional projections of the joint distributions of the macrolensing parameters σ, e, and $\gamma_{\rm ext}$, the microlensing parameters κ, γ, and f_*, and the time- and wavelength-averaged microlensing magnification μ_{ML}.

4.2.3 Supernova Modeling

We use the well-understood, spherically symmetric[4] SN Ia atmosphere model W7 (Nomoto et al. 1984) to estimate the time- and wavelength-dependent magnification of glSNe Ia due to microlensing. This radiation transport model is the result of a one-dimensional explosion simulation in which a Chandrasekhar-mass carbon-oxygen white dwarf undergoes a deflagration. The explosion of the white dwarf completely unbinds the star and deposits the energy liberated by nuclear burning into the ejected mass. The deposited energy controls the velocity distribution of the ejecta and its density profile, which is assumed to reach homology seconds after the explosion. We use the time-dependent, Monte Carlo radiation transport code `SEDONA` (Kasen et al. 2006) to calculate the spectral time series of the model. Details of our `SEDONA` simulations appear in Appendix 4.A.

The observed spectrum F_λ of the model at wavelength λ and time t is obtained by convolving its time-evolving specific intensity with the lensing amplification pattern over a

[4]Spectropolarimetry indicates that SNe Ia are globally spherically symmetric to ∼a few percent. See Wang & Wheeler (2008a).

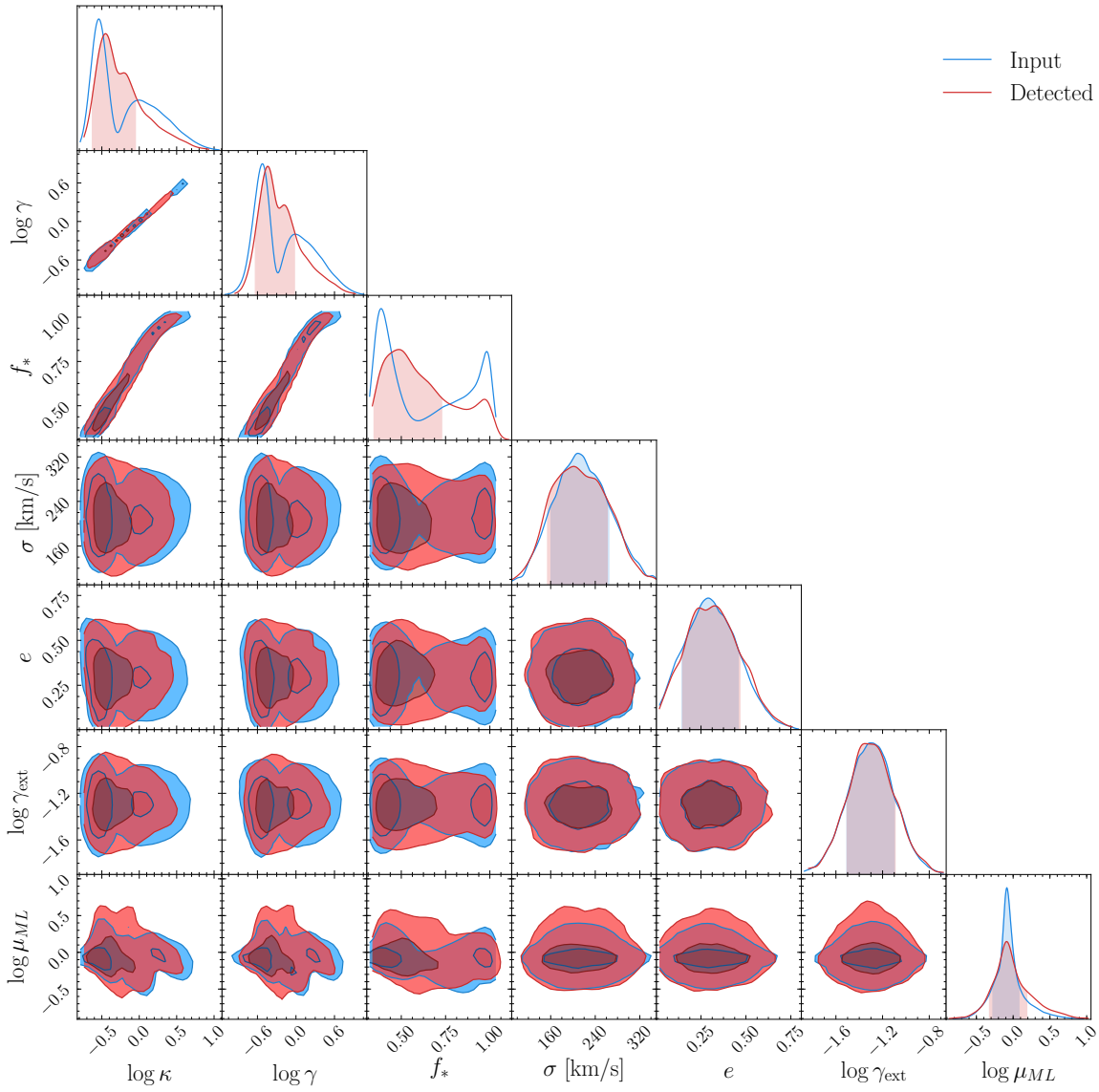

Figure 4.2: Two-dimensional projections of the joint distributions of lensed image macrolensing and microlensing parameters. The input distributions (blue) represent all 78,184 simulated lensed images from Section 4.2.1, and the detected distributions (red) represent only the images of the glSNe Ia detected in Section 4.4.2. The bimodal input distributions of f_*, γ, and κ represent the amplified ($f_* \approx 0.4$) and overfocussed ($f_* \approx 1$) images produced by SIE lenses. Joint contours show 1 and 2σ. Marginal shaded regions show 1σ.

plane normal to the observer's line of sight. Since the model is spherical, this integral takes the form:

$$F_\lambda(\lambda, t) = D_L^{-2} \int_0^{2\pi} \int_0^{P_m} I_\lambda(P, \phi, \lambda, t)\, \mu(P, \phi)\, P\, dP\, d\phi, \tag{4.9}$$

where ϕ and P are azimuthal and impact parameter coordinates on the plane, I_λ is the specific intensity of the model, μ is the lensing amplification,[5] D_L is the luminosity distance to the supernova, and P_m is the maximum impact parameter of the model. For a derivation of Equation 4.9, see Appendix 4.B. The time- and wavelength-dependent magnification of a given magnification pattern is obtained by dividing F_λ by the unlensed spectrum of the model (Equation 4.9 with $\mu = 1$).

We interpolate each magnification pattern bilinearly and convolve it with the redshifted[6] specific intensities of the supernova model. The redshift configurations control the projected size of the supernova on the magnification pattern and thus the magnification experienced by each differential element of the projected supernova atmosphere. They also control θ_E and thus κ, γ, and f_* at the location of the image. We always place the supernova model at the center of the magnification pattern. We model the homologous expansion of the supernova behind the magnification pattern (i.e., the projected size of the supernova on the magnification pattern changes with time), but not relative motion between the supernova and the lens galaxy star field. In general, supernova atmospheres both expand and move with respect to the lens galaxy, but the characteristic expansion velocity of the atmosphere ($\sim 10^4\,\mathrm{km\,s^{-1}}$) is much larger than the characteristic relative velocity between the lens galaxy and the supernova ($\sim 10^2\,\mathrm{km\,s^{-1}}$), so here we model only the effects of expansion.

4.3 Two Phases of Type Ia Supernova Microlensing

Example spectra and difference light curves of our microlensed SN Ia atmosphere appear in Figures 4.3 and 4.4, respectively; confidence regions of all $U-B$, $B-V$, $V-R$, and $R-I$ color curves produced by our simulation appear in Figure 4.5. The difference light curves give the microlensing amplification in magnitudes,

$$\Delta M(t) = -2.5 \log_{10} \left(\frac{L(t)}{\mu_0 U(t)} \right), \tag{4.10}$$

where $U(t)$ and $L(t)$ are the unlensed and observed fluxes of the supernova, respectively, and μ_0 is the magnification in the absence of microlensing (i.e., if there were only macrolensing due to the lens galaxy). In the absence of microlensing, $\Delta M = 0$.

Each of these figures demonstrates that glSN Ia microlensing has two phases, an "achromatic" phase, in which the microlensing magnification is the same at all wavelengths to a few

[5] In this paper, μ refers exclusively to lensing amplification. Nowhere should μ be interpreted as $\mu = \cos\theta$, the viewing angle parameter that frequently appears in supernova modeling papers.

[6] We refer here to cosmological redshift only; Doppler shifts due to supernova expansion velocity are accounted for implicitly in the radiation transport simulation.

millimag, followed by a "chromatic" phase, in which the microlensing magnification varies strongly (and unpredictably) with wavelength. The difference light curves show that the achromatic phase lasts roughly 3 rest-frame weeks after the explosion, transitioning to a chromatic phase between the time of peak brightness and the onset of the infrared secondary maximum. During the achromatic phase, the light curves of glSNe Ia can be deformed enough to bias time delay extraction; although ΔM is the same in all bands, it is not necessarily constant in time.

4.3.1 Physics of Achromatic and Chromatic SN Ia Microlensing

What is the physics responsible for the "achromatic" and "chromatic" phases of microlensing evident in Figures 4.4 and 4.5? Figure 4.6 shows the specific intensity profile $I_\lambda(v)$ of our unlensed model at 20 and 40 days after explosion, where v is the velocity of the shell, equivalent to a radial variable (i.e., P).[7] The left panel of the figure shows that near peak (20 days after explosion), the ratio $I_{X_1}(v)/I_{X_2}(v)$, where X_1 and X_2 are any two bands, is roughly constant over all v. Thus the supernova near peak has a specific intensity profile that is independent of v up to an overall normalization factor. As a result, any magnification pattern $\mu(P, \phi)$ will not change its color.

However, after peak, the supernova expands and cools enough for some part of the atmosphere to reach a temperature of 7000K. Kasen (2006a) and Kasen & Woosley (2007) note that this is the temperature at which Fe III recombines to Fe II, which presents a significantly higher opacity to blue and ultraviolet radiation than Fe III. This line blanketing has the effect of enabling one to see redder emission from deeper in the supernova, while emission in the blue and the UV is pushed to larger radii. Additionally, a "fluorescent shell" of iron recombination, which causes a peak in the redder bands in the specific intensity profile of the supernova, develops near the onset of the secondary maximum. This shell is clearly visible in the righthand panel of Figure 4.6. These two effects, line blanketing and a fluorescent shell, make the supernova's specific intensity ratio no longer spatially constant. As a result, the supernova atmosphere becomes susceptible to chromatic fluctuations.

4.4 The Effect of Microlensing on LSST Lensed Type Ia Supernova Yields

Previous estimates of glSN Ia yields, including those of Oguri & Marshall (2010), Quimby et al. (2014), and Goldstein & Nugent (2017), modeled only the effects of macrolensing. In this section, we present a novel method of identifying glSNe Ia photometrically based on spectral template fitting. We apply this technique to our simulated micro- and macrolensed glSN Ia light curves to present a new estimate of glSN Ia yields for LSST.

[7] As our model is spherically symmetric, I_λ possesses no ϕ-dependence.

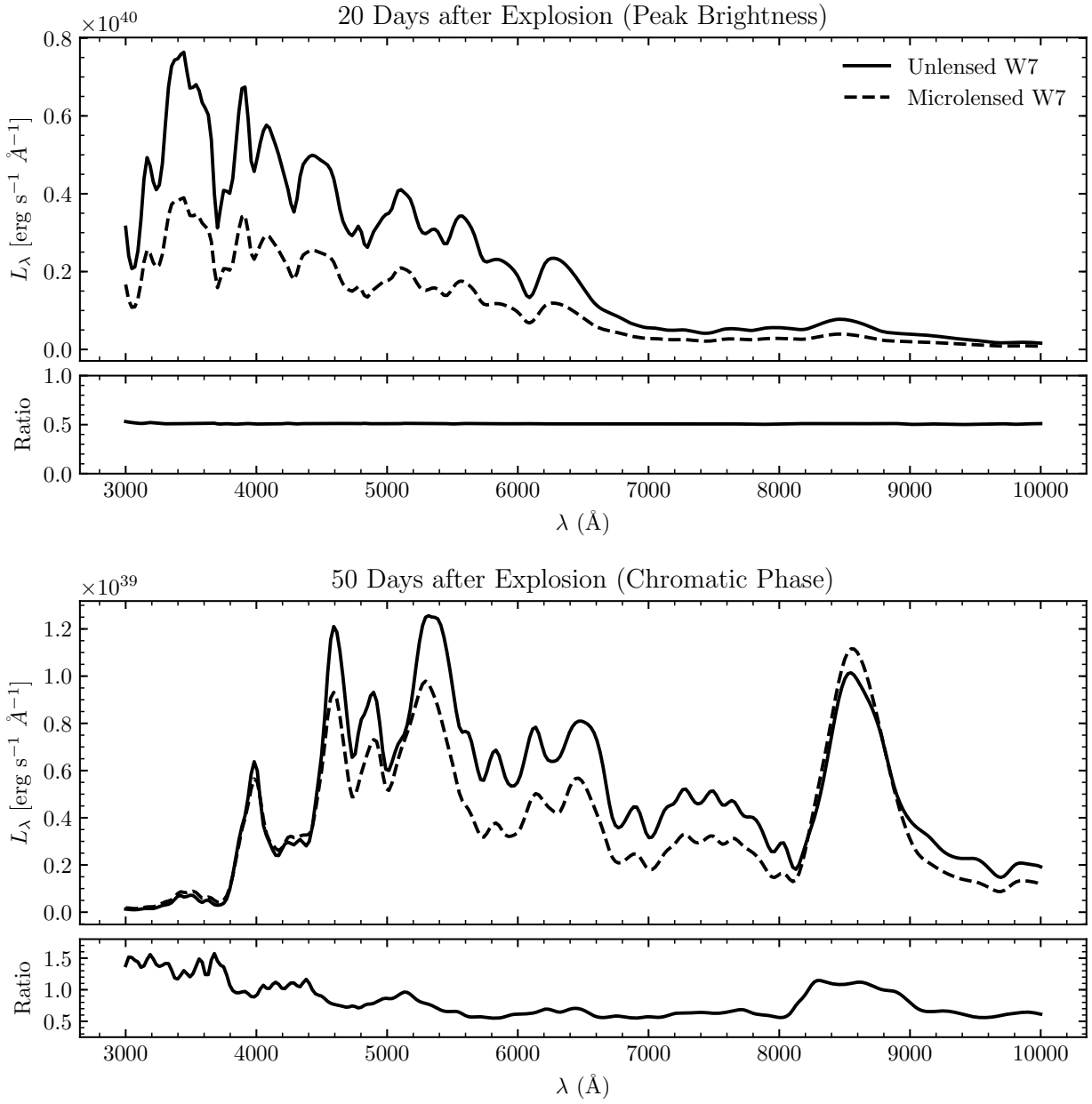

Figure 4.3: Rest-frame spectra of model W7 (Nomoto et al. 1984) computed with `SEDONA` near peak brightness and well into the onset of the infrared secondary maximum. The solid curve is unlensed and the dashed curve is lensed by star field (h) from Figure 4.1. Near peak brightness, microlensing does not have a large effect on the shape of the spectrum or the relative strengths of its features. During the chromatic phase, lensing-induced continuum shifts and spectral line distortions are visible in the ratios of the spectra. Such chromatic distortions can affect the colors of the supernova.

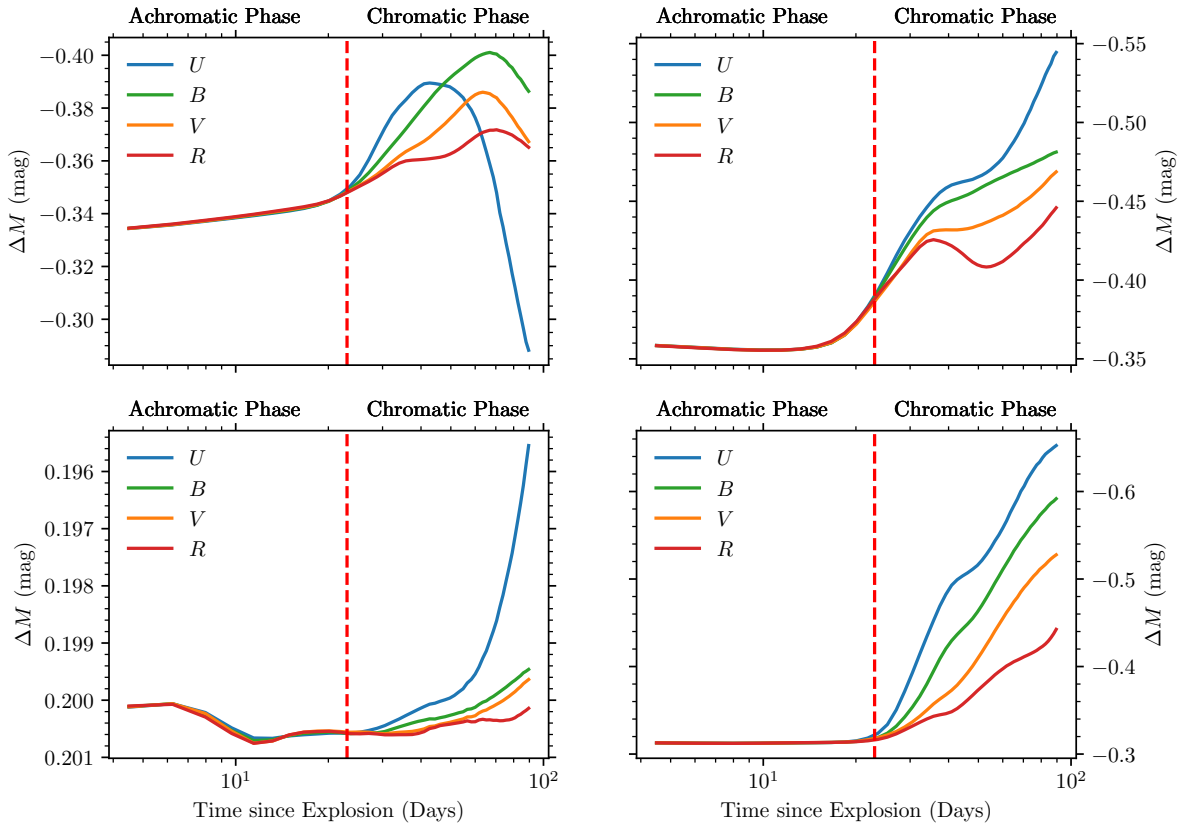

Figure 4.4: Four randomly chosen examples of broadband rest-frame difference light curves of model W7 computed by `SEDONA`. Each set of difference light curves has two distinct phases: an "achromatic" phase in which ΔM is the same in all bands to within a few millimag, and a "chromatic" phase in which ΔM can vary significantly from band to band.

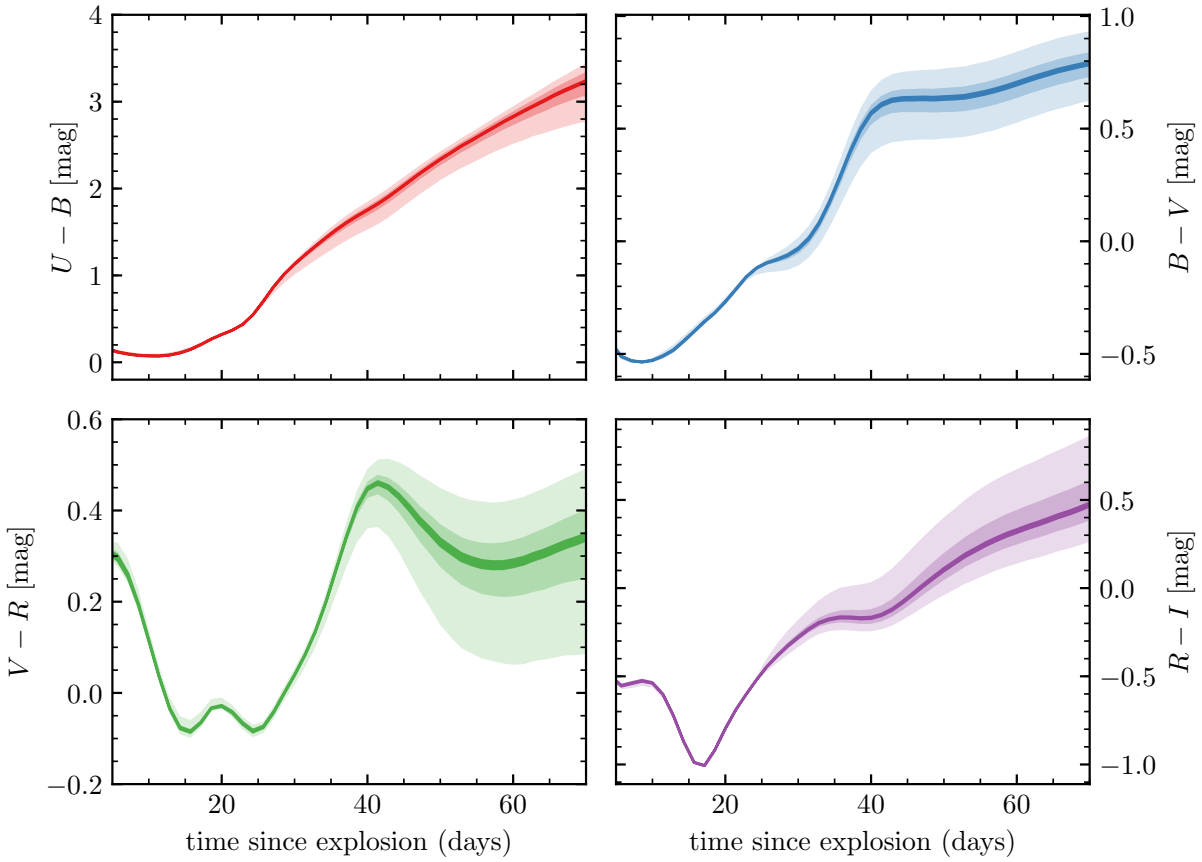

Figure 4.5: Rest-frame microlensed color curves of model W7. The intervals containing 68%, 95%, and 99% of the 78,184 microlensed color curves described in Section 4.3 are plotted as progressively less opaque shaded regions. The color curves of the unlensed model are indistinguishable from the 68% confidence regions of the microlensed models.

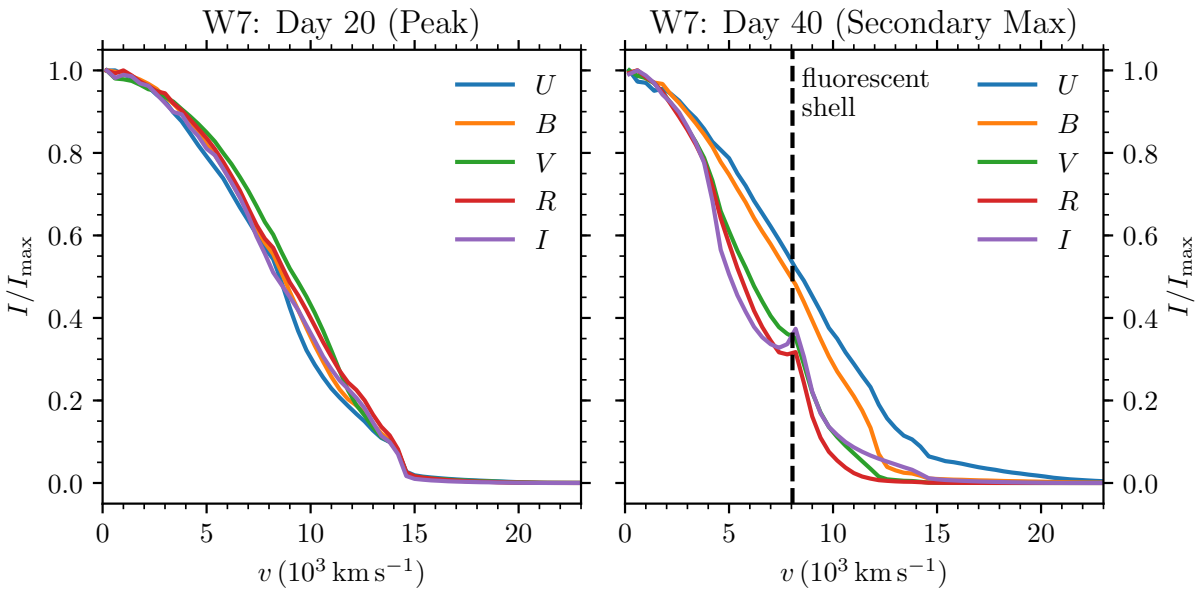

Figure 4.6: Normalized projected specific intensity profiles of model W7. Near peak, the specific intensity profiles in $UBVRI$ are similar, so microlensing is achromatic. At day 40, UV line blanketing and the "fluorescent shell" (in which Fe III $\rightarrow$ Fe II recombination occurs) causes different bands have different specific intensity profiles. As a result, microlensing is chromatic at this stage.

4.4.1 Efficient Identification of Lensed Type Ia Supernovae with Spectral Template Fitting

Our detection strategy rests on three observational facts. First, normal SNe Ia are the brightest type of supernovae that have ever been observed to occur in elliptical galaxies (Maoz et al. 2014). Second, the absolute magnitudes of normal SNe Ia in elliptical galaxies are remarkably homogenous, even without correcting for their colors or lightcurve shapes ($\sigma_M \sim 0.4$ mag), with a component of the population being underluminous (Li et al. 2011). Finally, due to the sharp 4000Å break in their spectra, elliptical galaxies tend to provide accurate photometric redshifts from large-scale multi-color galaxy surveys such as SDSS.

A high-cadence, wide-field imaging survey can leverage these facts to systematically search for strongly lensed SNe Ia in the following way. First, by spatially cross-matching its list of supernova candidates with a catalog of elliptical galaxies for which secure photometric redshifts have been obtained, supernovae that appear to be hosted by elliptical galaxies can be identified. The hypothesis that one of these supernovae actually resides in its apparent host can be tested by fitting its broadband light curves with an SN Ia spectral template (as SNe Ia are the only types of supernovae that occur in ellipticals) fixed to the photometric redshift of the galaxy and constrained to obey $-18.5 > M_B > -20$, a liberal absolute magnitude range for SNe Ia, assuming a fiducial cosmology. If the transient is a lensed supernova at higher redshift, then the spectral template fit will fail catastrophically, as the supernova light curves will be strongly inconsistent with the redshift and brightness implied by the lens galaxy.

4.4.2 Monte Carlo Simulation

We use SALT2 (Guy et al. 2007), a parametrized SN Ia spectral template that is the *de facto* standard tool to place SNe Ia on the Hubble diagram, to test this method. The template possesses four parameters: t_0, x_0, x_1, and c, encoding a reference time, an overall SED normalization, a supernova "stretch," and a color-law coefficient, respectively. The flux of the template is given by

$$F_\lambda(\lambda, t) = x_0[M_0(\lambda, t) + x_1 M_1(\lambda, t)] \exp[c\, CL(\lambda)], \tag{4.11}$$

where M_0 and M_1 are eigenspectra derived from a training sample of measured SN Ia spectra and $CL(\lambda)$ is the average color-correction law of the sample (see Guy et al. 2007, for details). The template aims to model the mean evolution of the SED sequence of SNe Ia and its variation with a few dominant components, including a time independent variation with color, whether it is intrinsic or due to extinction by dust in the host galaxy (or both).

We consider an LSST lensed supernova search in which the photometry is performed with a PSF that is artifically enlarged to blend the multiple images together into a single source. We randomly assign each of the 37,100 simulated glSNe Ia from Section 4.2.1 an LSST field from the nominal observing strategy (`minion_1016`; LSST Science Collaborations

in preparation).[8] We compute the phase- and wavelength- dependent magnification $\mu(\lambda, t)$ of each lensed image by placing its corresponding microlensed W7 SED into the rest frame, then dividing each by the unlensed spectral sequence of the model. We then generate the rest-frame spectral model for the image $F(\lambda, t)$ according to

$$F(\lambda, t) = \mu(\lambda, t)H(\lambda, t), \tag{4.12}$$

where $H(\lambda, t)$ is the Hsiao et al. (2007) SN Ia spectral template. We employ a warped Hsiao template rather than the microlensed W7 SEDs to mitigate uncertainties in the radiation transport.[9] We then place the templates of each image at their correct redshifts, and we rescale and time-shift them to account for the macrolensing and time delays. Finally, we draw a random time for the system (arbitrarily chosen to be the observer-frame time of rest-frame B-band maximum of the first image) from the 11 year period spanning 6 months before the beginning of the survey until 6 months following the end of the survey.

We realize broadband photometry of each blended glSN Ia (summing the flux of each microlensed image) using the sky brightnesses, FWHMs, exposure times, observation times, and limiting magnitudes of the assigned field provided by `minion_1016`, assuming the total area covered by the survey is 25,000 deg^2. Starting from the first observation of the SN Ia, we fit the light curve with SALT2, fixed to the redshift of the lens galaxy (assumed to be known either as a photometric or spectroscopic redshift) and fixed to obey $-18.5 > M_B > -20$ at that redshift (effectively a constraint on x_0). Additionally, we enforce bounds of $[-0.2, 0.2]$ on c and $[-1, 1]$ on x_1, values characteristic of normal SNe Ia (Scalzo et al. 2014a). We use the CERN minimization routine `MIGRAD` (James & Roos 1975) to fit the data. If the light curve has at least one data point that is at least 5σ discrepant from the best fit and at least 4 data points with S/N ≥ 5, then the object is marked "detected." If not, then the next observation is added and the process is repeated until the object is detected or all observations are added, resulting in a non-detection.

Figure 4.7 shows an example of this procedure being used to detect one of our simulated glSNe Ia at $z_s = 1.91$. The red data points show the "current" light curve, and the red line shows the best fit model, fixed to $z_l = 0.96$. Although the model fits the data well in the bluer bands, the high redshift of the source makes the data much brighter in the infrared than the model expects given the redshift of the lens. Thus the object is detected shortly after peak due to 10σ discrepant points in y-band.

4.4.3 Yields

Our spectral template fitting approach to glSN Ia identification delivers almost twice as many LSST glSNe Ia than the method of Goldstein & Nugent (2017). In total, LSST

[8] https://github.com/LSSTScienceCollaborations/ObservingStrategy

[9] The Hsiao template is an empirical, time-dependent SED model constructed from the observed spectra of many SNe Ia but it does not contain position dependent information (i.e., P, ϕ), so to calculate $\mu(\lambda, t)$ theoretical models are needed. The Hsiao template is more accurate than the theoretical model in the IR and after maximum light when NLTE effects become important.

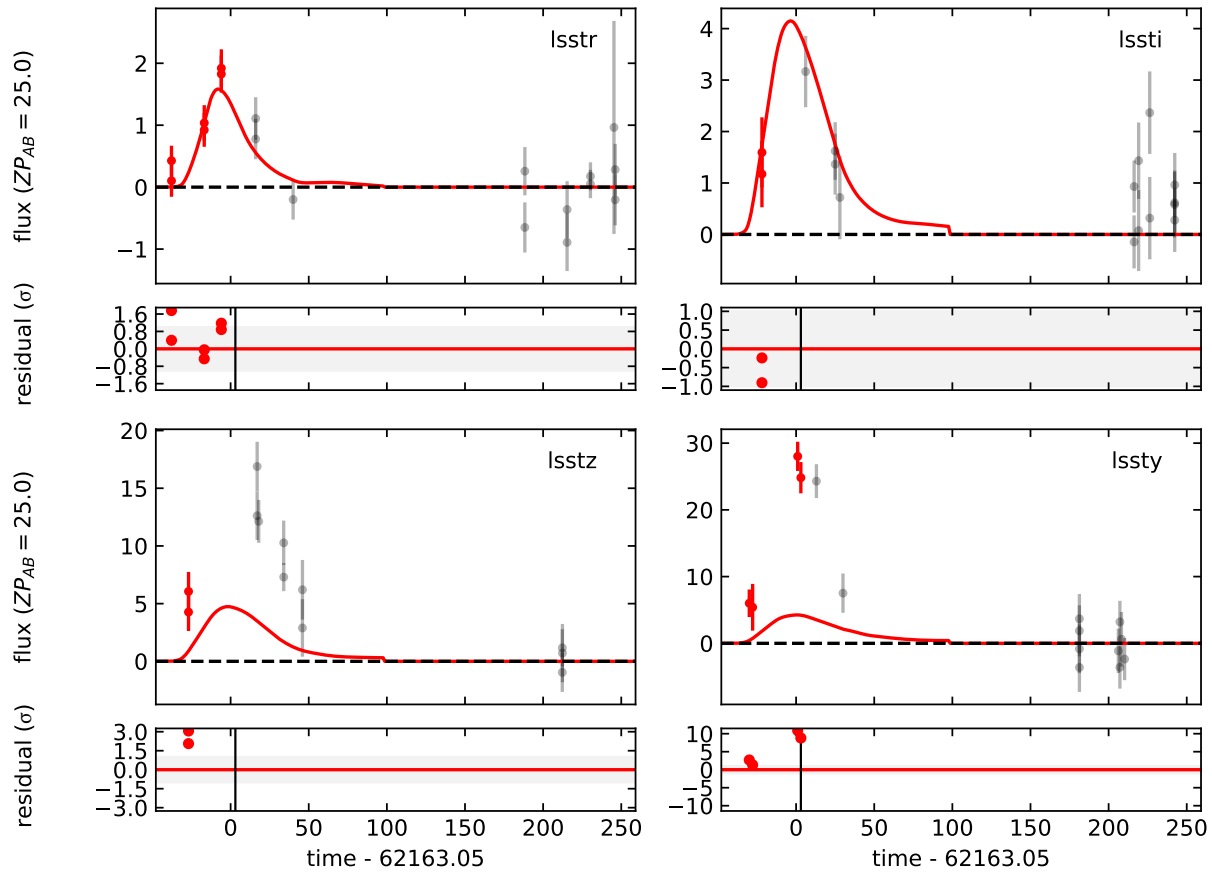

Figure 4.7: Detecting a $z_s = 1.91, z_l = 0.96$ LSST glSN Ia with SALT2. The red data points show the "current" light curve, and the red line shows the best fit SALT2 model fixed to the photometric redshift of the lens galaxy. The gray points show future observations that are not included in this iteration of the fit. The black vertical line in the residual plots shows the date when the supernova is detected. Although the model fits the data well in the bluer bands, the high redshift of the source makes the data much brighter in the infrared than the model expects given the redshift of the lens. Thus the object is detected shortly after peak due to 10σ discrepant points in y-band.

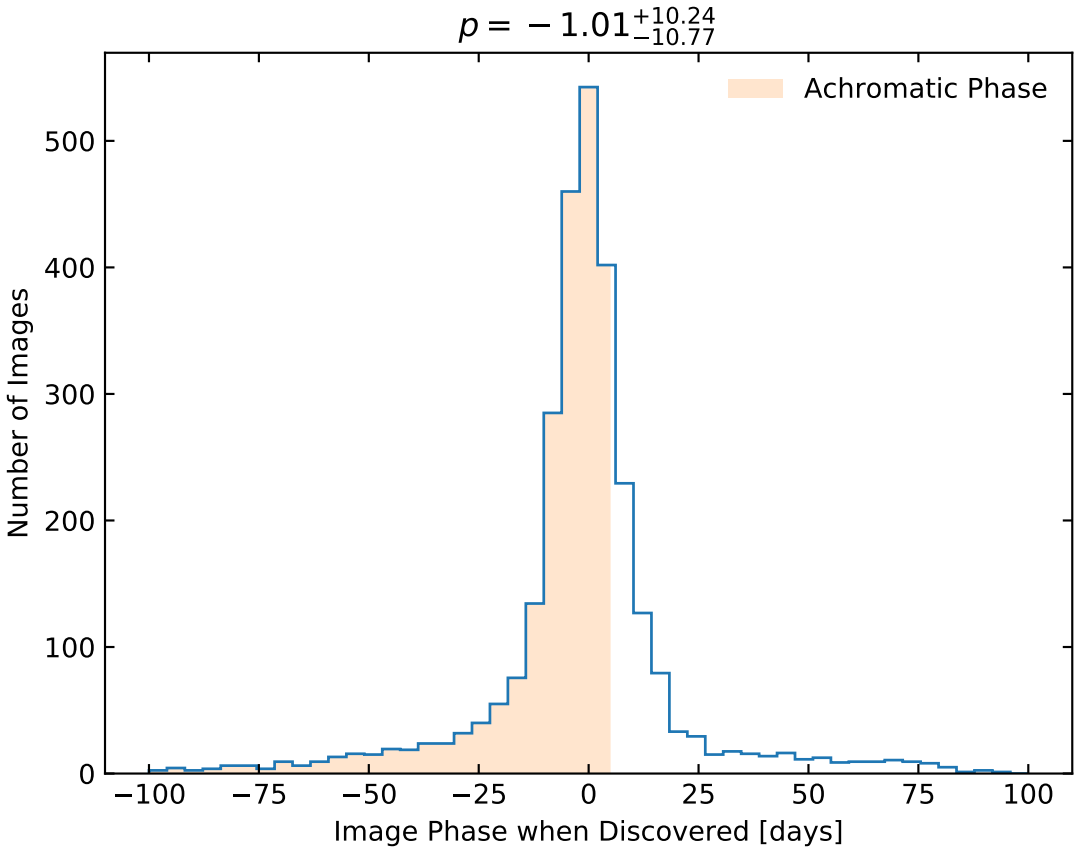

Figure 4.8: Phases of detected gLSN images when they are discovered. Phases are given relative to each image, not to the peak of the total flux of the multiple blended images of SN. 73% of the images and 64% of the image pairs are discovered during the achromatic phase.

should find ∼925 microlensed glSNe Ia with the new method over the duration of its 10-year survey. This is almost identical to the case with no microlensing, which would yield 935 glSNe Ia over the same period, with a nearly identical redshift distribution (see Figure 4.9). This represents a major increase in the expected glSN Ia yield for LSST, comparable to the number of expected lensed quasars (Oguri & Marshall 2010).

Figure 4.8 shows the rest-frame phase distribution of discovered microlensed glSN Ia images (a phase of 0 corresponds to peak brightness in B). The 68% confidence interval of the image phase distribution is $-1.01^{+10.24}_{-10.77}$, so about half of the images should be discovered before peak brightness. 73% of the images and 64% of the image pairs should be discovered during the achromatic phase.

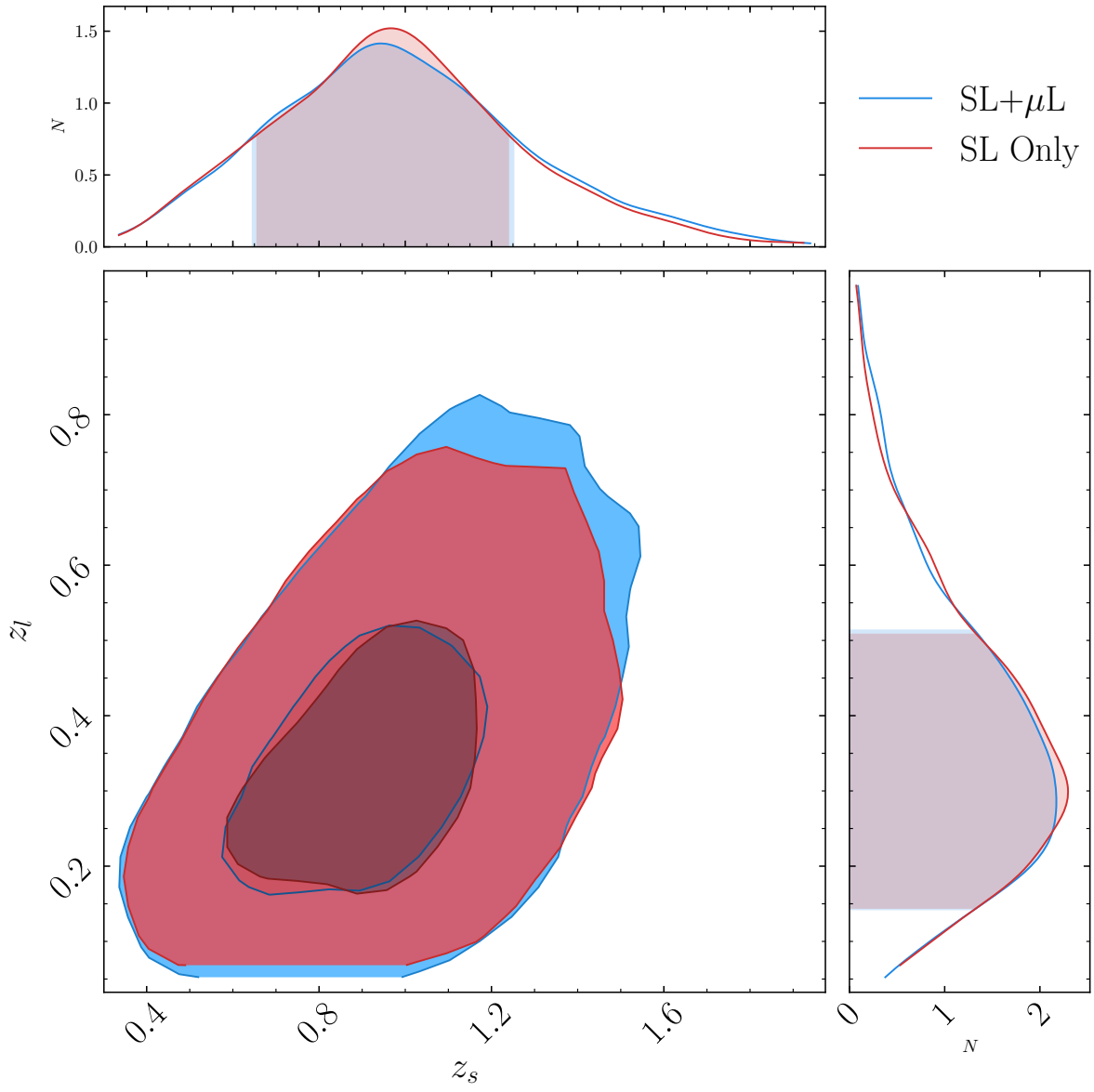

Figure 4.9: Source and lens redshift distributions of the gLSNe Ia with at least 4 data points with S/N > 5 detected with (blue) and without microlensing (red). The joint contours show 1 and 2σ. The marginal shaded regions show 1σ.

4.5 The Effect of Microlensing on Lensed Type Ia Supernova Time Delays

In Section 4.3, we showed that microlensing introduces time- and wavelength-dependent fluctuations into the light curves of SNe Ia. In this section, we quantify the effect of these fluctuations on the time delays that can be extracted from simulated photometric observations of typical LSST glSNe Ia, using as input the results of Section 4.4.3. We demonstrate that microlensing can introduce time delay uncertainties of ∼4% into the light curves of typical LSST glSNe Ia, but that this number decreases to ∼1% when achromatic-phase color curves of the same supernovae are used instead.

4.5.1 Monte Carlo Simulations of Microlensing Time Delay Uncertainty

Since many of the glSNe Ia that will be discovered by LSST will require higher-spatial resolution follow-up observations to extract time delays, either with ground-based adaptive optics or space-based imaging, we simulate "time-delay observations" with the Wide Field Camera 3 (WFC3) on the *Hubble Space Telescope* (*HST*). The redshift distribution in Figure 4.9 implies that most LSST glSNe Ia will be brightest in the IR, so we use the F814W, F125W, and F160W filters (roughly I, J, and H bands, respectively) on WFC3 for this simulation.

For each of the "detected" microlensed glSN Ia systems from Section 4.4.3, we realize 45 photometric observations of each image in F814W, F125W, and F160W with infinite signal to noise, with a uniform temporal spacing, spanning the light curve. The spectral template for each image is the same as the one used in Section 4.4 (see Equation 4.12). Using `MIGRAD`, we fit the realized light curves of each pair of images using the redshifted, unlensed spectral template $H(\lambda, t)$. For each fit, we estimate the fitted time delay as

$$\Delta t = t_{0,2} - t_{0,1}, \tag{4.13}$$

where $t_{0,2}$ and $t_{0,1}$ are the fitted reference times of the second and first images, respectively. We then measure the error on the fitted time delay as

$$\epsilon = \left| \frac{\Delta t - \Delta t'}{\Delta t'} \right|, \tag{4.14}$$

where $\Delta t'$ is the true time delay of the pair of images.[10]

Next, we prune the photometric observations to the achromatic phase, masking all observations more than 5 rest-frame days from the date of B-band maximum. We then synthesize F814W − F125W, F125W − F160W, and F814W − F160W color curves from the photometry.

[10]N.B. If Δt is distributed as a Gaussian with width σ, then the ensemble average of ϵ is only 0.79σ.

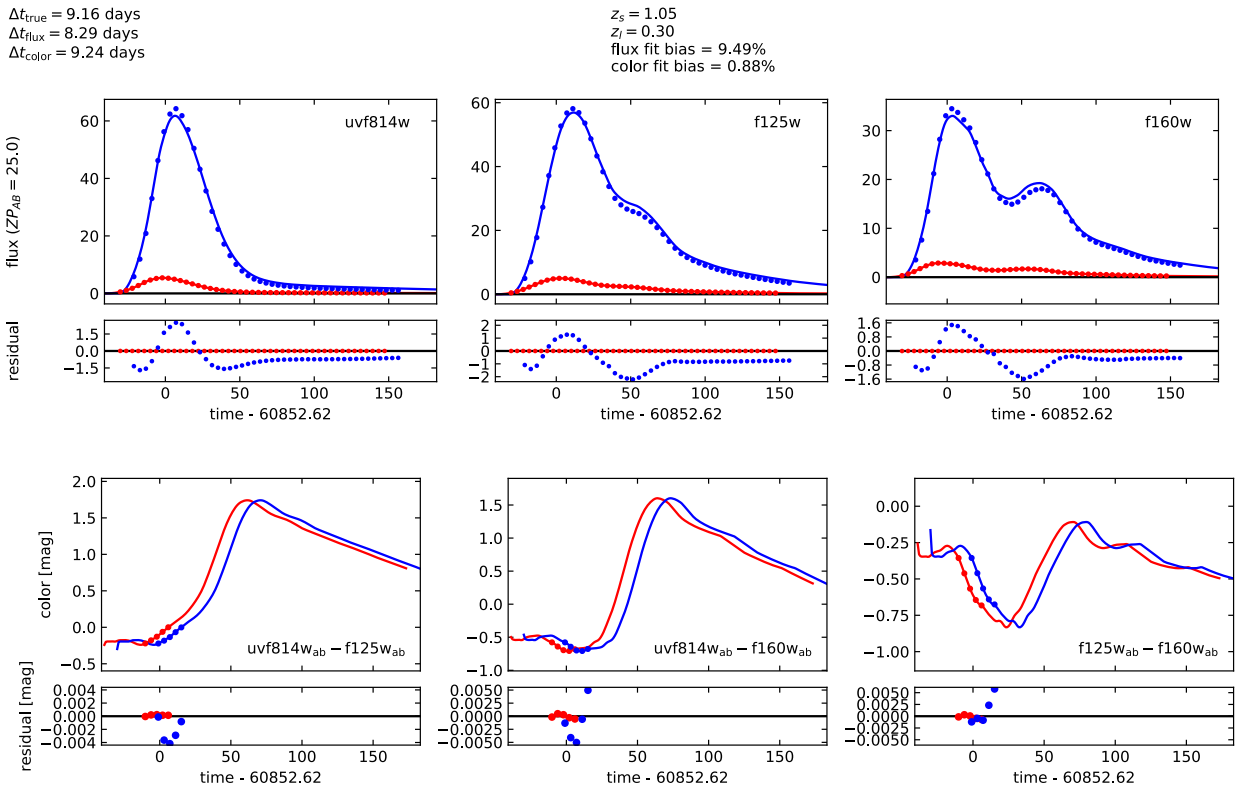

Figure 4.10: Fitting infinite S/N light curves and color curves (in the achromatic phase) of two images of a microlensed supernova with the unlensed Hsiao template to estimate time delay error. Microlensing produces visible offsets in the features of the light curves, but the residuals show that during the achromatic phase (until a few weeks after peak brightness) the offsets are achromatic. Thus when the color curves are fit in the achromatic phase, the uncertainty on the time delay is more than an order of magnitude smaller.

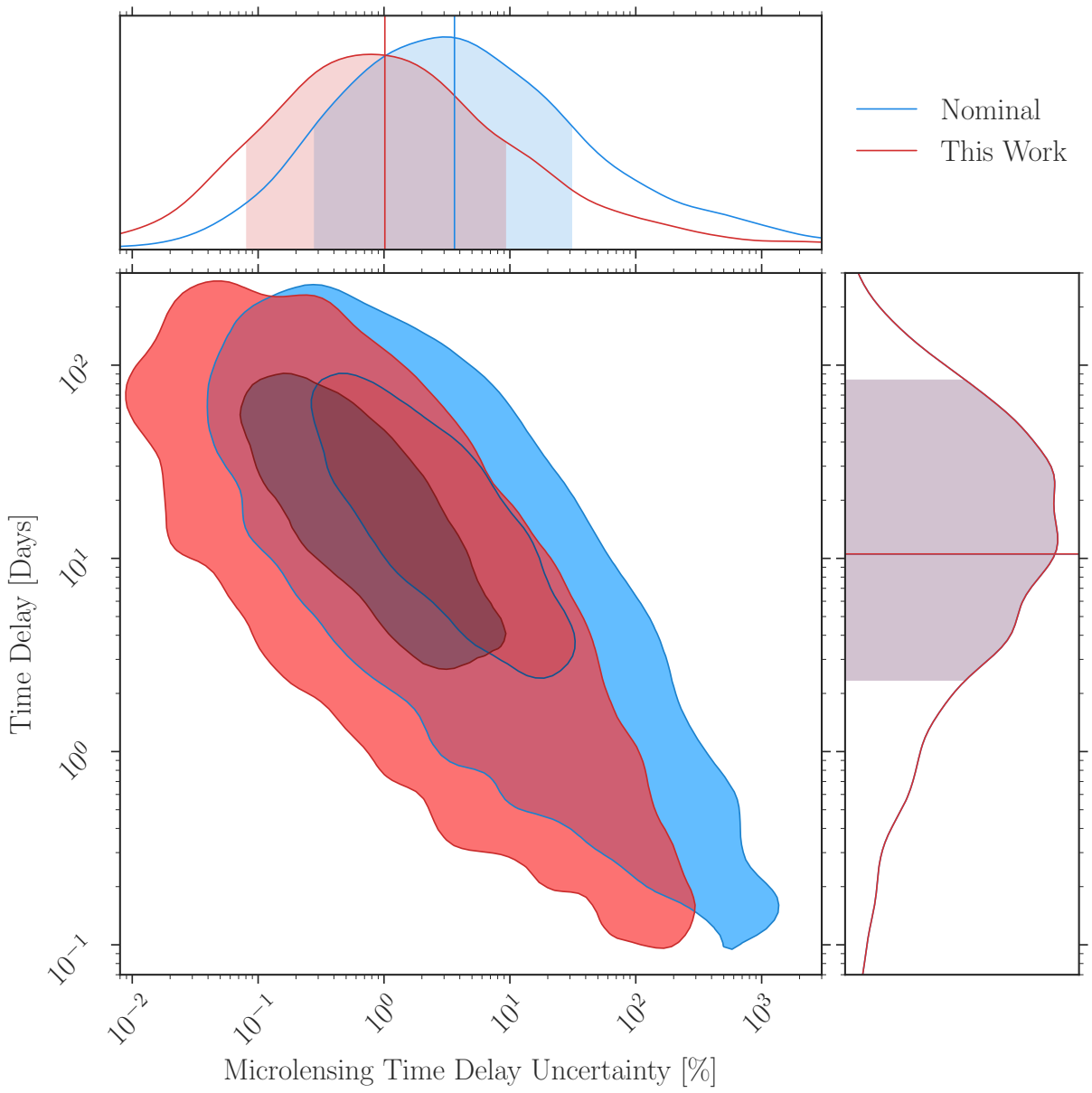

Figure 4.11: Joint distribution of the true time delay and the microlensing time delay uncertainty as a percentage of the true time delay for all discovered pairs of glSN Ia images. The median time delay uncertainty is 4% for light curves, but just 1% for color curve measurements in the achromatic phase. The median time delay that LSST will detect is 10 days. Contours show 1 and 2σ. Marginal shaded regions show 1σ.

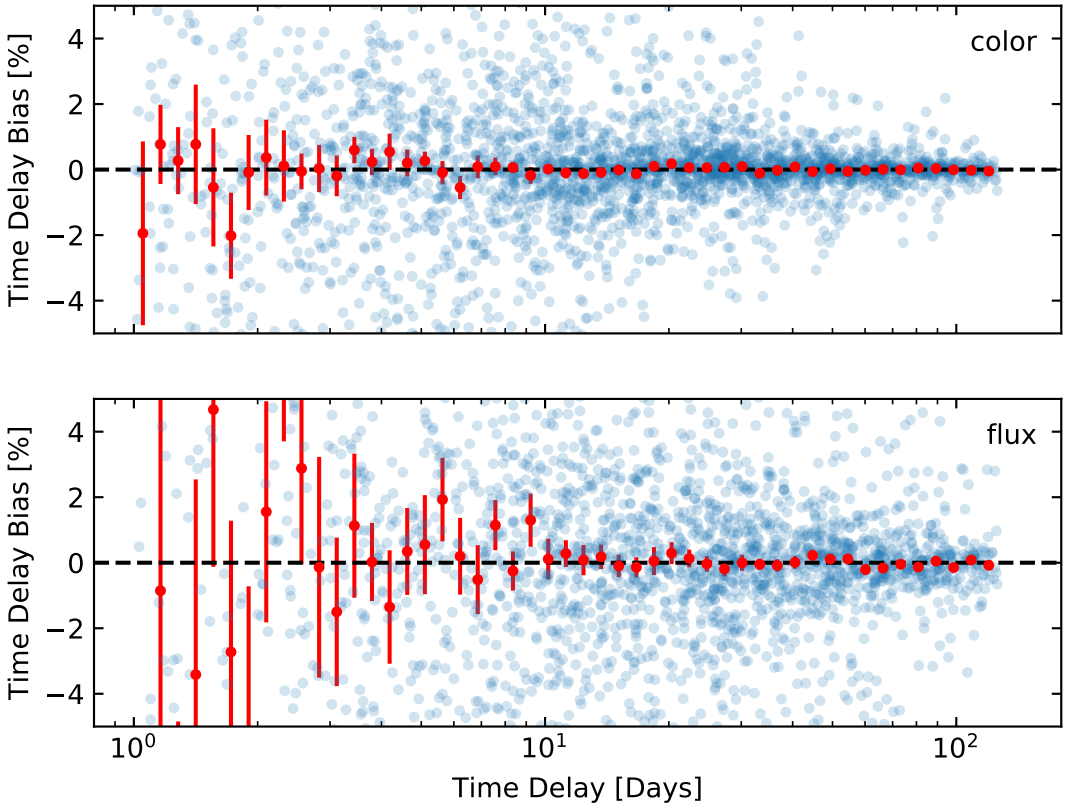

Figure 4.12: Bias as a function of true time delay for all discovered microlensed image pairs, fitting color curves in the achromatic phase (top panel) and entire light curves (bottom panel). Blue points show individual fits; red points show bin averages.

We apply the same fitting procedure to the color curves and estimate the fitted time delays and uncertainties using Equations 4.13 and 4.14. Figure 4.10 shows an example of the procedure being applied to the light curves and achromatic-phase color curves of two images of a supernova. While the light curve data show microlensing-induced offsets near peak brightness and the secondary maximum that produce a large time delay error of ∼10%, the residuals show that these offsets are nearly the same in all bands during the achromatic phase, and thus the fits to the color curve have errors $< 1\%$.

Figure 4.11 shows the joint distribution of time delays and microlensing-induced time delay uncertainties for all detected pairs of images in our simulation. We find that the median time delay of detected pairs of images is ∼10 days, and that the median microlensing-induced time delay uncertainty using light curve fits is 4%, comparable to the current uncertainties on mass modeling. However, this number drops down to 1% (∼2.5 hours on a 10 day time delay) when achromatic-phase color curves are used instead of light curves.

Figure 4.12 shows the systematic microlensing bias on time delays from fitting light curves and color curves in the achromatic phase. The achromatic phase color curve fits are consistent with zero bias down to $\Delta t = 1$ day, while the light curve fits are consistent with zero bias down to $\Delta t =$∼a few days. This result indicates that time delay bias from microlensing will not be a major systematic for cosmography with glSNe Ia.

4.5.2 iPTF16geu

iPTF16geu is the only glSN Ia with resolved images that has been discovered to date. Here we consider its potential time delay precision and cosmological impact. Before it faded, multiwavelength follow-up observations of the event were obtained with a variable cadence using the Washington C, g, r, wide I, Z, J, and H bands of WFC3 on *HST* (DD 14862, PI: Goobar). The bluer bands were only observed sporadically, but the redder bands were observed with a roughly 4-day cadence.[11] Unfortunately, the observations were obtained well into the chromatic phase, and thus the light curves and color curves exhibit significant microlensing uncertainties. Final photometry of the event has not yet been produced, as not enough time has passed to take final reference images. The current best estimate of the time delay on this system is 35 hours (Goobar et al. 2017). Based on Figure 4.11, we estimate the time delay uncertainty due to microlensing from this event to be ∼40%. If the event were discovered earlier so that color curves during the achromatic phase could be constructed, then the microlensing time delay uncertainty would drop to ∼10%.

4.6 Conclusion

In this article, we assessed the impact of microlensing on the yields and time delay precisions of LSST glSNe Ia. We presented microlensed broadband difference light curves and color curves of the well-understood SN Ia ejecta model W7 for 78,184 microlensing

[11] A full description of the observations is available here.

magnification patterns drawn from a realistic population model of glSN Ia images. We found that until shortly after peak brightness, the microlensing of SNe Ia is achromatic, and thus time delays from early-time color curves are less sensitive to microlensing than time delays from light curves. We interpreted the achromaticity of microlensing before the onset of the secondary maximum as being due to UV line blanketing and the emergence of a fluorescent shell of Fe III $\rightarrow$ II recombination that alters the specific intensity profile of the ejecta as suggested by Kasen (2006a) and Kasen & Woosley (2007). We found that microlensing does not have a significant impact on glSN Ia yields, but that they can be increased by a factor of $\sim$2 over the predictions of Goldstein & Nugent (2017) using a novel photometric detection techinque.

Our `SEDONA` calculation of W7 represents the most detailed SN Ia spectrum synthesis calculation that has been used to investigate SN Ia microlensing to date, but it is inherently one-dimensional and makes a number of physical approximations for computational expediency. It does not perfectly reproduce the observed colors of SNe Ia, especially at UV wavelengths, where line blanketing is strong and small differences in the underlying model can have pronounced effects. Additionally, W7 is just one SN Ia model, and there is diversity in the SN Ia population. However, we expect that this model captures the key physical behavior that leads to chromatic effects, and so we do not expect the results to change significantly with different one-dimensional models. Although there is evidence from spectropolarimetry that global asymmetry in SNe Ia is very small (Wang & Wheeler 2008a), asymmetric explosion scenarios have not been ruled out by observations. In the future, it will be useful to assess whether asymmetric, multi-dimensional supernova models confirm the two phases of glSN Ia microlensing identified in this work, or whether viewing angle effects become important.

Despite the complication of microlensing, time-delays can be robustly measured to sub-percent precision for many glSNe Ia. By photometrically detecting the first image of a strongly lensed core-collapse supernova before light from the other images arrives, one can use the sharp shock-breakout light curve as a time delay indicator with precision $\sim(30\,\mathrm{min})(1+z_s)/\Delta t$. Such precision is difficult to achieve with lensed AGNs (Tewes et al. 2013; Bonvin et al. 2017; Tie & Kochanek 2017), which also require a significantly longer observing campaign (Liao et al. 2015). This result provides a straightforward first step to inferring cosmological parameters with glSNe Ia. The latter steps of inferring the lens potential, and the effect of line-of-sight structures have already been implemented for lensed AGNs (e.g. Suyu et al. 2017; Rusu et al. 2017; Wong et al. 2017; Bonvin et al. 2017), and the solutions from lensed AGNs should be directly portable to glSNe Ia. Inferring the lens potential may even be easier than for AGNs as a more detailed reconstruction of the lensed SN Ia host should be possible once the supernova has faded. Those lensed SNe Ia with time-delays greater than a month are therefore golden lenses with which to measure H_0. With a method for extracting precise time delays from these objects in hand, a renewed focus should be placed on the discovery and follow up of glSNe Ia.

Appendix

4.A Radiation Transport Simulation

In this Appendix, we provide the details of the radiation transport simulations that we use to calculate the time-evolving SN Ia SED in Section 4.2.3. The `SEDONA` code (Kasen et al. 2006) is a time-dependent, multi-dimensional Monte Carlo radiative transfer code, designed to calculate the light curves, spectra and polarization of supernova explosion models. Given a homologously expanding SN ejecta structure, `SEDONA` calculates the full time series of emergent spectra at high wavelength resolution. In the present calculations, we employ a modified version of `SEDONA` that tags photons with their P and ϕ values, thus we calculate $I_\lambda(P, \phi, t, \lambda)$. In addition to being fully time-dependent, the `SEDONA` calculation accounts for the extendedness of continuum emitting regions in SN Ia atmospheres and the wavelength dependence of their location and extent. It also explicitly accounts for light travel time across the atmosphere. Broadband light curves are constructed by convolving the synthetic spectrum at each time with the appropriate instrumental throughputs. `SEDONA` includes a detailed treatment of gamma-ray transfer to determine the instantaneous energy deposition rate from radioactive ^{56}Ni and ^{56}Co decay. Other decay chains that can change the composition of the ejecta, such as $^{48}\mathrm{Cr} \rightarrow ^{48}\mathrm{V} \rightarrow ^{48}\mathrm{Ti}$, are not treated. Radiative heating and cooling rates are evaluated from Monte Carlo estimators, and the temperature structure of the ejecta is determined by iterating the model to thermal equilibrium.

Several significant approximations are made in our `SEDONA` simulation, notably the assumption of local thermodynamic equilibrium (LTE) in computing the atomic level populations. In addition, bound-bound line transitions are treated using the expansion opacity formalism (implying the Sobolev approximation; Jeffery 1995). In this formalism, the opacities of spectral lines within a wavelength bin are represented in aggregate by a single effective opacity. Although the `SEDONA` code is capable of a direct Monte Carlo treatment of NLTE line processes, due to computational constraints this functionality is not exploited here. Instead, the line source functions are treated using an approximate two-level atom approach. In the present calculations, we assume for simplicity that all lines are "purely absorptive," i.e., in the two-level atom formalism the ratio of the probability of redistribution to pure scattering is taken to be $\epsilon_{\rm th} = 1$ for all lines. In this case, the line source functions are given by the Planck function, consistent with our adoption of LTE level populations.

The numerical gridding in the present calculations was as follows: *spatial:* 100 equally

spaced radial zones with a maximum velocity of 4×10^4 km s^{-1}; *temporal:* 459 time points beginning at day 1 and extending to day 100 with logarithmic spacing $\Delta\, log\, t = 0.175$; *wavelength:* covering the range 100-30,000 Å with resolution of 10 Å. Extensive testing confirms the adequacy of this griding for the problem at hand. Atomic line list data were taken from the Kurucz CD 23 line list (Kurucz & Bell 1995), which contains nearly 500,000 lines. 10^{10} photon packets were used for the calculation, which allowed for acceptable signal-to-noise in the synthetic broadband light curves, spectra, and velocity-dependent specific intensity profiles.

4.B Derivation of Equation 9

The observed monochromatic flux density F_λ of a source is obtained by setting up a small element of area dA perpendicular to the line of sight at the location of the observer, and integrating the specific intensity of the field I_λ in the direction normal to dA over the solid angle subtended by the source (Rybicki & Lightman 1979),

$$F_\lambda = \int I_\lambda \cos\theta d\Omega. \tag{4.15}$$

In Equation 4.15, θ is defined by $\tan\theta = P/D_L$, where D_L is the luminosity distance from the observer to the closest point on the plane.[12] From this definition we can construct the radial differential dP,

$$dP = D_L \sec^2\theta\, d\theta. \tag{4.16}$$

Using $d\Omega \equiv \sin\theta\, d\theta\, d\phi$, Equation 4.15 becomes

$$F_\lambda = \int_0^{2\pi} \int_0^{\theta_m} I_\lambda \cos\theta \sin\theta\, d\theta\, d\phi, \tag{4.17}$$

where θ_m is the maximum angular extent of the atmosphere. Making the change of variables shown in Equation 4.16, and using $\cos\theta = D_L/\sqrt{P^2 + D_L^2}$ and $\sin\theta = P/\sqrt{P^2 + D_L^2}$, Equation 4.17 becomes

$$F_\lambda = \int_0^{2\pi} \int_0^{P_m} \frac{P D_L^2 I_\lambda}{(P^2 + D_L^2)^2}\, dP\, d\phi. \tag{4.18}$$

As we are in the $P \ll D_L$ limit, by Taylor expanding the denominator of the integrand of Equation 4.18 in powers of (P/D_L) and keeping only first order terms, Equation 4.18 reduces to

$$F_\lambda = D_L^{-2} \int_0^{2\pi} \int_0^{P_m} I_\lambda\, P\, dP\, d\phi. \tag{4.19}$$

Since lensing conserves surface brightness, the application of a spatially varying microlensing magnification pattern transforms $I_\lambda \rightarrow \mu(P,\phi) I_\lambda(P,\phi)$. Making this substitution in equation 4.19, we are left with Equation 4.9. A schematic of the integration geometry is presented in Figure 4.B.1.

[12] The luminosity distance (not the angular diameter distance) is used here because the intrinsic luminosity of the source is known.

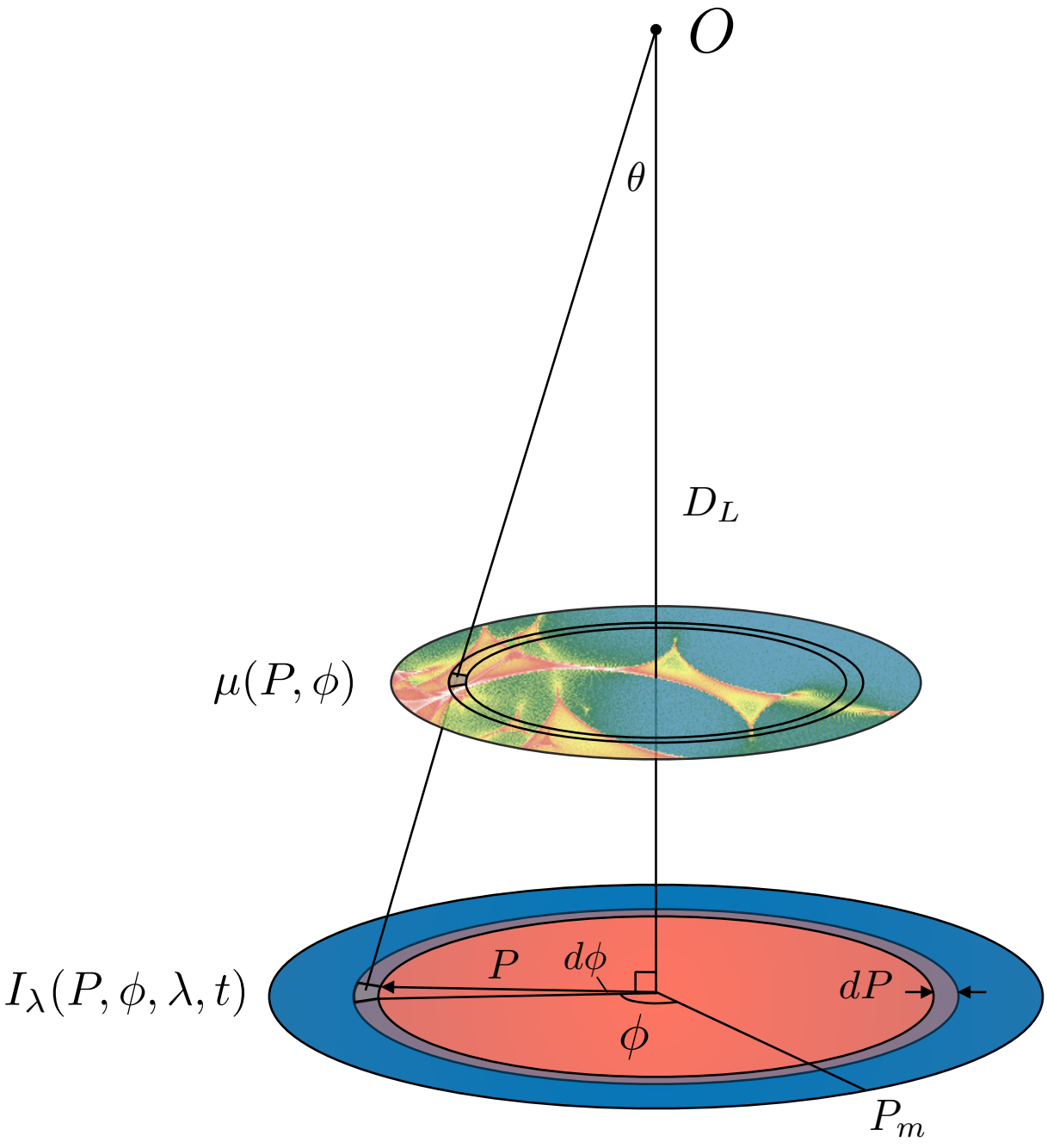

Figure 4.B.1: Integration geometry for Appendix 4.B.

Acknowledgments

DAG gratefully acknowledges Eric Linder for a careful reading of the manuscript and for thoughtful feedback. Greg Aldering and Alex Kim also deserve thanks for feedback that improved the paper. DAG, TEC, and PEN are members of the Large Synoptic Survey Telescope Dark Energy Science Collaboration (LSST-DESC), and they acknowledge Phil Marshall and the Strong Lensing working group for bringing them together so that this work could be launched. DAG thanks Kyle Barbary for leading the development of `sncosmo` (Barbary et al. 2016), which was essential to the analysis. The authors acknowledge support from the DOE under grant DE-AC02-05CH11231, Analytical Modeling for Extreme-Scale Computing Environments. This research used resources of the National Energy Research Scientific Computing Center, a DOE Office of Science User Facility supported by the Office of Science of the U.S. Department of Energy under Contract No. DE-AC02-05CH11231 as well as the `savio` cluster at UC Berkeley. Figures 4.2, 4.9, and 4.11 were rendered with code based on `ChainConsumer` (Hinton 2016). This research has made use of NASA's Astrophysics Data System. This research made use of Astropy, a community-developed core Python package for Astronomy (Astropy Collaboration et al. 2013).

Chapter 5

Evidence for Sub-Chandrasekhar Mass Type Ia Supernovae from an Extensive Survey of Radiative Transfer Models

An earlier version of this chapter was previously published as Goldstein, D. A., & Kasen, D. 2018, ApJ, 852, L33.

Abstract

There are two classes of viable progenitors for normal Type Ia supernovae (SNe Ia): systems in which a white dwarf explodes at the Chandrasekhar mass ($M_{\rm ch}$), and systems in which a white dwarf explodes below the Chandrasekhar mass (sub-$M_{\rm ch}$). It is not clear which of these channels is dominant; observations and light curve modeling have provided evidence for both. Here we use an extensive grid of 4,500 time-dependent, multiwavelength radiation transport simulations to show that the sub-$M_{\rm ch}$ model can reproduce the entirety of the width-luminosity relation (WLR), while the $M_{\rm ch}$ model can only produce the brighter events ($0.8 < \Delta M_{15}(B) < 1.55$), implying that fast-declining SNe Ia come from sub-$M_{\rm ch}$ explosions. We do not assume a particular theoretical paradigm for the progenitor or explosion mechanism, but instead construct parameterized models that vary the mass, kinetic energy, and compositional structure of the ejecta, thereby realizing a broad range of possible outcomes of white dwarf explosions. We provide fitting functions based on our large grid of detailed simulations that map observable properties of SNe Ia such as peak brightness and light curve width to physical parameters such as ^{56}Ni and total ejected mass. These can be used to estimate the physical properties of observed SNe Ia.

5.1 Introduction

Type Ia supernovae (SNe Ia) play a crucial role in astrophysics: they contribute to the chemical enrichment of galaxies, represent a key endpoint of stellar evolution, and continue to provide precise distances that enable the study of dark energy. Yet we know surprisingly little about their origins. Several lines of observational evidence, including early observations of the nearby SN Ia 2011fe (Nugent et al. 2011), indicate that the events result from the runaway thermonuclear explosion of at least one accreting carbon-oxygen (C/O) stellar core in a binary system (Hillebrandt & Niemeyer 2000; Maoz et al. 2014), most likely a white dwarf (WD; Bloom et al. 2012). But several viable theories exist for the nature and mass of the donor star, the triggering mechanism of the explosion, and the process by which thermonuclear burning propagates through the WD.

Potential progenitors of normal SNe Ia can be roughly divided into two categories (see Wang & Han 2012 or Maoz et al. 2014 for recent reviews): systems that produce an explosion near the Chandrasekhar mass, the maximum mass of a stable, non-rotating WD ($M_{\rm ch} \approx 1.4\,M_{\odot}$), and systems that produce an explosion below the Chandrasekhar mass (sub-$M_{\rm ch}$). In the classic $M_{\rm ch}$ scenario (Whelan & Iben 1973), a C/O WD accretes mass from a non-degenerate donor, usually a main sequence star or a red giant, until it approaches $M_{\rm ch}$ and centrally ignites.

A main alternative to the classic $M_{\rm ch}$ channel is the sub-$M_{\rm ch}$ double-detonation scenario, in which accreted helium on the surface of a WD in a close binary detonates before the star nears $M_{\rm ch}$, launching a shock wave that travels inward to detonate the C/O (Taam 1980; Nomoto 1982; Woosley & Weaver 1994; Shen & Bildsten 2009; Fink et al. 2010). Double-detonations can be either single-degenerate (if the donor is a non-degenerate helium star; Livne 1990) or double-degenerate (if the donor is another WD; Bildsten et al. 2007; Guillochon et al. 2010).

For many years, the classic $M_{\rm ch}$ scenario was favored as the dominant SN Ia progenitor channel (e.g., Hillebrandt & Niemeyer 2000; Woosley et al. 2007). But recently, independent lines of evidence that disfavor this scenario as the singular path to SNe Ia have emerged. Gilfanov & Bogdán (2010) showed that the X-ray fluxes of nearby galaxies are too low for classic $M_{\rm ch}$ progenitors, which are X-ray bright, to account for the observed SN Ia rate. Sim et al. (2010) and Woosley & Kasen (2011) showed that sub-$M_{\rm ch}$ models can reproduce the observed properties of SNe Ia and the basic light curve width-luminosity relation (WLR; Phillips 1993). Scalzo et al. (2014a,b) used the gray formalisms of Arnett (1982) and Jeffery (1999) to infer the masses of SNe Ia from their bolometric light curves, finding evidence for a significant rate of sub-$M_{\rm ch}$ events. Recent evidence against the classic $M_{\rm ch}$ scenario includes the lack of observed surviving companions in nearby SN Ia remnants (Shappee et al. 2013), the low metallicities of nearby galaxies (McWilliam et al. 2017), the correlation between SN Ia luminosity and stellar population age (Shen et al. 2017b), the lack of observed emission from stripped companion material (Shappee et al. 2016; Botyanszki et al. 2017) and simulations of spectrum synthesis for small sets of sub-$M_{\rm ch}$ explosion models (Blondin et al. 2017a,b; Shen et al. 2017a), which suggest sub-$M_{\rm ch}$ events may be required to explain fast-declining SNe Ia.

In this article, we present detailed radiation transport simulations of a broad grid of 4,500

parametrized, one-dimensional (1D) supernova ejecta models. The models are designed to capture the essential degrees of freedom in SN Ia spectrum synthesis without assuming a particular theoretical paradigm for the progenitor or explosion mechanism. Our broad model survey suggests that fast-declining SNe Ia must have sub-$M_{\rm ch}$ progenitors. This implies that the classic $M_{\rm ch}$ scenario cannot explain all SNe Ia.

5.2 A Simple Model for The Ejecta

The starting point for our simulations is a model describing the composition, density, and temperature of the debris produced by the thermonuclear explosion of a C/O WD. We assume that the explosion completely unbinds the star, and that the process of nuclear burning fuses part of the C/O into heavier elements. The nuclear energy released by burning, the internal and gravitational binding energies of the exploding WD, and other progenitor-specific terms that we do not model explicitly here (e.g., WD rotation; Yoon & Langer 2005) control the final kinetic energy of the ejecta, which expands and reaches homology minutes after the explosion. The ejecta is assumed to be spherically symmetric, consistent with spectropolarimetric observations that show that global asymmetries in SNe Ia are minor (Wang & Wheeler 2008b).

We write the kinetic energy E_K of the ejecta as $E_K = \frac{1}{2} M_{\rm Ej} v_K^2$, where $M_{\rm Ej}$ is the total ejected mass and v_K is the kinetic energy velocity, both free parameters of the model. We let both $M_{\rm Ej}$ and v_K float independently to implicitly capture progenitor-specific contributions to the kinetic energy; thus the kinetic energies of our models span a broader range than what would be obtained by summing the contributions of nuclear burning, internal energy, and gravitational binding energy alone.

We adopt an exponentially decaying density profile

$$\rho(v,t) = \rho_0 \left(\frac{t_0}{t}\right)^3 e^{-v/v_e}, \tag{5.1}$$

where v_e is the characteristic e-folding velocity of the atmosphere, given by

$$v_e = \sqrt{\frac{E_K}{6 M_{\rm Ej}}} = \frac{v_K}{\sqrt{12}}. \tag{5.2}$$

This profile has provided a good fit to the results of many explosion simulations (Woosley et al. 2007), but it has been known to overpredict the central densities of the ejecta of sub-$M_{\rm ch}$ explosions (Shen et al. 2017a). In Section 5.5, we study the effects of a less centrally concentrated density profile.

In a detailed calculation, the structure of the exploding object, the location of its ignition point(s), its explosion mechanism, and its explosive dynamics would determine the products of nuclear burning and their distribution in the ejecta. In the spirit of Woosley et al. (2007), we do not model these processes directly in our study; instead, we parametrize the nucleosynthetic yields of burning. Spectral time series of SNe Ia indicate that the ejecta are compositionally

stratified, with heavier elements located in the inner layers (e.g., Pereira et al. 2013b). In models, such an abundance layering results from burning at higher densities producing heavier elements. The interior ejecta consists primarily of ^{56}Ni and stable iron group elements (IGEs), the latter produced by electron capture or the neutron excess from metallicity. The exterior layers consist of intermediate mass elements (IMEs) and possibly unburned C/O.

Accordingly, our model possesses three layers: a ^{56}Ni+IGE layer (95% ^{56}Ni, 5% ^{54}Fe by mass), an IME layer, and an unburned C/O layer (50% C, 50% O by mass). For the IME layer, we base our abundances on the detailed nucleosynthesis calculations of Shen et al. (2017a), adopting the following mass fractions: ^{20}Ne: 4.486×10^{-8}, ^{24}Mg: 1.294×10^{-5}, ^{28}Si: 5.299×10^{-1}, ^{32}S: 3.303×10^{-1}, ^{36}Ar: 6.986×10^{-2}, ^{40}Ca: 6.834×10^{-2}, ^{44}Ti: 5.268×10^{-5}, ^{48}Cr: 1.479×10^{-3}. The masses of these layers are free parameters of the model, which we write as $f_{\rm Ni}$, the fraction of the ejecta mass in the ^{56}Ni+IGE layer, and $f_{\rm CO}$, the fraction of the ejecta mass in the C/O layer. The mass of the IME layer can be derived from the model parameters as $M_{\rm IME} = M_{\rm Ej}(1 - f_{\rm Ni} - f_{\rm CO})$.

There are a variety of mechanisms by which the abundances of elements in the ejecta can become smeared-out in velocity space (henceforth "mixing"). Our model includes a mixing parameter m, a dimensionless real number that is related to $N_{\rm mix}$, the integer number of times to run a boxcar average of window size 0.02 $M_\odot$ over the ejecta in Lagrangian space, via $N_{\rm mix} = {\rm floor}(10^m)$. In our scheme this parameter accomplishes the mixing of ^{56}Ni and other species into the inner and outer regions of the atmosphere.

We generated a grid of 4,500 SN Ia ejecta structures using the above scheme, each of which is fully specified by the five parameters listed in Table 5.1. We drew the parameters of each model at random from independent uniform distributions over the ranges specified in Table 5.1, except for $M_{\rm Ej}$, which was drawn from a broken uniform distribution. 95% of the models had $0.7 \leq M_{\rm Ej}/M_\odot < 1.6$, and the remaining 5% had $1.6 \leq M_{\rm Ej}/M_\odot \leq 2.5$. All models in the grid were generated with the `simple` supernova atmosphere generator (Goldstein 2016).

5.3 Radiation Transport Simulations

We used the time-dependent multi-wavelength Monte Carlo radiation transport code `SEDONA` (Kasen et al. 2006) to calculate light curves and spectra of the models. Given a homologously expanding supernova ejecta structure, `SEDONA` calculates the full time series of emergent spectra. Broadband light curves can be constructed by convolving the synthetic spectrum at each time with the appropriate filter transmission functions. `SEDONA` includes a detailed treatment of gamma-ray transfer throughout the atmosphere to determine the instantaneous energy deposition rate from radioactive ^{56}Ni and ^{56}Co decay (for a detailed description of the gamma-ray transport, see Kasen et al. 2006, Appendix A). Other decay chains that can change the composition of trace isotopes, such as ^{48}Cr $\rightarrow^{48}$ V $\rightarrow^{48}$ Ti, are not treated in the present calculations. Radiative heating and cooling rates are evaluated from Monte Carlo estimators, with the temperature structure of the ejecta assumed to be in radiative equilibrium. See Kasen et al. (2006) and Roth & Kasen (2015) for detailed code

Table 5.1: Model Parameters and Assumptions

Parameter	Range
$M_{\rm Ej}$	0.7 – 2.5 $M_\odot$
v_K	8,000 – 15,000 km s^{-1}
$f_{\rm Ni}$	0.1 – 0.8
$f_{\rm CO}$	0.00 – 0.07
m	1.0 – 2.5
Assumptions and Justifications	
Spherically symmetric ejecta (spectropolarimetry)	
Object that explodes is a C/O WD (2011fe)	
Decaying exponential density profile (explosion simulations)	
Ejecta are stratified in three layers (spectroscopy)	
Level populations assumed to be in LTE	
Light curve powered exclusively by ^{56}Ni decay chain	

descriptions and verifications.

Several significant approximations are made in our `SEDONA` simulations, notably the assumption of local thermodynamic equilibrium (LTE) in computing the atomic level populations. In addition, bound-bound line transitions are treated using the expansion opacity formalism (implying the Sobolev approximation; Jeffery 1995). In this formalism, the opacities of many spectral lines are represented in aggregate by a single effective opacity. Although the `SEDONA` code is capable of a direct Monte Carlo treatment of NLTE line processes, due to computational constraints this functionality is not exploited in the large parameter survey here.

We treat the line source function in the two-level equivalent atom approximation, where a parameter ϵ sets the ratio of absorptive opacity to total (i.e., absorptive plus scattering) opacity. Previous LTE studies of SNe Ia have found that using primarily absorptive lines ($\epsilon \approx 1$) reasonably captures the wavelength redistribution of photons. In complex atoms like the iron group species, redistribution via multiple fluorescence takes on an approximate thermal character (Pinto & Eastman 2000a,b; Blinnikov et al. 2006). For strong IME line features, however, using $\epsilon = 1$ typically over-estimates the line emission component; for example, Kasen (2006b) showed that using a purely absorptive line source function for calcium over-predicts the emission in the Ca II IR triplet features, which substantially influences the I-band light curve. We therefore assume that lines for all ions with $Z \leq 20$ are "purely scattering" ($\epsilon_{\rm th} = 0$) whereas lines from ions near the iron group are "purely absorptive" (i.e., $\epsilon_{\rm th} = 1$).

While the LTE approximation has been shown to produce a reasonable light curve predictions during the photospheric phases of SNe Ia (e.g., Jack et al. 2011) quantitative errors in the broadband magnitudes are expected on the order of 0.1 to 0.3 mag. For this

reason, our model peak magnitudes, colors and broadband (e.g., B-band) decline rates should be considered uncertain at this level. The adoption of an alternative value $\epsilon_{\rm th} \lesssim 1$ for the iron group lines shifts the location of the models in the WLR and color plots discussed below. In particular, choosing $\epsilon \lesssim 1$ leads to slower B-band light curve decline rates, but does not significantly change the slope of the model relation or the level of dispersion. On the other hand, if $\epsilon_{\rm th}$ depends in a systematic way on temperature or density, this could lead to correlated errors that affect the slope of the model relation.

The two-level atom framework applied here is just one of several uncertainties that affect the radiative transfer calculations. In addition, inaccuracy or incompleteness in the atomic line data can be a source of significant error. The inaccuracy of the LTE ionization assumption may also have significant consequences for the B-band light curves (Kasen et al. 2006). At later times ($\gtrsim$ 30 days after B-band maximum) the NLTE effects become increasingly significant and the model calculations become unreliable.

The numerical gridding in the present calculations was as follows: *spatial:* 100 equally spaced radial zones with a maximum velocity of 4×10^4 km s^{-1}; *temporal:* 116 time points beginning at day 1 and extending to day 100 with logarithmic spacing $\Delta \log t = 0.1$ and a maximum time step of 1 day; *wavelength:* covering the range 150 – 60,000 Å with resolution $\Delta \log \lambda = 0.001$. Atomic line list data were taken from the Kurucz CD 1 line list (Kurucz & Bell 1995), which contains about 42 million lines. A total of $\sim 2.3 \times 10^7$ photon packets was used for each calculation, which allowed for acceptable signal-to-noise in the synthetic broadband light curves and spectra.

5.4 Results

Figure 5.1 shows the distribution of our models in $\Delta M_{15}(B)$ v. M_B space, color coded by $M_{\rm Ej}$, with magnitudes given in the Vega system. The WLR of Phillips et al. (1999) is overplotted as a red box. The models span the space of SNe Ia and beyond, including the sub-luminous 91bg and over-luminous 91T-like events, as well as many more unusual events that fall far from WLR and may have never been observed. As discussed in Woosley et al. (2007), this implies that Nature does not realize all conceivable ejecta structures, rather the existence of a WLR implies that the explosion physics of SNe Ia must correlate the ejecta parameters in a systematic way.

By eye, it is clear that the entire model set shows a strong trend between $\Delta M_{15}(B)$, M_B, and $M_{\rm Ej}$. Models with faster B-band decline rates have lower overall ejecta mass. Only models with $M < M_{\rm ch}$ can reproduce the fastest decline rates, $\Delta M_{15}(B) > 1.55$. The sub-$M_{\rm ch}$ models can reproduce the full extent of the WLR ($0.8 < \Delta M_{15}(B) < 2.0$), whereas $M_{\rm ch}$ models can only reproduce the bright end ($0.8 < \Delta M_{15}(B) < 1.55$). Inclusion of NLTE effects (e.g., Blondin et al. 2013; Dessart et al. 2014) is necessary to see if radiative transfer effects can change this conclusion, although previous SN Ia light curve calculations suggest that NLTE effects tend to systematically decrease $\Delta M_{15}(B)$ compared to LTE calculations (compare, e.g., Blondin et al. 2017b and Shen et al. 2017a).

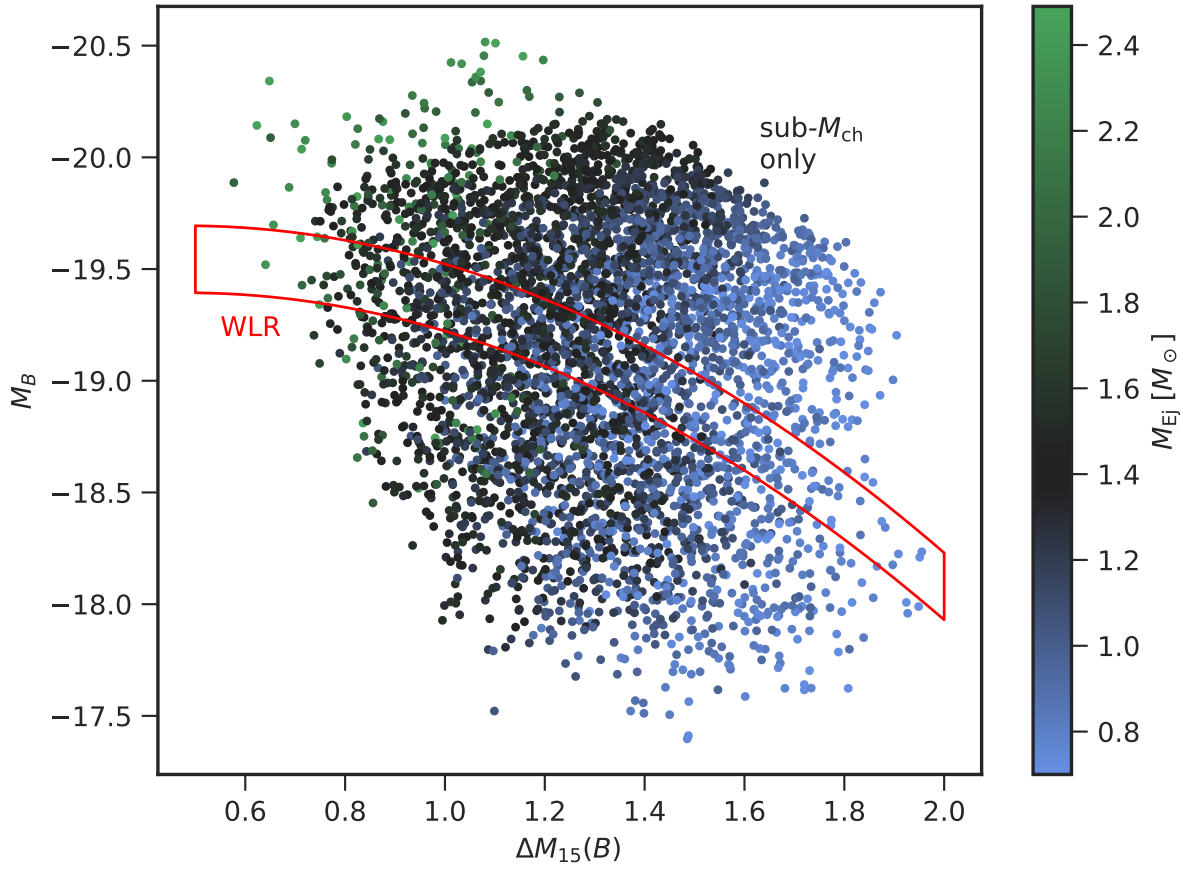

Figure 5.1: M_B versus $\Delta M_{15}(B)$ for our entire grid of 4,500 models. The relationship of Phillips et al. (1999) is overplotted as a red box. Models with $\Delta M_{15}(B) \geq 1.55$ are definitively sub-$M_{\rm ch}$. Both $M_{\rm ch}$, sub-$M_{\rm ch}$, and even some super-$M_{\rm ch}$ models are consistent with $0.8 < \Delta M_{15}(B) < 1.55$.

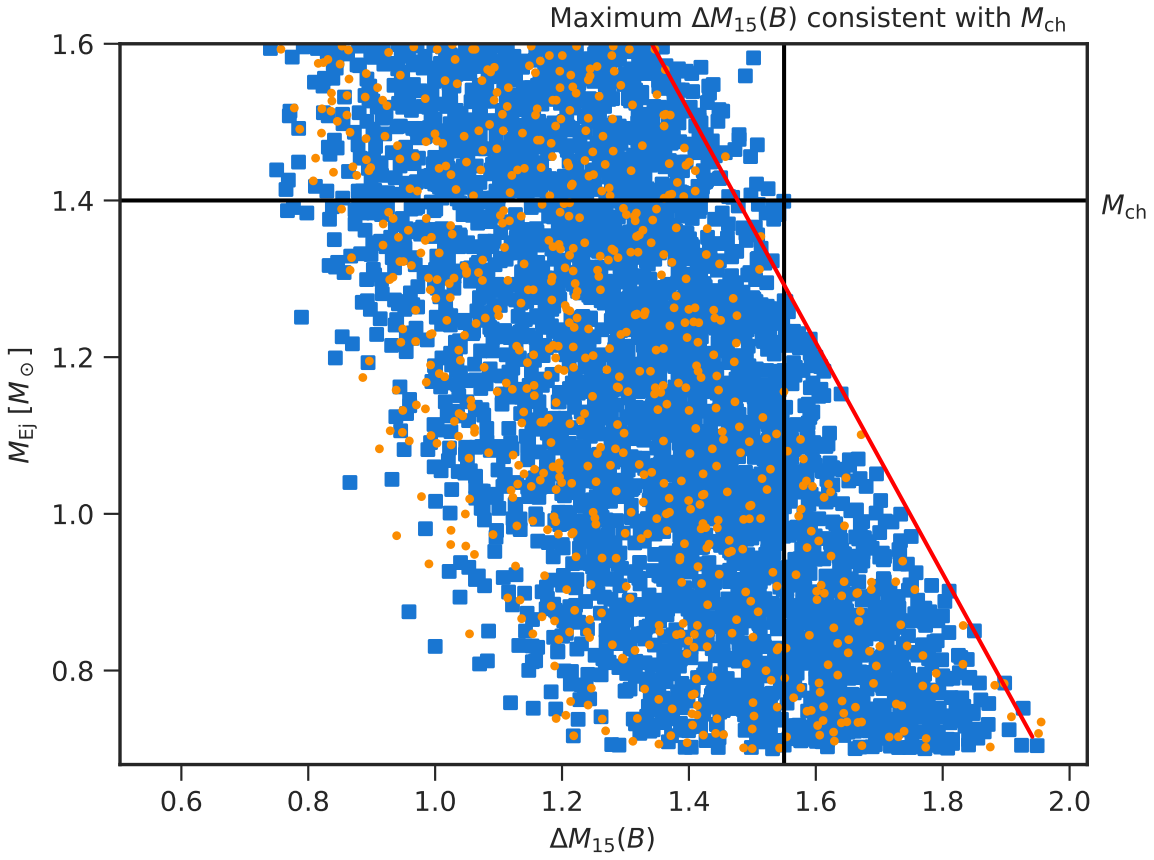

Figure 5.2: Correlation between $M_{\rm Ej}$ and $\Delta M_{15}(B)$ for models off the WLR (blue squares) and on the WLR (orange dots). In both cases, models with $\Delta M_{15}(B) > 1.55$ cannot be explained by $M_{\rm ch}$ progenitors. Many observed SNe Ia satisfy this criterion. A linear fit to the maximum ejected mass as a function of $\Delta M_{15}(B)$ is shown as a red line.

Figure 5.2 shows the correlation between $\Delta M_{15}(B)$ and $M_{\rm Ej}$ for models on and off the WLR (for clarity, super-$M_{\rm ch}$ models have been excluded from the Figure). At $\Delta M_{15}(B) = 1.55$, models on the grid cease to be consistent with $M_{\rm ch}$. Many known SNe Ia have $\Delta M_{15}(B) > 1.55$; for an in-depth study of supernovae of this class see Taubenberger et al. (2008). We conclude that sub-$M_{\rm ch}$ progenitors constitute at least some and potentially the bulk of observed of SNe Ia.

Evidence for sub-$M_{\rm ch}$ SNe Ia has previously been derived from empirical analyses of pseudobolometric SN Ia light curves (Stritzinger et al. 2006; Scalzo et al. 2014a,b; Dhawan et al. 2017; Wygoda et al. 2017). Heringer et al. (2017), using LTE spectrum synthesis calculations, found that a common explosion mechanism can account for both sub-luminous and normal SNe Ia. Our work suggests that this common mechanism is likely sub-$M_{\rm ch}$.

Blondin et al. (2017b), using NLTE light curve calculations for a set of 12 detonation models similarly found that only sub-$M_{\rm ch}$ models could reproduce the fast-declining light curves. Our extensive model survey indicates that this conclusion is robust and holds over a much more general model parameter space that is not tied to a particular explosion scenario.

Interestingly, we note that super-luminous SNe Ia such as SN 2003fg, SN 2006gz, SN 2007if, and SN 2009dc, all fall squarely in the super-$M_{\rm ch}$ zone of Figure 5.1 (Scalzo et al. 2010), suggesting that such events do indeed require super-$M_{\rm ch}$ ejecta, unless they are not spherically symmetric, or an additional source of luminosity (e.g., interaction) contributes to the brightness (Maeda et al. 2010; Silverman et al. 2013).

5.4.1 Light Curves and Empirical Fitting Functions

To make the results of our large simulation grid useful to observers, we provide simple fitting functions that map empirical properties of SNe Ia to physical parameters of our models. Figure 5.3 shows the $UBVRI$ light curves of the models that lie along the WLR of Figure 5.1, color-coded by $M_{^{56}\rm Ni}$. These light curves exhibit the characteristic broadband evolution of SNe Ia, validating the model parametrization described in Section 5.2. The over-luminous secondary maximum in R and I bands is a well-known issue related to the assumptions in the transfer (see Section 5.3). The light curves show a strong correlation between $M_{^{56}\rm Ni}$ and peak brightness in all bands; this is illustrated in Figure 5.4. The relations are quadratic and given in the Appendix.

Figure 5.2 shows that there is a linear relationship between $\Delta M_{15}(B)$ and the maximum ejected mass of an SN Ia. We fit a linear relationship to the data in the Figure, where it is displayed as a red line. We report the equation describing the relationship in the Appendix. We did not find a significant correlation between the mixing parameter m and the observable properties of the models. Goldstein & Kasen (in preparation) will present a more thorough analysis of the entire model set, and release it to the public.

5.5 Discussion

Although our model space is broad, it is not exhaustive—we have imposed physical constraints that limit certain models from the grid. One potentially important example is that, unlike some previous 1D investigations, we have not considered models with large cores of stable iron group elements. Such cores can help increase the decline rates of models by moving the ^{56}Ni closer to the surface, reducing the diffusion time and providing lines that blanket the B-band over time.

We do not include a large central core of stable IGEs in our models for two reasons. First, such cores appear to be the result of artificial burning fronts prescribed in parameterized 1D delayed-detonation models. In more realistic three-dimensional simulations, the deflagration phase produces buoyant plumes that smear out the compositional structures of the central regions, leaving no stable core (e.g., Seitenzahl et al. 2013). Other models of SNe Ia (e.g.,

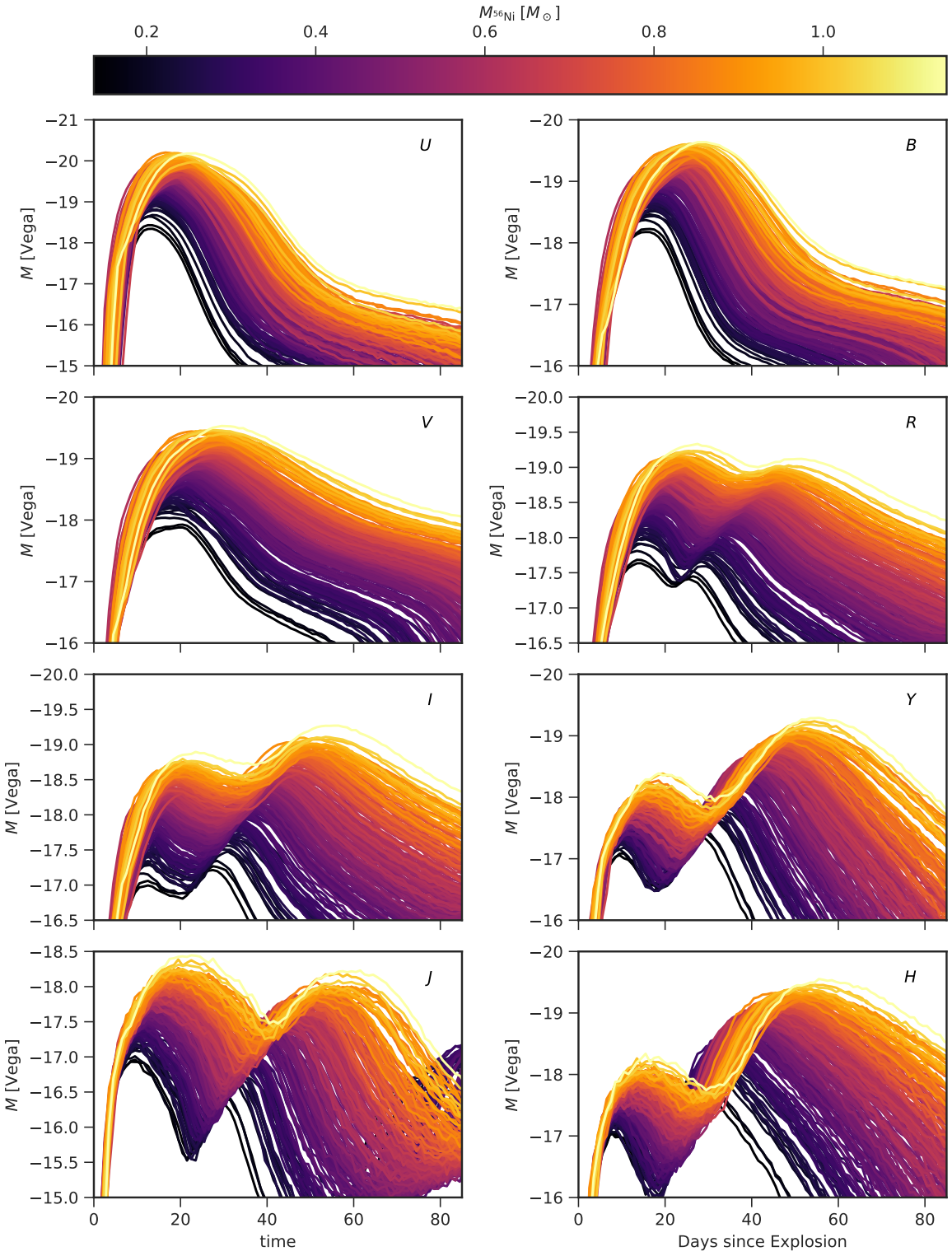

Figure 5.3: `SEDONA` light curves for the models that lie along the WLR (red boxed region in Figure 5.1), color-coded by $M_{^{56}\mathrm{Ni}}$. There is a strong correlation between light curve shape and $M_{^{56}\mathrm{Ni}}$ in all bands.

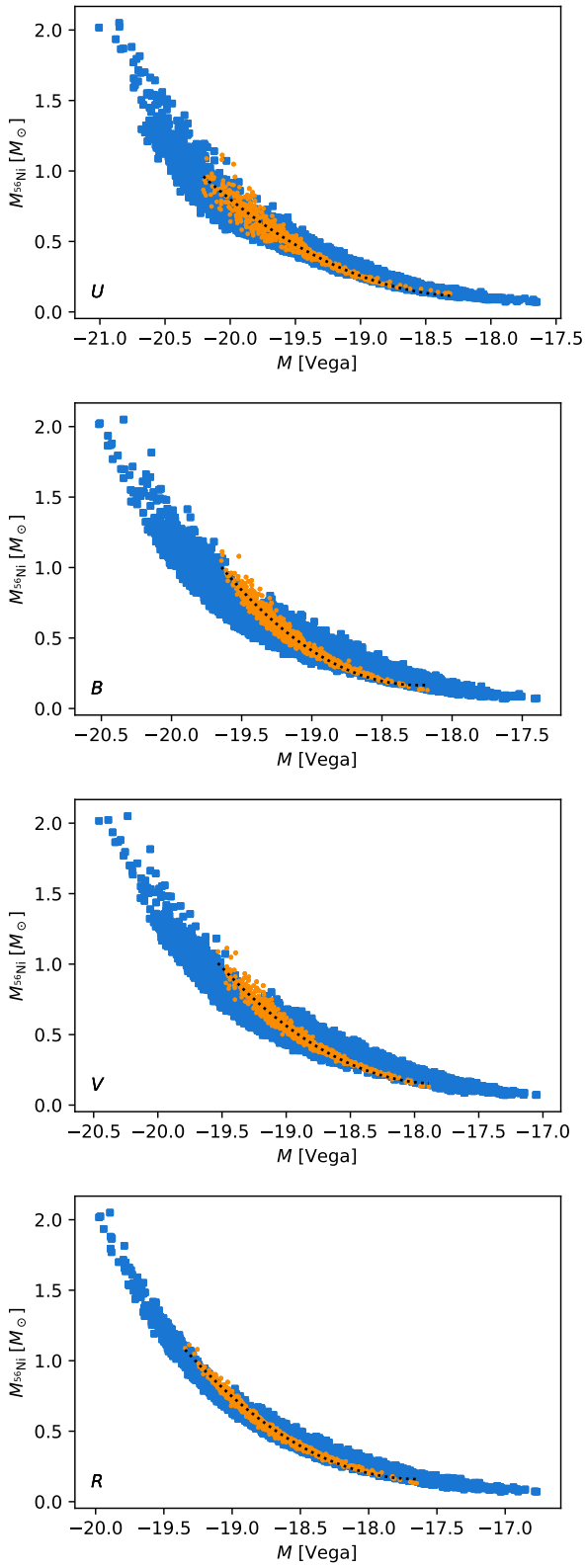

Figure 5.4: Correlation between $M_{^{56}\mathrm{Ni}}$ and peak brightness for models off the WLR (blue squares) and on the WLR (orange dots). The quadratic fitting functions in Equations 5.8 – 5.11 are plotted as black dashed lines in each panel.

sub-$M_{\rm ch}$ double detonations, violent WD mergers, WD collisions) likewise do not produce a stable iron core.

Second, NLTE calculations show that a large core of stable iron produces nebular line profiles that disagree with observations—notably a flat top to the [Co III] feature at 5888Å (Botyánszki & Kasen 2017). Observations of flat-topped profiles of Co lines in near-IR spectra of SN 2003du had been the main observational evidence given by Höflich et al. (2004) for the necessity of a stable iron core in models. However, the signal to noise ratio of the nebular spectrum of SN 2003du was low, and more recent samples of high signal-to-noise SN Ia nebular spectra have definitively exhibited rounded profiles (e.g., Maguire et al. in preparation).

Another potentially important effect is that we only consider exponential density profiles in our grid. Ejecta models with flat or slowly-declining central density profiles have smaller central densities for a given kinetic energy and mass than the exponential profiles used here, leading to shorter diffusion times and faster-evolving light curves. To determine if using a density profile with a flat inner region could enable our $M_{\rm ch}$ models to account for fast-declining SNe Ia, we selected 450 models (10%) at random from our grid and re-ran them using a broken power law density profile

$$\rho(v) \propto \begin{cases} (v/v_t)^{-\delta} & v < v_t \\ (v/v_t)^{-n} & v \geq v_t \end{cases}, \tag{5.3}$$

with a flat inner region ($\delta = 0$) and a steeply declining outer region ($n = 10$) instead of an exponential, with v_t set by E_K and $M_{\rm Ej}$ following Kasen (2010). We kept all other model parameters (mass, composition, mixing, and kinetic energy) the same.

We find that although flattening the inner density profile increases the decline rates of $M_{\rm ch}$ models, the models still cannot reproduce the fastest-declining SNe Ia. The exponential and broken power law models differ quantitatively by ∼0.2 mag in the $\Delta M_{15}(B)$ value at which they cease to be consistent with $M_{\rm ch}$ ($\Delta M_{15}(B) = 1.75$ for the broken power law models versus $\Delta M_{15}(B) = 1.55$ for the exponential models). But the power law $M_{\rm ch}$ models that have relatively fast decline rates ($\Delta M_{15}(B) > 1.6$) require unrealistically high kinetic energies (2×10^{51} erg $< E_K < 3 \times 10^{51}$ erg) and ^{56}Ni yields ($M_{^{56}\rm Ni} > 1 M_\odot$). Thus, although some $M_{\rm ch}$ power law models can get close to fast-declining SNe Ia, they can only do so with extreme parameters that cause other problems, suggesting that such models are unlikely.

Our main results are in conflict with those of Hoeflich et al. (2017), who make the case that with the appropriate choice of parameters they can account for the photometric behavior of both typical SNe Ia and 91bg-like events using $M_{\rm ch}$ delayed-detonation models. An important factor that likely allows Hoeflich et al. (2017) to achieve fast declining $M_{\rm ch}$ models is that their low ^{56}Ni models have a large amount (0.2 – 0.3 $M_\odot$) of stable iron at the very center. We note that the results of Hoeflich et al. (2017) are in significant tension with the results of Blondin et al. (2017b). Running similar low-^{56}Ni $M_{\rm ch}$ ejecta structures (DDC25 and 08) through NLTE radiation transport, Hoeflich et al. (2017) obtain $\Delta M_{15}(B)$ values that are larger than those of Blondin et al. (2017b) by almost 1 mag. While resolving this discrepancy

is outside the scope of the present paper, we note that the 3D calculations of Sim et al. (2013) also suggest that $M_{\rm ch}$ models with low ^{56}Ni yields do not have fast decline rates.

5.6 Conclusion

In this work we have used an extensive suite of 4,500 detailed radiation transport simulations to show that fast-declining SNe Ia come from sub-$M_{\rm ch}$ progenitor systems. We find that sub-$M_{\rm ch}$ and $M_{\rm ch}$ SNe Ia can reproduce the bright end of the WLR ($0.8 < \Delta M_{15}(B) < 1.55$), whereas only sub-$M_{\rm ch}$ SNe Ia can reproduce the faint end ($\Delta M_{15}(B) > 1.55$). In the era of big data, systematic parameter studies such as the one presented here will be useful for understanding the physics of transients. In future papers, we will use this technique to further illuminate the nature of SNe Ia, and we will expand the grid to further test the consistency of $M_{\rm ch}$ models with SN Ia light curves and spectra.

Appendix

5.A Functions Relating Physical Parameters of SNe Ia to Observable Quantities

The following functions can be used to estimate the ^{56}Ni mass of an SN Ia given its absolute magnitude in the rest-frame U, B, V or R bands (Vega system). The first set of functions gives a lower bound on the ^{56}Ni mass, the second set gives a median, and the third set gives an upper bound. The functions are second-degree polynomial fits to the 2.5, 50, and 97.5th percentiles of magnitude-binned WLR (orange) points in Figure 5.4.

$$[M_{^{56}\mathrm{Ni}}/M_\odot]_{\mathrm{min}} = 0.16263M_U^2 + 5.89704M_U + 53.57331 \tag{5.4}$$
$$= 0.43270M_B^2 + 15.85282M_B + 145.37146 \tag{5.5}$$
$$= 0.27958M_V^2 + 9.98986M_V + 89.39890 \tag{5.6}$$
$$= 0.33515M_R^2 + 11.87870M_R + 105.42028 \tag{5.7}$$

$$[M_{^{56}\mathrm{Ni}}/M_\odot]_{\mathrm{med}} = 0.20054M_U^2 + 7.27769M_U + 66.13664 \tag{5.8}$$
$$= 0.42325M_B^2 + 15.43821M_B + 140.94416 \tag{5.9}$$
$$= 0.28458M_V^2 + 10.12929M_V + 90.28593 \tag{5.10}$$
$$= 0.31409M_R^2 + 11.07772M_R + 97.83555 \tag{5.11}$$

$$[M_{^{56}\mathrm{Ni}}/M_\odot]_{\mathrm{max}} = 0.25592M_U^2 + 9.32807M_U + 85.11384 \tag{5.12}$$
$$= 0.40649M_B^2 + 14.71865M_B + 133.37570 \tag{5.13}$$
$$= 0.30942M_V^2 + 10.98176M_V + 97.57820 \tag{5.14}$$
$$= 0.29679M_R^2 + 10.41115M_R + 91.45071 \tag{5.15}$$

The following function gives the maximum ejected mass of an SN Ia in terms of $\Delta M_{15}(B)$. It is a fit to the upper boundary of the blue points in Figure 5.2, where it is shown as a red line.

$$M_{\mathrm{Ej,max}} = -1.47\Delta M_{15}(B) + 3.57 \tag{5.16}$$

Acknowledgments

DAG gratefully recognizes Rollin Thomas for years of guidance and mentorship—they were essential to this work. Ken Shen deserves thanks for sharing the results of his nucleosynthesis calculations and Peter Nugent for useful discussions. The authors acknowledge an anonymous referee for comments that improved the paper. This work was supported in part by the U.S. Department of Energy, Office of Science, Office of Nuclear Physics, under contract number DE-AC02-05CH11231 and DE-SC0017616, and by a SciDAC award DE-SC0018297. DK acknowledges support from the Gordon and Betty Moore Foundation through Grant GBMF5076. This research used resources of the National Energy Research Scientific Computing Center, a DOE Office of Science User Facility supported by the Office of Science of the U.S. Department of Energy under Contract No. DE-AC02-05CH11231. This research made use of NASA's Astrophysics Data System.

Chapter 6

Conclusion

This thesis presented solutions to some problems associated with using strongly gravitationally lensed supernovae (gLSNe) to measure the cosmological parameters. Chief among these were new methods for finding gLSNe and extracting their time delays in the presence of microlensing. The latter of these results involved performing simulations of radiation transport in supernova atmospheres. These simulations provided evidence that some Type Ia supernovae come from sub-Chandrasekhar mass progenitors.

I described an algorithm for identifying point-source transients and moving objects on reference-subtracted optical images containing artifacts of processing and instrumentation. The algorithm made use of the supervised machine learning technique known as Random Forest. I presented results from its use in the Dark Energy Survey Supernova program (DES-SN), where it was trained using a sample of 898,963 signal and background events generated by the transient detection pipeline. After reprocessing the data collected during the first DES-SN observing season (Sep. 2013 through Feb. 2014) using the algorithm, the number of transient candidates eligible for human scanning decreased by a factor of 13.4, while only 1.0 percent of the artificial Type Ia supernovae (SNe) injected into search images to monitor survey efficiency were lost, most of which were very faint events. I characterized the algorithm's performance in detail, and I discussed how it can inform pipeline design decisions for future time-domain imaging surveys, such as the Large Synoptic Survey Telescope and the Zwicky Transient Facility.

I also presented a simple algorithm for identifying gravitationally lensed SN Ia candidates in cadenced, wide-field optical imaging surveys. The technique is to look for supernovae that appear to be hosted by elliptical galaxies, but that have absolute magnitudes implied by the apparent hosts' photometric redshifts that are far brighter than the absolute magnitudes of normal SNe Ia (the brightest type of supernovae found in elliptical galaxies). Importantly, this purely photometric method does not require the ability to resolve the lensed images for discovery. AGNs, the primary sources of contamination that affect the method, can be controlled using catalog cross-matches and color cuts. Highly magnified core-collapse SNe will also be discovered as a byproduct of the method. Using a Monte Carlo simulation, I forecast that LSST can discover up to 500 multiply imaged SNe Ia using this technique in a

10-year z-band search, more than an order of magnitude improvement over previous estimates (Oguri & Marshall 2010). I also predicted that ZTF should find up to 10 multiply imaged SNe Ia using this technique in a 3-year R-band search—despite the fact that this survey will not resolve a single system.

I quantified the effect of microlensing on the glSN Ia yield of the Large Synoptic Survey Telescope (LSST) and the effect of microlensing on the precision and accuracy of time delays that can be extracted from LSST glSNe Ia. Microlensing has a negligible effect on the LSST glSN Ia yield, but it can be increased by a factor of $\sim$2 to 930 systems using a novel photometric identification technique based on spectral template fitting. Crucially, the microlensing of glSNe Ia is achromatic until 3 rest-frame weeks after the explosion, making the early-time color curves microlensing-insensitive time delay indicators. By fitting simulated flux and color observations of microlensed glSNe Ia with their underlying, unlensed spectral templates, I forecast the distribution of absolute time delay error due to microlensing for LSST, which is unbiased at the sub-percent level and peaked at 1% for color curve observations in the achromatic phase, while for light curve observations it is comparable to state-of-the-art mass modeling uncertainties (4%). About 70% of LSST glSN Ia images should be discovered during the achromatic phase, indicating that microlensing time delay uncertainties can be minimized if prompt multicolor follow-up observations are obtained. Accounting for microlensing, the 1–2 day time delay on the recently discovered glSN Ia iPTF16geu can be measured to 40% precision, limiting its cosmological utility.

I used an extensive grid of 4,500 time-dependent, multiwavelength radiation transport simulations to show that the sub-$M_{\rm ch}$ model can reproduce the entirety of the width-luminosity relation (WLR), while the $M_{\rm ch}$ model can only produce the brighter events ($0.8 < \Delta M_{15}(B) < 1.55$), implying that fast-declining SNe Ia come from sub-$M_{\rm ch}$ explosions. I did not assume a particular theoretical paradigm for the progenitor or explosion mechanism, but instead construct parameterized models that vary the mass, kinetic energy, and compositional structure of the ejecta, thereby realizing a broad range of possible outcomes of white dwarf explosions. I provided fitting functions based on our large grid of detailed simulations that map observable properties of SNe Ia such as peak brightness and light curve width to physical parameters such as ^{56}Ni and total ejected mass. These can be used to estimate the physical properties of observed SNe Ia.

Due their effectiveness and ease of implementation, the techniques presented in this thesis will greatly increase the utility of gravitationally lensed SNe Ia as cosmological probes. As such, a renewed focus should be placed on their role in cosmological studies and how to maximize their scientific return.

Bibliography

Alard, C., & Lupton, R. H. 1998, ApJ, 503, 325

Albrecht, A., Bernstein, G., Cahn, R., et al. 2006, ArXiv Astrophysics e-prints, astro-ph/0609591

Aldering, G., Adam, G., Antilogus, P., et al. 2002, in Proc. SPIE, Vol. 4836, Survey and Other Telescope Technologies and Discoveries, ed. J. A. Tyson & S. Wolff, 61

Amanullah, R., Goobar, A., Clément, B., et al. 2011, ApJ, 742, L7

Arnett, W. D. 1982, ApJ, 253, 785

Astier, P., Guy, J., Regnault, N., et al. 2006, A&A, 447, 31

Astropy Collaboration, Robitaille, T. P., Tollerud, E. J., et al. 2013, A&A, 558, A33

Baade, W., & Zwicky, F. 1934, Proceedings of the National Academy of Science, 20, 254

Bagherpour, H., Branch, D., & Kantowski, R. 2006, ApJ, 638, 946

Bailey, S., Aragon, C., Romano, R., et al. 2007, ApJ, 665, 1246

Baltay, C., Rabinowitz, D., Andrews, P., et al. 2007, PASP, 119, 1278

Banerji, M., Lahav, O., Lintott, C. J., et al. 2010, MNRAS, 406, 342

Barbary, K., Barclay, T., Biswas, R., et al. 2016, SNCosmo: Python library for supernova cosmology, Astrophysics Source Code Library, ascl:1611.017

Bellm, E. 2014, in The Third Hot-wiring the Transient Universe Workshop, ed. P. R. Wozniak, M. J. Graham, A. A. Mahabal, & R. Seaman, 27

Bernal, J. L., Verde, L., & Riess, A. G. 2016, JCAP, 10, 019

Bernstein, J. P., Kessler, R., Kuhlmann, S., et al. 2012, ApJ, 753, 152

Bertin, E., & Arnouts, S. 1996, A&AS, 117, 393

Bezanson, R., van Dokkum, P. G., Franx, M., et al. 2011, ApJ, 737, L31

Bildsten, L., Shen, K. J., Weinberg, N. N., & Nelemans, G. 2007, ApJ, 662, L95

Blanc, G., Afonso, C., Alard, C., et al. 2004, A&A, 423, 881

Blandford, R. D., & Narayan, R. 1992, ARA&A, 30, 311

Blinnikov, S. I., Röpke, F. K., Sorokina, E. I., et al. 2006, A&A, 453, 229

Blondin, S., Dessart, L., & Hillier, D. J. 2017a, ArXiv e-prints, arXiv:1711.09107 [astro-ph.SR]

Blondin, S., Dessart, L., Hillier, D. J., & Khokhlov, A. M. 2013, MNRAS, 429, 2127

—. 2017b, MNRAS, 470, 157

Bloom, J. S., & Richards, J. W. 2012, Data Mining and Machine Learning in Time-Domain Discovery and Classification, ed. M. J. Way, J. D. Scargle, K. M. Ali, & A. N. Srivastava, 89

Bloom, J. S., Richards, J. W., Nugent, P. E., et al. 2012, PASP, 124, 1175
Bolton, A. S., Burles, S., Koopmans, L. V. E., et al. 2008, ApJ, 682, 964
Bolton, A. S., Burles, S., Schlegel, D. J., Eisenstein, D. J., & Brinkmann, J. 2004, AJ, 127, 1860
Bonvin, V., Tewes, M., Courbin, F., et al. 2016, A&A, 585, A88
Bonvin, V., Courbin, F., Suyu, S. H., et al. 2017, MNRAS, 465, 4914
Botyánszki, J., & Kasen, D. 2017, ApJ, 845, 176
Botyanszki, J., Kasen, D., & Plewa, T. 2017, ArXiv e-prints, arXiv:1712.03274 [astro-ph.SR]
Bouy, H., Bertin, E., Moraux, E., et al. 2013, A&A, 554, A101
Breiman, L. 2001, Machine Learning, 45, 5
Breiman, L., Friedman, J., Olshen, R., & Stone, C. 1984, Classification and Regression Trees (Monterey, California: Wadsworth)
Brescia, M., Cavuoti, S., & Longo, G. 2015, MNRAS, 450, 3893
Brink, H., Richards, J. W., Poznanski, D., et al. 2013, MNRAS, 435, 1047
Brownstein, J. R., Bolton, A. S., Schlegel, D. J., et al. 2012, ApJ, 744, 41
Chae, K.-H. 2003, MNRAS, 346, 746
—. 2007, ApJ, 658, L71
Chang, K., & Refsdal, S. 1979, Nature, 282, 561
Choi, Y.-Y., Park, C., & Vogeley, M. S. 2007, ApJ, 658, 884
Chornock, R., Berger, E., Rest, A., et al. 2013, ApJ, 767, 162
Collett, T. E., & Auger, M. W. 2014, MNRAS, 443, 969
Collett, T. E., & Cunnington, S. D. 2016, MNRAS, 462, 3255
Collett, T. E., Marshall, P. J., Auger, M. W., et al. 2013, MNRAS, 432, 679
Desai, S., Armstrong, R., Mohr, J. J., et al. 2012, ApJ, 757, 83
Dessart, L., Hillier, D. J., Blondin, S., & Khokhlov, A. 2014, MNRAS, 441, 3249
Dhawan, S., Leibundgut, B., Spyromilio, J., & Blondin, S. 2017, A&A, 602, A118
Di Valentino, E., Melchiorri, A., & Silk, J. 2016, Physics Letters B, 761, 242
Diehl, H. T., Abbott, T. M. C., Annis, J., et al. 2014, in Proc. SPIE, Vol. 9149, Observatory Operations: Strategies, Processes, and Systems V, 91490V
Diehl, T. 2012, Physics Procedia, 37, 1332 , proceedings of the 2nd International Conference on Technology and Instrumentation in Particle Physics (TIPP 2011)
Dobler, G., & Keeton, C. R. 2006a, ApJ, 653, 1391
—. 2006b, ApJ, 653, 1391
du Buisson, L., Sivanandam, N., Bassett, B. A., & Smith, M. 2015, MNRAS, 454, 2026
Efstathiou, G. 2014, MNRAS, 440, 1138
Einstein, A. 1915, Sitzungsberichte der Königlich Preußischen Akademie der Wissenschaften (Berlin), Seite 844-847.
Fassnacht, C. D., Koopmans, L. V. E., & Wong, K. C. 2011, MNRAS, 410, 2167
Filippenko, A. V., Li, W. D., Treffers, R. R., & Modjaz, M. 2001, in Astronomical Society of the Pacific Conference Series, Vol. 246, IAU Colloq. 183: Small Telescope Astronomy on Global Scales, ed. B. Paczynski, W.-P. Chen, & C. Lemme, 121
Fink, M., Röpke, F. K., Hillebrandt, W., et al. 2010, A&A, 514, A53

Flaugher, B. 2005, International Journal of Modern Physics A, 20, 3121
Flaugher, B. L., Abbott, T. M. C., Angstadt, R., et al. 2012, in Proc. SPIE, Vol. 8446, Ground-based and Airborne Instrumentation for Astronomy IV, 844611
Foreman-Mackey, D., Price-Whelan, A., Ryan, G., et al. 2014, triangle.py: triangle.py v0.1.1, Zenodo Software Release, 2014
Foxley-Marrable, M., Collett, T. E., Vernardos, G., Goldstein, D. A., & Bacon, D. 2018, ArXiv e-prints, arXiv:1802.07738
Freedman, W. L. 2017, Nature Astronomy, 1, 0121
Friedmann, A. 1922, Zeitschrift fur Physik, 10, 377
Frieman, J. A., Bassett, B., Becker, A., et al. 2008, AJ, 135, 338
Garnavich, P. M., Kirshner, R. P., Challis, P., et al. 1998, ApJ, 493, L53
Gehrels, N., Spergel, D., & WFIRST SDT Project. 2015, Journal of Physics Conference Series, 610, 012007
Gilfanov, M., & Bogdán, Á. 2010, Nature, 463, 924
Gini, C. 1921, Econ. J., 31, 124
Goldstein, D. 2016, dannygoldstein/simple
Goldstein, D. A., & Kasen, D. 2018, ApJ, 852, L33
Goldstein, D. A., & Nugent, P. E. 2017, ApJ, 834, L5
Goldstein, D. A., Nugent, P. E., Kasen, D. N., & Collett, T. E. 2018, ApJ, 855, 22
Goldstein, D. A., D'Andrea, C. B., Fischer, J. A., et al. 2015, AJ, 150, 82
Goobar, A., Amanullah, R., Kulkarni, S. R., et al. 2017, Science, 356, 291
Guillochon, J., Dan, M., Ramirez-Ruiz, E., & Rosswog, S. 2010, ApJ, 709, L64
Gupta, R. R., D'Andrea, C. B., Sako, M., et al. 2011, ApJ, 740, 92
Guy, J., Astier, P., Baumont, S., et al. 2007, A&A, 466, 11
Hamuy, M., Maza, J., Phillips, M. M., et al. 1993, AJ, 106, 2392
Hastie, T., Rosset, S., Zhu, J., & Zou, H. 2009, Statistics and its Interface, 2, 349
Heringer, E., van Kerkwijk, M. H., Sim, S. A., & Kerzendorf, W. E. 2017, ApJ, 846, 15
Hillebrandt, W., & Niemeyer, J. C. 2000, ARA&A, 38, 191
Hinton, S. 2016, JOSS, 1
Hoeflich, P., Hsiao, E. Y., Ashall, C., et al. 2017, ApJ, 846, 58
Höflich, P., Gerardy, C. L., Nomoto, K., et al. 2004, ApJ, 617, 1258
Holder, G. P., & Schechter, P. L. 2003, ApJ, 589, 688
Holz, D. E. 2001, ApJ, 556, L71
Hsiao, E. Y., Conley, A., Howell, D. A., et al. 2007, ApJ, 663, 1187
Hubble, E. 1929, Proceedings of the National Academy of Science, 15, 168
Ivezić, Ž., Connelly, A. J., VanderPlas, J. T., & Gray, A. 2014, Statistics, Data Mining, and Machine Learningin Astronomy
Jack, D., Hauschildt, P. H., & Baron, E. 2011, A&A, 528, A141
James, F., & Roos, M. 1975, Computer Physics Communications, 10, 343
Jeffery, D. J. 1995, A&A, 299, 770
—. 1999, ArXiv Astrophysics e-prints, astro-ph/9907015
Karpenka, N. V., Feroz, F., & Hobson, M. P. 2013, MNRAS, 429, 1278

Kasen, D. 2006a, ApJ, 649, 939
—. 2006b, ApJ, 649, 939
—. 2010, ApJ, 708, 1025
Kasen, D., Thomas, R. C., & Nugent, P. 2006, ApJ, 651, 366
Kasen, D., & Woosley, S. E. 2007, ApJ, 656, 661
Kayser, R., Refsdal, S., & Stabell, R. 1986, A&A, 166, 36
Keeton, C. R., Kochanek, C. S., & Seljak, U. 1997, ApJ, 482, 604
Kelly, P. L., Rodney, S. A., Treu, T., et al. 2015a, Science, 347, 1123
Kelly, P. L., Brammer, G., Selsing, J., et al. 2015b, ArXiv e-prints, arXiv:1512.09093
Kessler, R., Bernstein, J. P., Cinabro, D., et al. 2009, PASP, 121, 1028
Kim, A., Goobar, A., & Perlmutter, S. 1996, PASP, 108, 190
Kochanek, C. S. 1991, ApJ, 373, 354
Komatsu, E., Smith, K. M., Dunkley, J., et al. 2011, ApJS, 192, 18
Koopmans, L. V. E., Bolton, A., Treu, T., et al. 2009, ApJ, 703, L51
Kormann, R., Schneider, P., & Bartelmann, M. 1994, A&A, 284, 285
Kurucz, R. L., & Bell, B. 1995, Atomic line list
Li, W., Leaman, J., Chornock, R., et al. 2011, MNRAS, 412, 1441
Liao, K., Treu, T., Marshall, P., et al. 2015, ApJ, 800, 11
Linder, E. V. 2004, Phys. Rev. D, 70, 043534
—. 2011, Phys. Rev. D, 84, 123529
Livne, E. 1990, ApJ, 354, L53
LSST Science Collaboration, Abell, P. A., Allison, J., et al. 2009, ArXiv e-prints, arXiv:0912.0201 [astro-ph.IM]
Maeda, K., Benetti, S., Stritzinger, M., et al. 2010, Nature, 466, 82
Mainzer, A., Bauer, J., Grav, T., et al. 2011, ApJ, 731, 53
Maoz, D., Mannucci, F., & Nelemans, G. 2014, ARA&A, 52, 107
McCully, C., Keeton, C. R., Wong, K. C., & Zabludoff, A. I. 2017, ApJ, 836, 141
McWilliam, A., Piro, A. L., Badenes, C., & Bravo, E. 2017, ArXiv e-prints, arXiv:1710.05030 [astro-ph.HE]
Moore, C. B., & Hewitt, J. N. 1996, Prospects for the Detection of Microlensing Time Delays, ed. C. S. Kochanek & J. N. Hewitt (Dordrecht: Springer Netherlands), 279
More, A., Suyu, S. H., Oguri, M., More, S., & Lee, C.-H. 2017, ApJ, 835, L25
Nomoto, K. 1982, ApJ, 257, 780
Nomoto, K., Thielemann, F.-K., & Yokoi, K. 1984, ApJ, 286, 644
Nordin, J., Rubin, D., Richard, J., et al. 2014, MNRAS, 440, 2742
Nugent, P., Kim, A., & Perlmutter, S. 2002, PASP, 114, 803
Nugent, P. E., Sullivan, M., Cenko, S. B., et al. 2011, Nature, 480, 344
Oguri, M. 2006, MNRAS, 367, 1241
—. 2010, PASJ, 62, 1017
Oguri, M., & Kawano, Y. 2003, MNRAS, 338, L25
Oguri, M., & Marshall, P. J. 2010, MNRAS, 405, 2579
Oguri, M., Inada, N., Strauss, M. A., et al. 2008, AJ, 135, 512

—. 2012, AJ, 143, 120
Patel, B., McCully, C., Jha, S. W., et al. 2014, ApJ, 786, 9
Pedregosa, F., Varoquaux, G., Gramfort, A., et al. 2012, ArXiv e-prints, arXiv:1201.0490 [cs.LG]
Pereira, R., Thomas, R. C., Aldering, G., et al. 2013a, A&A, 554, A27
—. 2013b, A&A, 554, A27
Perlmutter, S. 2014, in American Astronomical Society Meeting Abstracts, Vol. 223, American Astronomical Society Meeting Abstracts #223, 341.04
Perlmutter, S., Pennypacker, C. R., Goldhaber, G., et al. 1995, ApJ, 440, L41
Perlmutter, S., Aldering, G., Deustua, S., et al. 1997a, in Bulletin of the American Astronomical Society, Vol. 29, American Astronomical Society Meeting Abstracts, 1351
Perlmutter, S., Gabi, S., Goldhaber, G., et al. 1997b, ApJ, 483, 565
Perlmutter, S., Aldering, G., della Valle, M., et al. 1998, Nature, 391, 51
Perlmutter, S., Aldering, G., Goldhaber, G., et al. 1999, ApJ, 517, 565
Petrushevska, T., Amanullah, R., Goobar, A., et al. 2016, A&A, 594, A54
Phillips, M. M. 1993, ApJ, 413, L105
Phillips, M. M., Lira, P., Suntzeff, N. B., et al. 1999, AJ, 118, 1766
Pinto, P. A., & Eastman, R. G. 2000a, ApJ, 530, 744
—. 2000b, ApJ, 530, 757
Planck Collaboration, Ade, P. A. R., Aghanim, N., et al. 2016a, A&A, 594, A13
Planck Collaboration, Aghanim, N., Ashdown, M., et al. 2016b, A&A, 596, A107
Quimby, R. M., Oguri, M., More, A., et al. 2014, Science, 344, 396
Refsdal, S. 1964, MNRAS, 128, 307
Rest, A., Scolnic, D., Foley, R. J., et al. 2014, ApJ, 795, 44
Richards, J. W., Starr, D. L., Butler, N. R., et al. 2011, ApJ, 733, 10
Richards, J. W., Starr, D. L., Brink, H., et al. 2012, ApJ, 744, 192
Riess, A. G., Filippenko, A. V., Challis, P., et al. 1998, AJ, 116, 1009
Riess, A. G., Macri, L. M., Hoffmann, S. L., et al. 2016, ApJ, 826, 56
Rigault, M., Aldering, G., Kowalski, M., et al. 2015, ApJ, 802, 20
Rodney, S. A., Patel, B., Scolnic, D., et al. 2015, ApJ, 811, 70
Roth, N., & Kasen, D. 2015, ApJS, 217, 9
Rousseeuw, P. J., & Croux, C. 1993, Journal of the American Statistical Association, 88, 1273
Rusu, C. E., Fassnacht, C. D., Sluse, D., et al. 2017, MNRAS, 467, 4220
Rybicki, G. B., & Lightman, A. P. 1979, Radiative processes in astrophysics
Sako, M., Bassett, B., Becker, A., et al. 2008, AJ, 135, 348
Sako, M., Bassett, B., Connolly, B., et al. 2011, ApJ, 738, 162
Salpeter, E. E. 1955, ApJ, 121, 161
Scalzo, R., Aldering, G., Antilogus, P., et al. 2014a, MNRAS, 440, 1498
Scalzo, R. A., Ruiter, A. J., & Sim, S. A. 2014b, MNRAS, 445, 2535
Scalzo, R. A., Aldering, G., Antilogus, P., et al. 2010, ApJ, 713, 1073
Schmidt, B. P., Suntzeff, N. B., Phillips, M. M., et al. 1998, ApJ, 507, 46

Schneider, P., & Weiss, A. 1987, A&A, 171, 49
Seitenzahl, I. R., Ciaraldi-Schoolmann, F., Röpke, F. K., et al. 2013, MNRAS, 429, 1156
Shannon, C. E. 1948, BSTJ, 27, 379
Shappee, B. J., Kochanek, C. S., & Stanek, K. Z. 2013, ApJ, 765, 150
Shappee, B. J., Piro, A. L., Stanek, K. Z., et al. 2016, ArXiv e-prints, arXiv:1610.07601 [astro-ph.HE]
Shen, K. J., & Bildsten, L. 2009, ApJ, 699, 1365
Shen, K. J., Kasen, D., Miles, B. J., & Townsley, D. M. 2017a, ArXiv e-prints, arXiv:1706.01898 [astro-ph.HE]
Shen, K. J., Toonen, S., & Graur, O. 2017b, ArXiv e-prints, arXiv:1710.09384 [astro-ph.HE]
Sheth, R. K., Bernardi, M., Schechter, P. L., et al. 2003, ApJ, 594, 225
Silverman, J. M., Nugent, P. E., Gal-Yam, A., et al. 2013, ApJS, 207, 3
Sim, S. A., Röpke, F. K., Hillebrandt, W., et al. 2010, ApJ, 714, L52
Sim, S. A., Seitenzahl, I. R., Kromer, M., et al. 2013, MNRAS, 436, 333
Smith, A. M., Lynn, S., Sullivan, M., et al. 2011, MNRAS, 412, 1309
Smith, R. M., Dekany, R. G., Bebek, C., et al. 2014, in Proc. SPIE, Vol. 9147, Ground-based and Airborne Instrumentation for Astronomy V, 914779
Stritzinger, M., Leibundgut, B., Walch, S., & Contardo, G. 2006, A&A, 450, 241
Strolger, L.-G., Riess, A. G., Dahlen, T., et al. 2004, ApJ, 613, 200
Sullivan, M., Ellis, R., Nugent, P., Smail, I., & Madau, P. 2000, MNRAS, 319, 549
Suyu, S. H., Marshall, P. J., Auger, M. W., et al. 2010, ApJ, 711, 201
Suyu, S. H., Auger, M. W., Hilbert, S., et al. 2013, ApJ, 766, 70
Suyu, S. H., Bonvin, V., Courbin, F., et al. 2017, MNRAS, 468, 2590
Suzuki, N., Rubin, D., Lidman, C., et al. 2012, ApJ, 746, 85
Taam, R. E. 1980, ApJ, 237, 142
Taubenberger, S., Hachinger, S., Pignata, G., et al. 2008, MNRAS, 385, 75
Tewes, M., Courbin, F., Meylan, G., et al. 2013, A&A, 556, A22
Tie, S. S., & Kochanek, C. S. 2017, ArXiv e-prints, arXiv:1707.01908
Tojeiro, R., Masters, K. L., Richards, J., et al. 2013, MNRAS, 432, 359
Treu, T. 2010, ARA&A, 48, 87
Treu, T., & Marshall, P. J. 2016, ArXiv e-prints, arXiv:1605.05333
Tripp, R. 1998, A&A, 331, 815
van Dokkum, P. G. 2001, PASP, 113, 1420
Vapnik, V. 2013, The nature of statistical learning theory (Springer science & business media)
Vuissoz, C., Courbin, F., Sluse, D., et al. 2008, A&A, 488, 481
Wambsganss, J. 1990, PhD thesis, Thesis Ludwig-Maximilians-Univ., Munich (Germany, F. R.). Fakultät für Physik., (1990)
—. 1999, Journal of Computational and Applied Mathematics, 109, 353
Wang, B., & Han, Z. 2012, New A Rev., 56, 122
Wang, L., & Wheeler, J. C. 2008a, ARA&A, 46, 433
—. 2008b, ARA&A, 46, 433
Waszczak, A., Ofek, E. O., Aharonson, O., et al. 2013, MNRAS, 433, 3115

Whelan, J., & Iben, Jr., I. 1973, ApJ, 186, 1007
Willsky, A. S., Wornell, G. W., & Shapiro, J. H. 1995, Course notes for MIT, 6
Witt, H. J., & Mao, S. 1997, MNRAS, 291, 211
Wong, K. C., Suyu, S. H., Auger, M. W., et al. 2017, MNRAS, 465, 4895
Woosley, S. E., & Kasen, D. 2011, ApJ, 734, 38
Woosley, S. E., Kasen, D., Blinnikov, S., & Sorokina, E. 2007, ApJ, 662, 487
Woosley, S. E., & Weaver, T. A. 1994, ApJ, 423, 371
Wright, D. E., Smartt, S. J., Smith, K. W., et al. 2015, MNRAS, 449, 451
Wygoda, N., Elbaz, Y., & Katz, B. 2017, ArXiv e-prints, arXiv:1711.00969 [astro-ph.HE]
Yoon, S.-C., & Langer, N. 2005, A&A, 435, 967
York, D. G., Adelman, J., Anderson, Jr., J. E., et al. 2000, AJ, 120, 1579
Zhao, G.-B., Raveri, M., Pogosian, L., et al. 2017, Nature Astronomy, 1, 627
Zwicky, F. 1964, Annales d'Astrophysique, 27, 300